

DEVELOPMENT OF ELECTROSPUN NANOFIBER BIOSENSOR AND NUCLEAR
MAGNETIC RESONANCE BASED BIOSENSOR FOR RAPID PATHOGEN DETECTION

By

Yilun Luo

A DISSERTATION

Submitted to
Michigan State University
in partial fulfillment of the requirements
for the degree of

Biosystems Engineering — Doctor of Philosophy
Electrical Engineering — Dual Major

2020

ABSTRACT

DEVELOPMENT OF ELECTROSPUN NANOFIBER BIOSENSOR AND NUCLEAR MAGNETIC RESONANCE BASED BIOSENSOR FOR RAPID PATHOGEN DETECTION

By

Yilun Luo

Water and food contaminated with pathogens cause millions of hospitalizations and thousands of deaths, and costly recalls in food and retail industries annually. Among them, the Shiga Toxin-producing *Escherichia coli* (STEC) causes foodborne outbreaks every year, which leads to more than 265,000 illnesses, 3,600 hospitalizations, and 30 deaths in the United States alone. Currently approved detection methods, such as culturing and colony counting, or polymerase chain reaction (PCR), provide accurate diagnosis. However, these methods require long detection time (ranging from 6 to 24 hours), high testing cost, large-sized equipment, and/or skilled personnel, limiting their application in controlling outbreaks, reducing recall loss, or on-field diagnosis in developing countries. In this dissertation research, two biosensors were developed based on electrospun nanofiber and nuclear magnetic resonance (NMR) for rapid detection of STEC with high sensitivity. The electrospun biosensor was designed as lateral-flow immuno-sensor based on magnetic nanoparticles (MNPs) and electrospun nanofibers. The MNPs were coated with conductive nano-shells and functionalized with antibody to extract target pathogen by immunomagnetic separation. Biocompatible nanofibrous membrane was synthesized by electrospinning technique, which was optimized for nano-porous structure and excellent capillary properties. The electrospun membrane was functionalized with antibody to capture the MNP-pathogen conjugates by lateral-flow separation. As a result, the membrane's conductivity was proportional to pathogen concentration, which could be measured by a portable impedance analyzer. Owing to the novel nanostructure, the surface area and mass transfer rate were

significantly increased. This improved the biochemical binding effect and sensor signal to noise ratio. The biosensor's sensitivity limit was 61 colony forming units per milliliter (CFU/mL) and 10^4 cell culture infective dose per milliliter (CCID/mL) for bacterial and viral samples, respectively, with detection time of 8 min. The electrospun biosensor has advantages of low cost and high sensitivity, which can be used for on-field biodefense and food safety applications.

In the second work, a portable nuclear magnetic resonance (pNMR) biosensor was developed based on antibody functionalized MNPs as proximity biomarkers of the pathogen, which induced micro-magnetic variation to accelerate NMR resonance signal decay. The pNMR was designed using a hand-held magnet of 0.47 Tesla, a high-power radio frequency (RF) transmitter, and an ultra-low noise receiver capable of detecting 0.1 μ V NMR signal. The pNMR biosensor assay and sensing mechanism was used in detecting *E. coli* O157:H7, and sensitivity limit was 76 CFU/mL in water samples and 92 CFU/mL in milk samples with detection time of 1 min. The pNMR biosensor is innovative for bacterial detection in food matrices and can be extended to other microbial or viral organisms by changing the antibody specificity. Besides, the pNMR biosensor can be used for on-field healthcare diagnostic and biodefense applications owing to its advantages of portability and speed of detection.

Copyright by
YILUN LUO
2020

This work is dedicated to my father Xinhua Luo, my mother Zhongchun Xu, my wife Lei Jin,
and my daughter Jessica Jinyi Luo.

ACKNOWLEDGEMENTS

I sincerely thank everyone who supported and contributed to the completion of this research throughout the years. First and foremost, I would like to express my deepest gratitude to my advisor, Dr. Evangelyn Alocilja, for her continuous support and guidance over the years and for making everything possible. Her expertise, broad vision, and encouragement helped me finish my Ph.D. research. I would like to thank her for valuable advice, encouragement, and mentoring throughout my graduate study and research. I would also like to thank my co-advisor in the Department of Electrical and Computer Engineering, Dr. Timothy Hogan for his strong support and insightful guidance during my dual-major doctoral research. I would like to thank the members of my Ph.D. guidance committee professors, Dr. Premjeet Chahal, Dr. Wei Liao, and Dr. Renfu Lu for their valuable advice, helpful discussions, and all the support.

I thank all the members in the Biosensors research group, Michael Anderson, Barbara Cloutier, Yang Liu, Shannon McGraw, Sudeshna Pal, Emma Settington, Edith Torres, Yun Wang, and Deng Zhang for sharing a creative, professional, and pleasant research environment. I also would like to express my appreciation to Dr. Lawrence Drzal and Steven Nartker in the Department of Chemical Engineering for the innovative research collaboration and valuable discussions. I especially would like to thank Dr. Nejadhashemi Amirpouyan, the Graduate Coordinator in the department, for his help and support to my doctoral readmission and study at Michigan State University. Besides, I would like to thank Hanna Miller, Michael Wiederoder, David Hochhalter, and all the other undergraduate assistants who have worked with me over the past years. I also

thank the Ann Arbor Technical Center and the Southwest Research Institute for all the support and assistance provided to complete this doctoral research work.

Finally, I would like to express my deepest gratitude and love to my parents, Xinhua Luo and Zhongchun Xu, and my family for their unconditional support, love, and believing in me during my Ph.D. pursuit. I truly appreciate my wife, Lei Jin, who accompanied me through the past years and provided countless encouragement and support no matter what difficulties or challenges she encountered and fought for. Ultimately, to our daughter, Jessica Jinyi Luo, who was born in the year before my dissertation defense. She brought us such precious and memorable joy while transforming our lives and providing me with the best motivation for completing this dissertation.

Yilun Luo

TABLE OF CONTENTS

LIST OF TABLES	x
LIST OF FIGURES	xi
KEY TO ABBREVIATIONS.....	xv
CHAPTER 1 INTRODUCTION	1
1.1 Hypothesis.....	3
1.1.1 Contribution I: Electrospun Nanofiber Biosensor	3
1.1.2 Contribution II: Portable NMR Biosensor.....	3
1.2 Research Objectives	4
1.3 Research Significance and Novelty.....	4
CHAPTER 2 LITERATURE REVIEW	7
2.1 <i>Escherichia coli</i> Pathogen.....	7
2.1.1 Traditional Methods of Detection.....	10
2.2 Biosensor based Detection	13
2.2.1 Acoustic Biosensor	14
2.2.2 Electrochemical Biosensor.....	16
2.2.3 Optical Biosensor.....	17
2.2.4 Immunoassay Biosensor	19
2.2.5 NMR based Microorganism Detection	21
CHAPTER 3 SYNTHESIS AND CHARACTERIZATION OF MAGNETIC NANOPARTICLES	26
3.1 Introduction	26
3.2 Materials and Methods	27
3.2.1 Synthesis of Conductive Immunomagnetic Nanoparticle.....	27
3.2.2 Synthesis of NMR Magnetic Nanoparticle	28
3.2.3 Magnetic Nanoparticle Characterization	29
3.3 Results and Discussion	30
3.3.1 Magnetic Nanoparticle Characterization and Synthesis	30
3.4 Conclusions	31
CHAPTER 4 BIOSENSOR BASED ON ELECTROSPUN NANOFIBERS AND MAGNETIC NANOPARTICLES FOR PATHOGEN DETECTION	32
4.1 Introduction	32
4.2 Materials and Methods	34
4.2.1 Electrospun Material Synthesis.....	34
4.2.2 Plasma Enhancement for Capillary Flow	38
4.2.3 Sensor Architecture and Detection Principle.....	39
4.2.4 Test Pathogens and Antibodies	44
4.2.5 Surface Functionalization	45

4.2.6 Immunomagnetic Separation	47
4.2.7 Detection and Data Analysis.....	49
4.3 Results and Discussion	51
4.3.1 Surface Functionalization with Antibody	51
4.3.2 Aligned Nanofibrous Membrane by Parallel Electrode Electrospinning	54
4.3.3 Biosensor Detection	55
4.4 Conclusions	66
CHAPTER 5 BIOSENSOR BASED ON NMR AND MAGNETIC NANOPARTICLES FOR PATHOGEN DETECTION	69
5.1 Introduction	69
5.2 Materials and Methods	70
5.2.1 Design of Portable NMR Biosensor	70
5.2.2 Design of Portable NMR Duplexer.....	73
5.2.3 Design of Portable NMR Antenna.....	77
5.2.4 Design of Matching Networks of the pNMR Probe	83
5.2.5 Evaluation of the Portable NMR Probe and the Matching Networks.....	88
5.2.6 NMR Power Amplifier	92
5.2.7 NMR Low Noise Amplifier	96
5.2.8 NMR Detection using Magnetic Nanoparticle	99
5.2.9 Effects of MNP on NMR Relaxation.....	103
5.2.10 Detection of pNMR Relaxation Time.....	115
5.2.11 Test Pathogen and Antibodies	118
5.2.12 Magnetic Pathogen Separation	118
5.2.13 Sensor Architecture and Detection Principle.....	119
5.2.14 Detection and Data Analysis.....	120
5.3 Results and Discussion	121
5.3.1 Functionalization of Magnetic Nanoparticles with Antibody.....	121
5.3.2 MNP Antibody Functionalization.....	122
5.3.3 NMR R_2 Relaxation Time	123
5.4 Conclusions	129
CHAPTER 6 CONCLUSION AND FUTURE WORK	131
6.1 Conclusions	131
6.2 Recommendations for Future Work	133
APPENDIX.....	135
BIBLIOGRAPHY.....	155

LIST OF TABLES

Table 2.1 Reported <i>E. coli</i> O157:H7 Outbreaks and Infections in the United States of the last five years (2016 to 2020) [16].	8
Table 4.1 Dimension of the biosensor and its components	42
Table 4.2 P-value of biosensor test results (unaligned nanofiber) for <i>E. coli</i> O157:H7	61
Table 4.3 P-value of biosensor test results (unaligned nanofiber) for BVDV	62
Table 4.4 P-value of biosensor test results (aligned nanofiber) for <i>E. coli</i> O157:H7	63
Table 4.5 P-value of biosensor test results (nitrocellulose mat) for <i>E. coli</i> O157:H7	65
Table 5.1 Matching network design based on NMR probe characterization through resistance and inductance measurement	86
Table 5.2 RF performance of Henry Radio 50B HF power amplifier, including output power, frequency range, and operating mode.	94
Table 5.3 RF performance of Miteq AU-1467 low noise amplifier, including frequency range, gain, and noise figure.	97
Table 5.4 RF performance of Sonoma Instrument 310 low noise amplifier, including frequency range, gain, and noise figure.	99
Table 5.5 P-value of NMR biosensor test results for <i>E. coli</i> O157:H7 in water samples.	127
Table 5.6 P-value of NMR biosensor test results for <i>E. coli</i> O157:H7 in milk samples	128

LIST OF FIGURES

Figure 2.1 Schematic diagram and working principle of a biosensor system.	13
Figure 2.2 The oscillating frequency is inversely proportional to the mass as indicated by the spring-mass oscillator system as an example.....	14
Figure 2.3 Scheme of sensor operating principle for electrochemical biosensors (adapted and modified from [31]).....	17
Figure 2.4 Scheme of sensor structure and operating principle for optical biosensors (adapted and modified from [35]).....	18
Figure 3.1 Synthesis of conductive immunomagnetic nanoparticles by encapsulating gamma-iron oxide ($\gamma\text{-Fe}_2\text{O}_3$) nanoparticles with polymerizing aniline as conductive nano-shell. ..	28
Figure 4.1 Schematic diagram of electrospinning setup for nanofibrous membrane fabrication, consisting of the syringe, the needle, the nanofiber jet (the Taylor cone, the stable region, and the instability region), and the rotating collector.	35
Figure 4.2 Self-contained Nanofiber Electrospinning Unit (NEU, Kato Tech Co. Japan) using rotating drum as collector for high yield fiber fabrication.....	36
Figure 4.3 Scanning electron microscopy image of electrospun nitrocellulose nanofibers.	37
Figure 4.4 Nanofibers spun across the gap of a parallel electrode collector on the NEU unit.....	38
Figure 4.5. The capillary flow capability comparison of electrospun nanofibrous membranes (A) without and (B) with the plasma enhancement.....	39
Figure 4.6 Silver electrodes fabricated on electrospun nanofiber membrane using spray deposition method.	40
Figure 4.7. Schematic of the biosensor structure and membrane assembly consisting of cellulose application and adsorption pads and electrospun cellulose nitrate capture pad.....	41
Figure 4.8. Detection scheme of the lateral flow immunosensor based on immunomagnetic nanoparticle and electrospun antibody functionalized capture membrane.	43
Figure 4.9. The surface antibody functionalization process for the electrospun biosensor capture pad.....	47
Figure 4.10. The antibody functionalization process for the conductive MNPs.	49

Figure 4.11 Testing platform of electrospun MNP biosensor. (a) Test strip mounted on platform and sandwiched by copper electrodes. (b) Design of the entire platform with three testing units	50
Figure 4.12 The CLSM image of functionalized membrane with FITC antibody, (A) CLSM image of nitrocellulose nanofibrous membrane with FITC antibody functionalization, (B) CLSM image of nitrocellulose nanofibrous membrane without antibody. Significant fluorescence emission at 530 nm verifies the antibody immobilization. ..	52
Figure 4.13 FITC antibody functionalized electrospun membrane: (A) CLSM image verified that the fiber morphology retains after antibody functionalization. (B) Fluorescence image confirmed that antibodies are attached on membrane after wash step by significant fluorescent emission at 435 nm.....	53
Figure 4.14 The SEM and optical microscope image of functionalized membrane with FITC antibody (A) SEM image of the electrospun nanofibrous membrane, (B) optical microscope image of nanofibrous membrane and silver electrodes after antibody functionalization.....	53
Figure 4.15 SEM image of highly-aligned nanofibrous membrane synthesized by the parallel electrode collector electrospinning.	54
Figure 4.16 The CLSM image at 600×: significant fluorescent emission verified strong antibody functionalization, and the highly-aligned fiber morphology still remained intact.....	55
Figure 4.17 SEM images of electrospun membrane after test. <i>E. coli</i> O157:H7 were effectively captured on the functionalized fiber mat.....	56
Figure 4.18 SEM images of electrospun membrane after test. No bacteria were observed in the nanofiber mat without functionalization.	57
Figure 4.19 Biosensor conductance signal versus test time of <i>E. coli</i> O157:H7 samples with different target concentrations: aligned nanofibrous biosensor	59
Figure 4.20 Biosensor (unaligned nanofibers) conductance signal versus test time of <i>E. coli</i> O157:H7 samples with different target concentrations: randomly oriented nanofibrous biosensor	60
Figure 4.21 Biosensor test results (unaligned nanofiber) for <i>E. coli</i> O157:H7 demonstrate a linear sensing response from 0 to 10 ⁴ CFU/mL.....	60
Figure 4.22 Biosensor test results (unaligned nanofibrous mat) for BVDV virus demonstrate the linear sensor response from 10 ¹ to 10 ³ virus dilution and control sample.	61
Figure 4.23 Biosensor test results (aligned nanofibers) for <i>E. coli</i> O157:H7 demonstrated a linear relationship between resistance signal and bacterial concentration from 10 ¹ to 10 ⁴ CFU/mL. The signal was significantly below the control from 10 ⁵ to 10 ⁷ CFU/mL. .	63

Figure 4.24 Pathogen detection comparison of biosensors made of electrospun nanofibrous membrane and nitrocellulose mesoporous membrane.	65
Figure 5.1 System Architecture of the Portable NMR, including FPGA control, modulation and demodulation system, and NMR sub-systems.	72
Figure 5.2 System prototype of the portable NMR, including a palm-sized permanent magnet, NMR transmitter, NMR receiver, T/R switch, sample holder, and NMR probe.	73
Figure 5.3 Complete set up of NMR coil antenna and duplexer switch for the NMR transmitter and receiver	74
Figure 5.4 The crossed diodes pair shows high impedance for low voltages, and low impedance for high voltages. The threshold is the built-in voltage.	75
Figure 5.5 NMR coil antenna and duplexer switch based on quarter-wave impedance transformer: transmitter ON	76
Figure 5.6 NMR coil antenna and duplexer switch based on quarter wavelength transformer: transmitter OFF	77
Figure 5.7 A high Q NMR antenna corresponds to higher selectivity, and is more immune to noise for the NMR receiver [153]	82
Figure 5.8 The NMR probe, consisting of NMR coil antenna and a matching network, was designed to achieve high quality factor to optimize NMR signal acquisition.	85
Figure 5.9 NMR probe comprising of NMR coil antenna, NMR sample tube, tuning circuit, and non-magnetic probe holder is designed and fabricated in the Nano-Biosensors Lab. .	88
Figure 5.10 The NMR probe evaluation using a Keysight E5062 VNA for reflection coefficient and quality factor. Its matching network was tuned while measuring using the VNA to optimize the reflection coefficient (S_{11}) and achieved -23.6 dB.	89
Figure 5.11 The NMR probe was designed to achieve high quality factor to optimize NMR signal acquisition. Its matching networks was tuned to optimize the reflection coefficient using a VNA and achieved -23.6 dB at 19.918 MHz.....	90
Figure 5.12 Testing set up of the NMR transmitter using the function generator, 50 Ω loads and oscilloscope to calibrate the input power required for pNMR application.	95
Figure 5.13 The input power to the NMR transmitter was calibrated to achieve 20 W output to the NMR probe.....	96
Figure 5.14 Testing set up of the NMR receiver using the function generator, attenuators, and the oscilloscope to evaluate the LNA with the $\lambda/4$ wavelength duplexers.	98

Figure 5.15 The Conventional nuclear magnetic resonance (NMR) spectrometer, Bruker 700 MHz NMR system [165].....	100
Figure 5.16 The Zeeman effect: nuclei spin energies split when placed in an external magnetic field [168].....	104
Figure 5.17 Dipolar interaction between nuclear spins, I and S, through space. The spin S induces a local field <i>B_{loc}</i> at the spin I.	106
Figure 5.18 NMR spin-echo technique to treat the inhomogeneous field of a small permanent magnet using 90 degree and 180 degree RF pulse trains. (adapted and modified from [176]).....	116
Figure 5.19 NMR spin-echo technique and CPMG pulse sequence to detect the spin-spin relaxation time, <i>T₂</i> in a less homogeneous magnetic field.	117
Figure 5.20 Working principle of the NMR based biosensor for pathogen detection.....	119
Figure 5.21 Magnetic nanoparticles as biomarker to detect the target pathogen by the NMR measurement.	120
Figure 5.22 TEM image and electron diffraction image (inset) of the MNPs.....	122
Figure 5.23 NMR biosensor relaxation signal of detection: (A) control (blank) sample, and (B) bacterial sample.....	124
Figure 5.24 The MNP-based pNMR biosensor's measurement of relaxation time change, delta <i>T₂</i> , for drinking water, which were contaminated by <i>E. coli</i> O157:H7.....	127
Figure 5.25 The MNP-based pNMR biosensor's measurement of relaxation time change, delta <i>T₂</i> , for whole milk samples, which were contaminated by <i>E. coli</i> O157:H7	128

KEY TO ABBREVIATIONS

AC	Alternative Current
BVDV	Bovine Viral Diarrhea Virus
CEA	Carcinoembryonic Antigen
CDC	Centers of Disease Control and Prevention
CFU	Colony-Forming Unit
CLSM	Confocal Laser Scanning Microscopy
CMOS	Complementary Metal Oxide Semiconductor
CNT	Carbon Nano Tube
CPMG	Carr-Purcell-Meiboom-Gill
C4	Complement Component 4
DFB	1,4-difluorobenzene
DI	De-Ionized
DMF	Dimethylformamide
ECL	Electrochemiluminescent
EGF	Epidermal Growth Factor
ELISA	Enzyme-linked Immunosorbent Assay
ENM	Electrospun Nanofibrous Membrane
FDA	Food and Drug Administration
FITC	Fluorescein Isothiocyanate
FPGA	Field Programmable Gate Array
FSM	Finite State Machine

HUS	Hemolytic-uremic Syndrome
IC	Integrated Circuit
IgG	Immunoglobulin G
ITO	Indium Tin Oxide
LCP	Lanthanide-complexed Polymer
LFA	Lateral Flow Assay
LIBS	Laser-Induced Breakdown Spectroscopy
LOC	Lab-On-Chip
MNP	Magnetic Nanoparticle
MPN	Most Probable Number
MWCNT	Multi Walled Carbon Nano Tube
NEO	Neomycin
NIAID	National Institute of Allergy and Infectious Disease
NV	Nitrogen Vacancy
NMR	Nuclear Magnetic Resonance
PANI	Polyaniline
PBS	Phosphate-buffered Saline
PCR	Polymerase Chain Reaction
pNMR	Portable Nuclear Magnetic Resonance
PVDC	Polyvinylidene Chloride
QCM	Quartz Crystal Microbalance
QNS	Quinolones Antibiotics
RF	Radio Frequency

SEM	Scanning Electron Microscope
SERS	Surface-enhanced Raman Scattering
SNR	Signal to Noise Ratio
SPR	Surface Plasmon Resonance
STEC	Shiga Toxin-producing Escherichia Coli
SWCNT	Single Walled Carbon Nano Tube
TEM	Transmission Electron Microscopy
THF	Tetrahydrofuran
TMP	Trimethyl Phosphate
VHDL	Very High Speed Integrated Circuit Hardware Description Language
WHO	World Health Organization

CHAPTER 1

INTRODUCTION

Clean drinking water is essential to public health and safety. Pathogenic contaminations cause enormous medical expenses, massive losses to retailers and food industry, and serious threats to biosecurity. *Escherichia coli* O157: H7, an important waterborne pathogen, is associated with acute and lethal illness, including diarrhea, hemorrhagic colitis, and hemolytic-uremic syndrome (HUS), which has attracted extensive attention from academia and health agencies. *E. coli* O157: H7 infects human alimentary tract, produces Shiga toxin, and induces abdominal cramps with hemorrhagic diarrhea [1]. Studies from 10 of the 14 subregions of the World Health Organization (WHO) indicates that the global breakout of *E. coli* is 2.8 million cases annually. In the United State alone, estimates of *E. coli* O157:H7 induced hemorrhagic colitis cases are 63,000 per year [2][3]. *E. coli* grow rapidly at exponential rate. Hence, rapid and accurate testing of water samples are crucial to identify the pathogenic bacteria and control the spread of disease. The current standard detection methods are growth based, which require 18 hours or longer for the identification [4][5]. Culture plating-based methods detect the bacteria through metabolic pathways, not by pathogenic capabilities. These methods are slow and have limitation in selectivity among related species [6]. Testing methods based on DNA gene sequences are applied to the detection and identification of bacteria, including polymerase chain reaction (PCR), isothermal amplification, and bio-barcode method. PCR directly detects the gene sequences and is highly sensitive in identification. However, it requires specialized equipment, strict reagent storage, and highly skilled personnel, and hence often limited to laboratory application [7]. Isothermal amplification is less expensive than PCR owing to simplified equipment requirements but is still

limited due to the requirement for enzyme storage at low temperature [8]. The bio-barcode method is based on DNA amplification and is applicable for enzyme free detection. However, it involves DNA input and the detection process is time consuming [9]. Antibody detection is based on its recognition of antigenic proteins on the cell surface of the target bacteria. It is used in bio-barcode detection and enzyme-linked immunosorbent assay (ELISA) [10]. ELISA has higher sensitivity, but it is expensive and not suitable for high throughput measurement. Its detection time often takes 24 hours or longer.

This dissertation describes the research work on two biosensors developed for the detection of *E. coli* O157: H7. The first part of the dissertation is the development of lateral flow immunobiosensor based on electrospun nanofibers and magnetic nanoparticles (MNPs). The second part of the dissertation describes the development of an MNP-based portable nuclear magnetic resonance (NMR) biosensor.

The dissertation is organized as follows. Chapter 2 presents a review of the literature on technologies relevant to this research work, including the current standard testing, biosensor-based detection and NMR based detection. Chapter 3 describes the generation of MNPs synthesized by amine-functionalized iron oxide using thermal decomposition method, and their optimization for the electrospun biosensor and the pNMR biosensor applications. Chapter 4 describes the development of electrospun nanofibrous membrane, surface modification, antibody functionalization, and the design for MNP-based lateral flow immuno-assay biosensor. Chapter 5 summarizes our efforts to develop NMR sensing of MNP-labeled pathogen by combination of an improved cell binding process, portable NMR development and performance optimization, and

NMR detection based on selective immuno-assay MNP. Chapter 6 contains the summary of the research and recommendations for future work.

The following section describes the research hypothesis, objectives, and novelty of the dissertation work performed.

1.1 Hypothesis

The two research contributions presented in this dissertation are based on the following hypotheses:

1.1.1 Contribution I: Electrospun Nanofiber Biosensor

- An antibody-based biosensor platform can be developed for rapid detection of pathogenic contaminants through impedance readout of an MNP-pathogen sandwich assay captured by lateral flow separation using the electrospun membrane.

1.1.2 Contribution II: Portable NMR Biosensor

- A portable NMR biosensor platform can be developed to measure the concentration of target pathogen in water and food samples based on the acceleration of proton spin relaxation induced by antibody conjugated MNPs.

1.2 Research Objectives

The overall objective of this dissertation research is to develop rapid pathogen detection biosensors to detect *E. coli* O157:H7. The detailed objectives of this project are as follows.

- To synthesize MNPs, functionalize them with antibody, and optimize them for impedance detection and NMR detection, respectively
- To synthesize electrospun nanofibrous membranes and optimize them for lateral flow immunoassay to capture target pathogens and separate supernatant
- To develop a lateral flow immunoassay biosensor based on MNP and electrospun nanofibrous membrane for rapid detection through electrical impedance measurement
- To develop a portable NMR biosensor for rapid testing of water and milk samples by measuring perturbations of proton spin relaxation caused by MNPs immuno-conjugated on the target pathogen

1.3 Research Significance and Novelty

The novelty of the research contribution presented in this dissertation lies in exploring the use of an innovative nanomaterial, nitrocellulose electrospun nanofibrous membrane (ENM), in functions of lateral flow separation, pathogen capture, and biosensing transducer. High throughput fabrication method, capillary enhancement, immuno functionalization, and impedance sensing are innovative. The adaptability of nano biosensor has been demonstrated in detecting both bacterial and viral pathogens. Current literature shows a sizable amount of research on nitrocellulose ENM synthesis. However, the capillary action enhancement and lateral flow assay (LFA) application have not been reported in prior literature. New literature shows ENMs based on metal oxide or

DNA network have been implemented as impedimetric biosensors to detect chemical compounds, ions, and cancer cells [11]-[14]. However, as of today, this is the first report of an ENM in an integrated design of LFA and impedimetric immunoassay as one biosensor system, and successful detection of both bacterial and viral pathogens.

The electrospun lateral flow biosensor demonstrated excellent performance in sensing response and detection speed. Owing to high surface-to-volume ratio and unique nanostructure, the ENM enhanced capillary action, assay kinetics, and immunochromatography ability compared to conventional membrane material. This led to improved target pathogen binding effects, filtration, and separation from sample supernatant. The electrospun biosensor is of low cost and small size, and capable of rapid detection with high sensitivity, which can be used for on-field application of food safety, water monitoring, and biodefense.

The innovation of the research contribution in the second biosensor includes exploring the use of polyaniline maghemite MNP, filtration assay to quantify the pathogen by MNP concentration, as well as inexpensive and high signal-to-noise ratio (SNR) NMR probe and RF transceiver for microbial detection in complex matrices. The biosensor is novel in aspects of design and application. The versatility of the pNMR biosensor was demonstrated in bacterial detection in both water and dairy food samples. Current literature shows a number of portable NMR systems for noninvasive imaging. Recent literature shows several biosensing applications of micro NMRs that are fabricated based on integrated circuit (IC) and micro-fabrication technologies. Their detection of biotargets, such as cancer cells and molecules, are based on immuno-clustering of MNPs. The reported sensitivity is in the range of 10^3 CFU/mL (*Staphylococcus aureus*). The fabrication

approach is also more costly. To the best of our knowledge, this is the first report of NMR biosensor with successful detection of bacterial pathogen in water and dairy food samples. The sensitivity demonstrated a lower limit and wider linear response, from 10^1 to 10^4 CFU/mL.

To minimize infectious disease spread and reduce costly food recalls and medical expenses, it is crucial to implement rapid pathogen detection systems with high sensitivity and on-field capability. The micro NMR systems in the existing literature are small in size and suitable for on-field application. Based on the water and food monitoring application, there is still a need to improve their sensitivity limits and sample volume (currently up to sub-10 μL). We developed a portable NMR biosensor based on high SNR probe and NMR transceiver, resulting in a higher sensitivity and wider linear sensing response, as shown in Figure 5.24 and Figure 5.25. It was also capable of testing samples with a volume up to 180 μL , allowing combined detection of multiple samples in one test, which is essential to rapidly handle massive test samples during a pandemic. With the novel filtration assay, the test sample could be easily concentrated to handle larger test volume or to detect lower concentration. The pNMR detection is nondestructive, which allows further investigation through other testing methods. The system is low in cost and highly portable, which is favorable for on-field and rapid detection of foodborne pathogens.

CHAPTER 2

LITERATURE REVIEW

2.1 *Escherichia coli* Pathogen

With incidences occurring every year, microbial contaminations in water and food safety have become main concerns. One of the leading bacterial pathogens is *Escherichia coli* O157:H7, which belongs to the Shigatoxigenic group of *E. coli* (STEC). It is a gram-negative rod-shaped bacterium of micro size around 1.1 to 1.5 μm in diameter, 2.0 to 6.0 μm in length, and with a cell volume of 0.6 to 0.7 μm^3 . The infection can be caused by ingestion of contaminated food or water, or oral contact with contaminated surfaces. The resultant illness can last for 5 to 10 days with symptoms including severe and acute hemorrhagic diarrhea, abdominal cramps, headache, vomiting, and nausea. Infection with some patients, particularly children five years and younger, immunity-compromised person and the elderly, can lead to life-threatening hemolytic uremic syndrome (HUS), which cause red blood cells to breakdown, or be destroyed, and kidney failure [15]. The occurrence rate is around 2% to 7% of infections. In the United States, the main cause of acute kidney failure in children is the HUS, most of which are caused by *E. coli* O157:H7 infection.

Meanwhile, *E. coli* O157:H7 is one of the major bacterial pathogens accountable for foodborne illness and product recall, such as drinking water, beverages, fresh vegetables, and fast food, etc. There were at least eight confirmed food-linked outbreaks of the bacteria in the U.S. in the last five years (2016 to 2020) as reported by the United States Centers of Disease Control and Prevention (CDC) (Table 2.1) [16]. In 2018, food contamination of *E. coli* O157:H7 in romaine lettuce caused two foodborne infection outbreaks. The first one lasted from March to June and

caused a total of 210 cases across 36 states with 96 hospitalization and 5 death. The second one lasted from October 2018 to January 2019, and caused a total of 62 cases across 16 states with 25 hospitalization and a recall of all 18 kinds of sandwiches and other food products distributed in 5 states, leading to a health alert issued by the CDC [17]. In the latest outbreak as recently as January 2020, *E. coli* O157:H7 contaminated fresh salad kits caused infections in multiple states and costly hospitalization. Furthermore, the bacteria can contaminate various other kinds of food products, such as spinach, sprouts, flour, cookie dough, butter, cheese, hazelnut, sausage, beef and pork, etc., which have been reported by the CDC.

Table 2.1 Reported *E. coli* O157:H7 Outbreaks and Infections in the United States of the last five years (2016 to 2020) [16].

Outbreak Time	Source of the Outbreak	Reported Cases	States	Hospitalizations	Recall
2019/11/05 to 2020/01/15	Fresh Express Sunflower Crisp Chopped Salad Kits	10	5	4	No
2019/9/20 to 2019/12/21	Romaine Lettuce	167	27	85	Yes
2018/10/07 to 2019/01/09	Romaine Lettuce	62	16	25	Yes
2018/03/13 to 2018/06/28	Romaine Lettuce	210 (5 death)	36	96	No
2017/11/05 to 2018/01/25	Leafy Greens	25 (1 death)	15	9	No
2017/01/04 to 2017/05/04	I.M. Healthy Brand Soy Nut Butter	32	12	12	Yes
2016/06/27 to 2016/10/19	Beef, Veal, and Bison products	11	5	7	Yes
2016/01/17 to 2016/03/25	Alfalfa Sprouts	11	2	2	Yes

As estimated by the CDC, the totally annual cost of *E. coli* O157:H7 infections is around \$271,418,690 [18]. The yearly total cases of illness are estimated at 63,153. 11,737 cases required the assistance of physicians, of which 1,806 patients were hospitalized. Among those, 10 cases were deadly even though HUS was not developed, while 302 cases did developed HUS with 12 acute deaths and 10 premature deaths at a later point. The infections result in various costly expenses to patients, employers, and the health care system for medical expense, acute and premature death loss, wage loss, and productivity loss.

Furthermore, the *E. coli* O157 is highly effective in multiplication and infection. It can spread in water, food, soil, or on surfaces that has been contaminated by body fluids or feces of animal or human. The bacteria can live in the intestines of healthy cattle and other animals without illness. Study by the United States Food and Drug Administration (FDA) indicates that fewer than 10 to 100 colony forming units (CFU) is sufficient to cause infection [19]. It is required by the World Health Organization (WHO) that *E. coli* bacteria must not be detectable in any 100-ml water sample to verify the quality and safety of water intended for drinking or public distribution [20]. Furthermore, *E. coli* O157:H7 is classified as a “Category B”, the second highest priority, pathogen for biodefense by the CDC and the National Institute of Allergy and Infectious Disease (NIAID), due to its ease of wide spread in water, beverages, and various food sources, and highly virulent illness consequences [21][22].

As a result, it is not tolerant for any level of *E. coli* O157:H7 in water or food intended for human use. And it is essential to identify micro quantities of this pathogen in unknown samples effectively and rapidly. The standard method of *E. coli* O157:H7 detection requires highly trained personnel

and complex instrument with long testing time. The identification involves several steps including enrichment in selective media, incubation on differential agar to isolate sorbitol non-fermenting colonies, biochemical identification, and definitive identification, lasting around four days. Detection by PCR is capable of phenotypical and serological identification with high accuracy. However, it requires long testing time lasting several days, and high cost due to complex sample preparation steps, such as DNA extraction and amplification. For faster testing, the real-time PCR method can be used to detect the bacteria, after the selective enrichment process, to provide a testing result of positive or negative within 24 h and are not applicable for on-field applications [23]. However, it still requires the culture method and PCR to confirm presumptive positive results for three days [19]. Hence, it is still of high demand to improve detection time and sensitivity for *E. coli* O157:H7 for disease surveillance, prevention strategies, and water and food monitoring.

The following sections described the traditional methods as well as novel methods based on biosensors for pathogen detection used in water and food monitoring efforts.

2.1.1 Traditional Methods of Detection

The conventional methods of bacterial identification are through gas generation or colorimetric change, of which the determination is based on the metabolic differences. Among this category, there are three techniques approved by the EPA, including presence or absence testing, multiple fermentation tube, and membrane filtration.

The presence/absence testing technique is the first option for bacterial testing [24]. The procedure involves adding a known volume of water sample, typically 100 mL, to a liquid or powder media

in a sterile container, and determination by change of color after incubation of 24 hours. This technique has simple procedures of testing and analysis and does not require incubator owing to its wide temperate range. However, its results are not quantitative, and is not appropriate for testing known contaminated samples.

The multiple fermentation tube technique is performed by growing the test sample in a liquid medium with a second tube inversely placed inside to show gas generation [25]. The culture medium suitable for coliforms can be lactose, lauryl tryptose, or lactose bile broth. The test sample are incubated inside the tube under anaerobic conditions at 35-45°C for 24-48 hours to allow gas generation. The presence of the coliforms is indicated by pH or turbidity or change of the culture medium, or by the gas presence. The result is reported as a most probable number (MPN) index, which is determined by comparing the pattern of tube numbers showing growth at each dilution (the positive results) with statistical tables. Hence, it is a statistical estimate of the starting concentration with unit of MPN index per 100 mL, but not an actual count of bacteria presented in the sample. A second fermentation for 24 hours is required for positive quantification of fecal coliform to determine total and fecal coliform quantities. This method remains being the key conventional procedure for sample matrices that are non-transparent or colored such as milk or turbid field samples with semi-solids.

The membrane filtration technique integrates the filtration concentration and growth assay. It starts with filtering a measured volume of liquid sample under vacuum through a cellulose acetate membrane of uniform pore diameter, typically 0.45 µm. The bacteria captured on the membrane is incubated in a sterile container using a selective medium, such as m-Endo-type agar to form red

bacterial colonies after growth at 35 °C of 24 hours. Other medium that can be used for this technique includes Lactose agar with Tergitol 7, Teepol broth, ChromAgar, MacKonkey agar, MacKonkey-sorbital agar, and Rainbow agar. This technique is regularly used in monitoring water systems owing to its capability of testing relatively large numbers of samples by filter concentration. It also requires less testing time than the multiple fermentation tube technique and can give a direct count of total and fecal coliforms present in the sample. However, the result can still be affected due to uncountable plate growth, over-crowding, and capture of non-target microbes that can out-compete the coliforms. Culture media and buffered dilution water may be prepared in the field, but this requires the transport of all necessary equipment, which may include measuring cylinders, beakers, distilled water, autoclavable bottles, a large pressure-cooker and a gas burner or other source of heat. It is possible to prepare the culture media on field, but needs transport all necessary equipment, including distilled water, autoclavable bottles, beakers, measuring cylinders, a large pressure-cooker and a heat source, such as gas burner.

The EPA approved methods have been used for many years in water sample testing and monitoring. However, a major drawback is their long testing time with common methods taking 24 to 48 hours, and rapid methods taking 12 hours. There is still a considerable gap with the actual requirement indicated in the previous section to meet the demand of reducing disease infection and costly recall. Besides, the growth system can be affected by contamination with other microbials, which is usually common in on-field samples. Non-target microbials can over-compete and slow the growth of the target, leading to false negative results. Moreover, selective culture medium cannot guarantee the optimal growth conditions thus giving false negative results when the target pathogen is stressed or of low concentration.

2.2 Biosensor based Detection

Biosensors are sensing devices that combine a bioreceptor element and a physicochemical transducer to detect biochemical substances. The system structure and working principle of a biosensor is demonstrated in Figure 2.1. The bioreceptor element is a biologically derived or biomimetic component that captures and recognizes the sensing target through highly specific binding or other biochemical integrations. Once recognized, the physicochemical signal generated by the biochemical recognition reaction is converted by the transducer into other forms, which can be amplified and processed for detection. The bioreceptor is versatile in its sensing elements, which can be composed of antibodies, aptamers, cell receptor, enzymes, molecularly imprinted polymers, microorganisms, nucleic acids, and whole cells, etc. According to different sensing principles, biosensors can be categorized into many forms, including electrochemical, optical, mechanical, and magnetic biosensors, which are discussed in detail in the following part of this section.

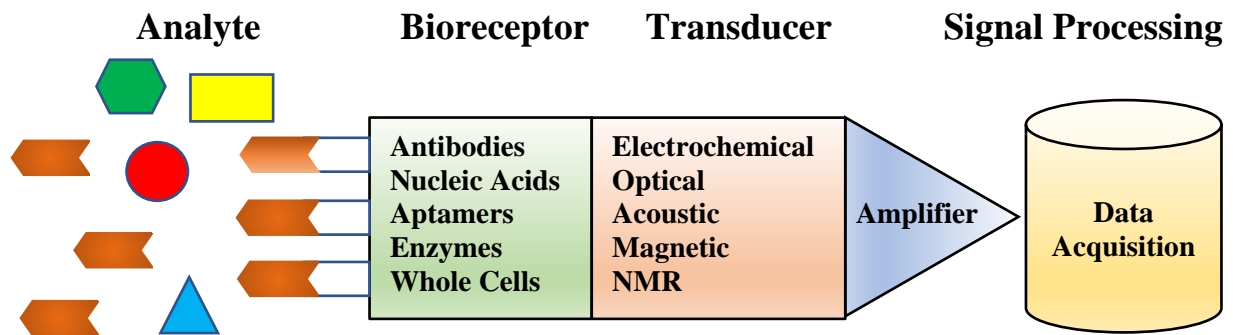


Figure 2.1 Schematic diagram and working principle of a biosensor system.

2.2.1 Acoustic Biosensor

The acoustic biosensor is based on piezoelectric crystal, a unique material capable of transforming mechanical vibration into electrical energy, and vice versa. During the sensing, an alternative current (AC) is applied to excite standing wave in the crystal. The resultant resonant vibration has a characteristic frequency, which is highly sensitive to the surface properties of the crystal. Hence, if the crystal is functionalized with a bioreceptor, once the sensing target is captured, it will cause a shift in the resonant frequency due to the mass change as shown in Figure 2.2.

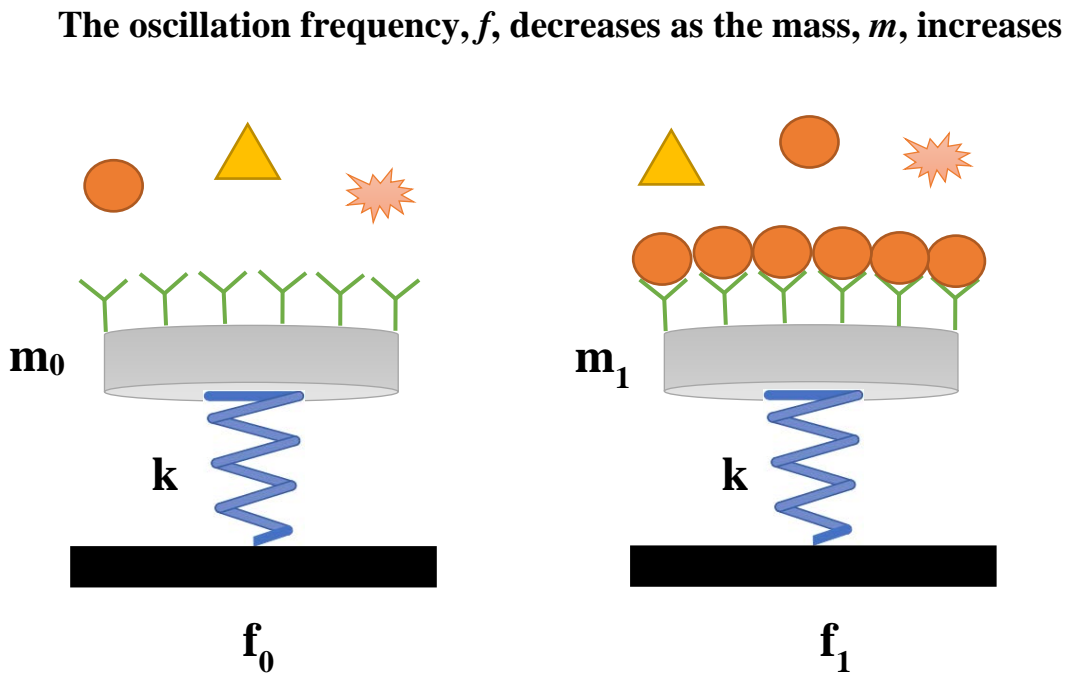


Figure 2.2 The oscillating frequency is inversely proportional to the mass as indicated by the spring-mass oscillator system as an example.

The mass change has a linear relation with the frequency shift as indicated by the Sauerbrey equation (Equation 1) [26], which can be used to quantify the target concentration.

$$\Delta f = -\frac{2.3 \times 10^6 f_0^2}{A} \Delta m \quad \text{Equation 1}$$

where, Δf is the frequency change in Hz, f_0 is the resonant frequency of the crystal in MHz, and A is the coating area in cm^2 , and Δm is the captured mass in grams.

Acoustic immunosensors have been reported, of which immuno assay is functionalized on the crystal surface as the sensor's bioreceptor. Muratsugu et al. developed a quartz crystal microbalance (QCM) biosensor using antibody specific to human serum albumin to form a label free assay. It successfully detected albumin in urea (albuminuria) in a range 0.1–100 $\mu\text{g/mL}$ [27]. In another research, a QCM immunosensor was developed by Deng and coworkers to detect a protein in human, the complement component 4 (C4) [28]. The working electrodes were modified with nafion membrane and then by the target-specific antibody. Detection range of 0.08–1.6 $\mu\text{g/mL}$ and relative standard deviation around five percent were achieved [28]. Funari and coworkers reported another QCM immunosensor, of which spatially oriented antibodies against gluten were functionalized on gold electrodes. It reached sensitivity limit of 4 ppm for the gluten and detection range between 7.5 and 15 ppm [29].

In summary, the acoustic biosensor can be of low cost and durable since piezoelectric crystals are abundant, inexpensive, and robust, which is suitable for biosensor applications under challenging physiochemical conditions with low cost. In addition, the acoustic biosensor provides great flexibility, wide dynamic sensing range, and is capable of label free detection. The acoustic biosensor has a limitation in detecting low molecular weight analytes because they cause lower decrease of oscillation frequency. Besides, the sensitivity is not ideal for detecting large analyte,

such as microbial cell, because it does not act as an ideal mass point and only the portion in the proximity of the bioreceptor is involved in frequency change of oscillations [30].

2.2.2 Electrochemical Biosensor

The electrochemical biosensors convert chemical information from bioreceptor events into various form of electrical signals, such as potentiometry, amperometry, impedance, capacitive, or conductometry. The working principle and system structure of the electrochemical biosensor is demonstrated in Figure 2.3 [31]. It measures the conductance of ions or electrons in a sample solution or fibrous network using inert electrodes, direct or alternating current, and an alternating null current.

The electrode is a major component, which is responsible for the binding of target biomolecules and the transport of electron/ions. Label-free application has been developed based on different electrochemical sensing techniques, such as impedance spectroscopy for DNA detection using single walled carbon nanotubes (SWCNTs) as support for DNA probe [32], and electrical conductometry using graphene support with rGO/AgNP composites [33], etc. For labelled application, binding molecules, such as antibodies, enzymes, or aptamers, can be used to conjugate signal probes on the sensing target to further amplify or transduce the binding event into signals to be easily measured and quantified. Recently, new material has been studied including carbon-based nanomaterial, such as SWCNT, multi-walled CNT (MWCNT), and graphene; and non-carbon nanomaterials, such as metallic nanoparticles, porous silica, nanowire, indium tin oxide (ITO), and organic polymers, etc. A ratiometric electrochemical biosensor was developed by Cai et al. using Polythionine–Gold (PTh–Au) as an electrode. It can detect a tumor marker,

carcinoembryonic antigen (CEA), with good specificity within a wide linear range, and a detection limit of 2.2 pg/mL [34]. Owing to the large surface area to volume ratio and unique mechanical and electron transport properties, synergic improvements are achieved in sensing performance and analytical sensitivity by enhanced loading capacity and increased mass transport of reactants.

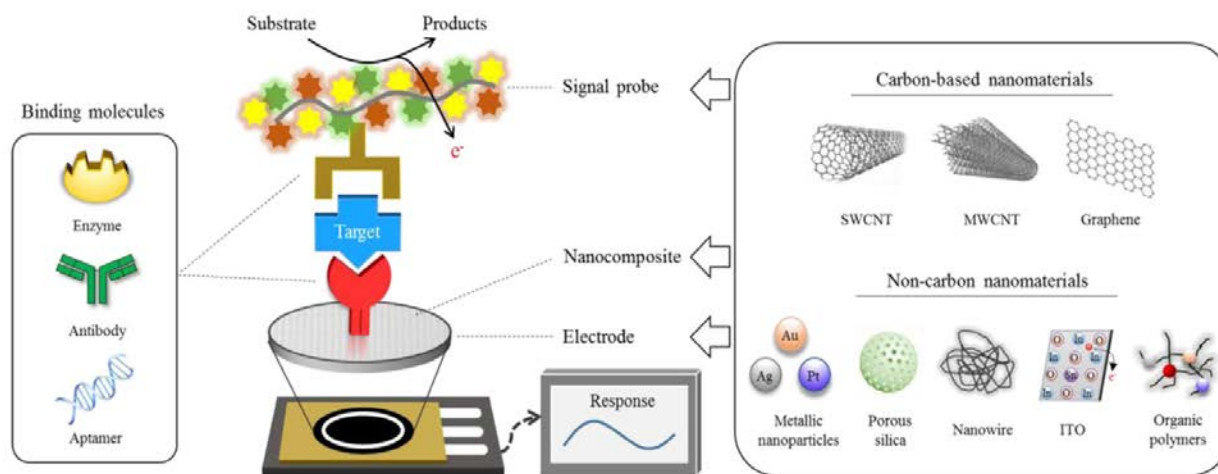


Figure 2.3 Scheme of sensor operating principle for electrochemical biosensors (adapted and modified from [31]).

2.2.3 Optical Biosensor

The optical biosensor utilizes an optical transducer to detect the target analyte under study. Various types of bioreceptors adopted in other biosensor platforms can also be used in their optical counterparts, including antibodies, antigens, enzymes, nucleic acids, receptors, whole cells and tissues. The optical transducer then detects the recognition events by measuring the evanescent field in close proximity to the biosensor surface in terms of surface plasmon resonance (SPR), evanescent wave fluorescence, or optical waveguide interferometry. The working principle and system structure of the electrochemical biosensor is demonstrated in Figure 2.4.

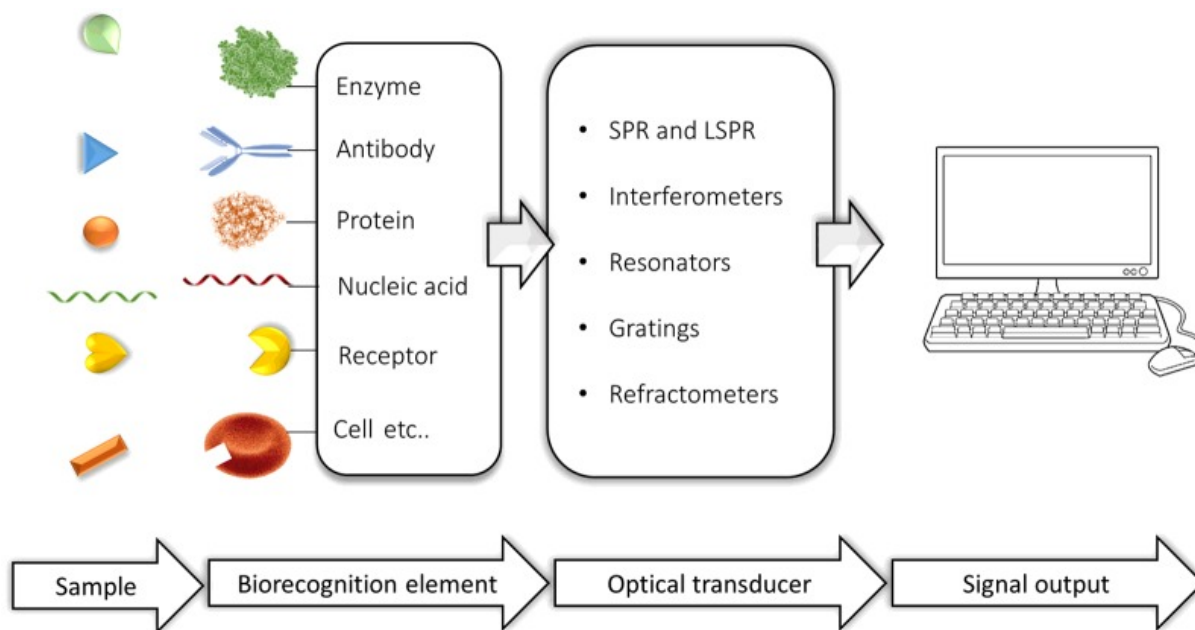


Figure 2.4 Scheme of sensor structure and operating principle for optical biosensors (adapted and modified from [35]).

The sensing of the optical biosensor relies on the number of biorecognition and optical transducing events. Hence, changing material structure or increasing surface area and porosity to enhance the amount of radiation reflected or emitted are beneficial to improve sensitivity. Nano materials, such as nano particles and nano fibers, are promising to achieve such improvements owing to their versatility and unique nanostructure.

Optical biosensors are relatively new, and their importance is expected to grow in healthcare and pathogen detections. They can enable large-scale high-throughput testing of multiple samples simultaneously. However, optical biosensors for general practical application are still under development. Their current applications are still limited to academic and pharmaceutical environments.

2.2.4 Immunoassay Biosensor

Immunoassay biosensor adopts antibodies as the bioreceptor with advantage of the high selectivity provided by the molecular recognition and binding between antibody and antigen. The immunoassay biosensor can be generally categorized into two types: label-free and labeled. The label-free application relies on detecting the physical changes directly induced by the antibody-antigen complex. The labeled application adds a sensing label to the antibody-conjugated target, forming a sandwich structure to amplify or transduce the original conjugation event. Their transducers have a variety of sensing forms, such as optical sensing including luminescent, fluorescent, and surface plasmon resonance, electrochemical sensing including voltammetry, amperometry, and impedance spectroscopy.

Owing to the continuous advancement of instrument electronics, the size and cost of the sensor transducer have been reducing over the years and is technically ready for portable applications. The bioreceptor remains the crucial part to be further improved on sensitivity and detection time to fulfil the requirements for water and food testing. Enhancing the surface area of the biosensor is an effective approach through maximizing the number of reaction sites. Hence, nanomaterials of electron nanofibrous membrane and magnetic nanoparticle are the promising solution that provides these advantages, owing to their excellent surface to area ratio and unique nanostructures. Immunoassay biosensor has recently been developed based on nanofibers, polymers, nanoparticles, CNTs, and graphene [36]-[40]. Fellows and coworkers developed a rapid lateral flow assay (LFA) based on streptavidin-conjugated gold nanoparticles (AuNPs) as reporter molecules to screen single-stranded DNA aptamers for the detection of a glycoprotein, cluster of differentiation 4 (CD4). The sensor was able to detect 250 ng of human CD4 in 9 min [41]. A

lateral flow immunoassay (LFI) to detect proteins was developed by Qiu and coworkers utilizing antibody functionalized CNTs as a colored (black) tag [42]. The capture antibodies on the test zone of LFI captured target proteins, and then immobilized the CNTs labelled by detection-antibodies, resulting in a black colored line on the LFI to enable visual detection of protein. It could detect rabbit IgG in spiked human plasma in 20 min with sensitivity limit of 1.3 pg/mL [42]. Zheng and coworkers developed a label-free immunosensor based on electrochemiluminescent (ECL) to detect β -Trophin protein [43]. AuNPs were linked on the indium-tin oxide substrate via (3-aminopropyl) trimethoxysilane based polymer to enhance ECL and immobilize the β -Trophin antibodies. The detection time was approximately 2 hours. The detection limit of β -Trophin was 1.26 ng/mL [43]. Shi and coworkers developed a portable lateral flow assay (LFA) biosensor to simultaneously detect neomycin (NEO) and quinolones antibiotics (QNS) based on immunonanoprobes and surface-enhanced Raman scattering (SERS) detection [44]. The LFA achieved sensitivity limits of 10 ng/mL for NEO and 200 ng/mL for NOR using visual detection, and 0.37 pg/mL and 0.55 pg/mL using SERS [44]. Gondhalekar and coworkers developed a laser-induced breakdown spectroscopy (LIBS) for lateral-flow immunoassays (LFIA) to detect *E. coli* using labels of AuNP or lanthanide-complexed polymers (LCPs) [45]. The LIBS system was applied on a commercial LFIA (based on nitrocellulose membranes) to detect AuNP labeled *E. coli*. It achieved a sensitivity limit of 8.89×10^3 CFU/mL in approximately 3 hours of total testing time [45]. Compared to chemical synthesis methods of nanomaterials, the electrospinning technology has unique advantages to fine tune fiber properties with ease, such as fiber compositions, orientation, diameter, and length, etc. The capability of the fibrous membrane, including surface area and capillary action, can be optimized for binding, filtration, and signal transducing to improve biosensor performance.

2.2.5 NMR based Microorganism Detection

Nuclear magnetic resonance (NMR) is a physical phenomenon of which atomic nuclei absorb and reemit electromagnetic radiation at certain frequency when placed in a magnetic field. NMR technique exploits this phenomenon by analyzing the magnetic properties of atomic nuclei to determine physical and chemical properties of biomolecules. Since its sensing signal is able to pass through turbid raw samples, simplifying sample preparation processes and saving analysis time, NMR techniques have wide applications in non-contact and non-destructive biomedical and food diagnoses [46]. In standard testing, NMR analysis were performed in laboratories using a strong stationary magnet, in which the sample of interest was placed inside [47]. Although the system produced accurate results, the magnet and instruments were rather expensive, heavy, large, and unportable [47][48]. This makes the NMR technique less useful and less practical for on-site applications. However, continuous development has led to the advancement of portable NMR (pNMR) detection hardware and sensing performance. pNMR sensors were developed using magnetic nanoparticles and microparticles as proximity sensors to amplify molecular interactions [49]. Their sensing is based on the reversible self-assembly of dispersed magnetic particles into stable nano-assemblies [49]. When a few magnetic nanoparticles conjugate to their molecular target through affinity ligands, they form magnetic clusters which result in a corresponding decrease in the bulk spin-spin relaxation time (T_2) of its surrounding water molecules [50]. Their measurements can be performed on turbid samples with simplified sample preparation. Furthermore, the sensing is faster than those by surface-based techniques, which relies on molecular diffusion of targets to the sensing elements. These advantages make the proximity assay ideal for fast, simple and high-throughput sensing applications, especially in miniaturized device format. Such type of sensors is smaller in size and suited for on-site and field applications. They

are also cheaper to manufacture and less costly to maintain as compared to the bulky conventional NMR systems. A portable NMR system for a noninvasive spin-echo imaging of living plants in their natural environment was reported in 2000 [51]. Recent advances in micro-fabrication technologies have accelerated the development of palm-sized NMR and high-throughput NMR transceivers. The palm-sized NMR was based on integrated circuit (IC) technique and was tested in detecting biological molecules and cancer cells by measuring the sample's NMR relaxation time which was inversely proportional to the immuno-clustering of magnetic nanoparticles [50]. The reported sensitivity for detection of cancer cells was in the range of 10^3 to 10^4 cells/mL [52]. Other portable NMR developments include different designs [47]-[49][51][53][54]. Hash and coworkers developed an NMR biosensor to detect *Vibrio parahaemolyticus* bacterium spiked in shrimp tissues [55]. The detection started with DNA extraction from test samples. Iron nanoparticles coated with target-specific biomarkers were applied to bind with *V. parahaemolyticus* DNA, which could be detected by molecular mirroring NMR technology [56]. The NMR biosensor output spin-spin relaxation time, T_2 , which correlated with the quantity of the *V. parahaemolyticus* DNA. The biosensor could detect different quantities of *V. parahaemolyticus* DNA, which was equivalent to cell concentrations ranging from 10^5 to 10^8 CFU/mL in approximately 1 hour of testing time [55]. An on-chip probe-based portable NMR was developed by Gupta and coworkers to detect a malaria parasite, parasitaemia *Plasmodium falciparum* in human blood [57]. The system utilized a permanent magnet of 0.5 Tesla to detect the NMR signal of water proton. The signal frequency was 21.287 MHz. The NMR probe was designed combining a planar circular coil antenna and a matching network (a L-section circuit with a shunt capacitor and a series capacitor). After capacitor tuning, the quality factor of the probe was optimized and measured as 24.407, using the same measurement method as described in Section 5.2.5. The NMR sample volume was 15 μ L. T_2

differences between test samples of control (blank) and parasitaemia were measured to determine the target concentration. The NMR biosensor achieved a sensitivity limit of 0.0001% parasitaemia, the percentage of infected red blood cells used to monitor the infection progress and the patient recovery. This was at the same level as their PCR results and was lower than the other methods that they conducted for comparison, including blood smear, fluorescence activated cell sorting, SYBR Green staining [57]. Gossuin and coworkers studied using low-field (0.5 Tesla and 1 Tesla) NMR T_2 sensing to detect the synthetic malaria pigment β -hematin based on its own paramagnetic effect on water proton (without adding superparamagnetic MNPs for signal amplification) [58]. It could detect β -hematin with concentration of 3.88 mg/ml. The result indicated that paramagnetic particles were more difficult to detect by NMR than the superparamagnetic particles. The paramagnetic effect of β -hematin on relaxation decay was not enough to accurately detect malaria without the use of a large-field magnet, T_2 (not T_1), constant temperature, or any preliminary sample preparation, such as microcentrifugation [58]. Lu and coworkers developed a low-field microfluidic NMR device (0.443 Tesla) to detect tumor markers using immunomagnetic nanoparticles (IMNPs) [59]. A multi-layer microfluidic NMR probe (probe diameter of 1.7 mm) was designed for sample transport and detection. The matching network was of the same design as described in Section 5.2.5. The device utilized a commercially available electronic control system (Bruker minispec console) as the NMR transceiver. The transverse relaxation time change ΔT_2 was measured to determine the target concentration in approximately 1 hour. It detected three biomarkers, respectively, and achieved sensitivity limit of 10^{-1} ng/mL and linear response from 10^0 ng/mL to 5×10^2 ng/mL for immunoglobulin G (IgG), sensitivity limit of 5×10^{-1} ng/mL and linear response from 10^0 ng/mL to 10^2 ng/mL for mucin glycoprotein 1 (MUC1), and sensitivity limit of 10^1 cells/mL and linear response from 5×10^2 cells/mL to 5×10^4 cells/mL for human breast

adenocarcinoma cell line (MCF-7) [59]. Janis and coworkers developed a novel two-dimensional NMR sensor with a microfluidic diamond quantum sensor [60]. The microfluidic chip transported the sample through a medium low field (1.5 Tesla Halbach magnet) for prepolarization, and subsequently tested it inside using a low field ($B_0 = 13$ mT, Helmholtz coils). The NMR sensor utilized optically probed nitrogen-vacancy (NV) quantum defects in diamond, excited by a linearly polarized 532-nm green laser beam, to detect NMR signals with high-spectral resolution from micron-scale sample volumes. The NV NMR signal was detected using a custom-built epifluorescence microscope. It achieved 2D correlation spectroscopy of liquid analytes: trimethyl phosphate (TMP), or 1,4-difluorobenzene (DFB), within an effective detection volume of approximately 40 picoliter in a spectral resolution of 0.65 ± 0.05 Hz [60]. The development of a high-throughput NMR spectrometer used complementary metal oxide semiconductor (CMOS) technology to integrate an array of high sensitivity micro-coils with interfacing radio-frequency circuits on the same chip [61]. A micro nuclear magnetic resonance (μ NMR) relaxometer was also developed to miniaturize the sensing system to be palm-size with a portable sub-Tesla magnet, and electronically automate for multi-step and multi-sample chemical/biological diagnosis [67]. The μ NMR relaxometer utilized microfluidic and microelectronic technologies to enable the coordination between the droplet management and μ NMR assay detection. Targets in sub-10 μ L water samples, captured by specific probe-decorated magnetic nanoparticles, were sequentially quantified by their spin-spin relaxation time (T_2) via multiplexed μ NMR screening. An NMR relaxometer that can fit in a 2 mm by 2 mm silicon chip was also reported [54].

In order to minimize the pathogen infection and costly product recall, rapid, sensitive, and portable detection of *E. coli* O157:H7 is crucial in applications of healthcare and food supply. Studying

from the basic NMR design by Fukushima and Roeder [151], we developed a portable NMR (pNMR) and biosensor assay that can rapidly and sensitively detect foodborne pathogens. Our pNMR biosensor is novel in filtration assay, use of high signal-to-noise ratio but inexpensive NMR probe, and RF transceiver for microbial detection in complex matrices. The proximity biomarker uses an antibody-functionalized magnetic nanoparticle (Ab-MNP). The system is low cost and does not require skilled operators. It has high testing throughput, small size and high portability, which is suitable for in-field foodborne pathogen detection.

CHAPTER 3

SYNTHESIS AND CHARACTERIZATION OF MAGNETIC NANOPARTICLES

3.1 Introduction

Magnetic nanoparticles (MNPs) have promising properties in a wide variety of applications, which continue to attract research focus in recent years [61]-[65]. MNPs exhibit no net magnetization due to the random thermal flipping of magnetic moments but can be effectively manipulated by external magnetic fields. In addition, it can be functionalized by different affinity ligands, such as aptamers, lectins, folic acid, and epidermal growth factor (EGF), etc. [1][16]. MNPs can be conjugated to target cells or directly absorbed inside the cell for magnetically controlled non-destructive cell manipulation [69] and for lab-on-chip (LOC) applications [70].

MNPs have wide applications in medical diagnostics and treatments. After being manipulated or delivered to target tissue/cell, nanoparticles can be heated by an external alternating magnetic field as an experimental cancer treatment called magnetic hyperthermia [71]. MNPs can be used to target specific cells or tissues inside human body in order to accurately deliver drugs with optimal quantity [72]. MNPs can also be used to magnetically manipulate free-floating cancer cells to be carried out of the body for lab analysis [73]. For sensor applications, MNPs can be used to extract target pathogen or biomaterial from supernatant solution as the magnetic separation for sample purification and concentration [74] [75]. Electrochemical detection using magnetic nanoparticles has been developed to form immunoassay with target pathogen, and measure cyclic voltammetry (CV) signals or electrical conductance signals [76][77].

Magnetic nanoparticles synthesis has been established by different chemical process including: co-precipitation method [78], microemulsion method [79] and flame spray synthesis method [80] to achieve different core and shell material/composition, particle size, magnetization, and electrochemical properties. This chapter describes synthesis methods of two magnetic nanoparticles, which were developed in the lab, for conductance biosensor and NMR biosensor applications, respectively.

3.2 Materials and Methods

3.2.1 Synthesis of Conductive Immunomagnetic Nanoparticle

The conductive immunomagnetic nanoparticles were synthesized from gamma iron (III) oxide (γ -Fe₂O₃) nanoparticles as core, and polymerized aniline as shell, which was biologically and electrically activated by acid doping [1] [82] [83]. The γ -Fe₂O₃ (maghemite) nanoparticles, which were purchased from Sigma-Aldrich (St. Louis, MO), were dispersed in a mixture of 50 ml 1M HCl, 0.4 ml of aniline monomer and 10 ml de-ionized water, and sonicated at 0°C for 1 hour to disintegrate the cluster. Then a slow drop-wise addition of the oxidant, ammonium persulfate ((NH₄)₂S₂O₈), at a rate of 0.1 ml/min was added to this solution mixture with constant stirring. The solution color changed from rust brown to dark green which indicated the formation of the conductive emeraldine form of polyaniline (green) coating on the smaller γ -Fe₂O₃ nanoparticles (brown). This reaction continued for 4 hours with constant stirring at 0°C. Finally, the green solution was filtered and washed with 1M HCl, and 10% methanol and diethyl ether. The filtered product was dried for 18 hours at room temperature. The synthesis of conductive immunomagnetic nanoparticles is demonstrated in Figure 3.1 below. The polymerization and acid doping process

were determined to obtain a uniform nanoparticle size and optimized magnetisms and conductivity to be used for the electrospun lateral flow biosensor.

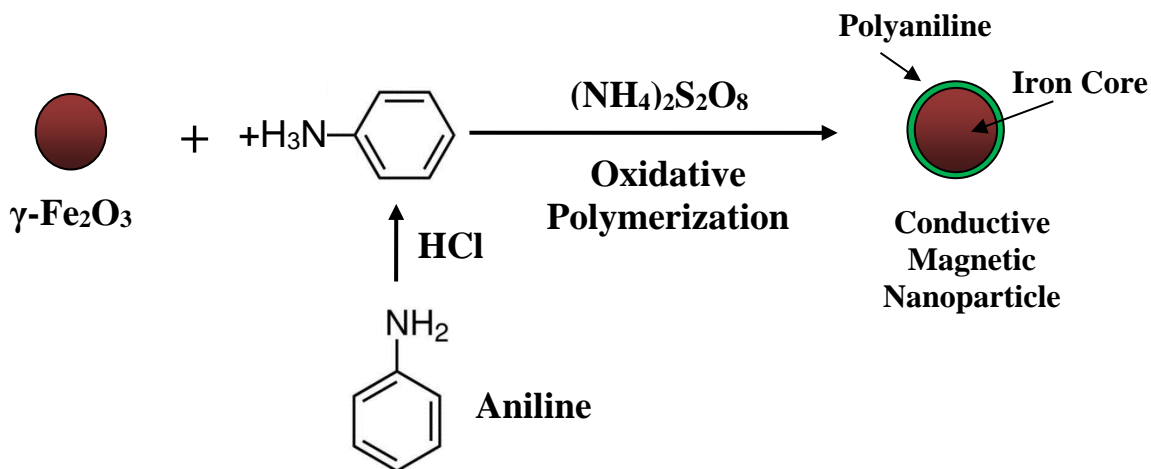


Figure 3.1 Synthesis of conductive immunomagnetic nanoparticles by encapsulating gamma-iron oxide ($\gamma\text{-Fe}_2\text{O}_3$) nanoparticles with polymerizing aniline as conductive nano-shell.

3.2.2 Synthesis of NMR Magnetic Nanoparticle

The NMR biosensor detects target pathogen concentration by measuring the sample's ^1H NMR relaxivity, which is determined by magnetic field alternation from the pathogen and magnetic nanoparticle conjugation. The smaller and more uniform nanoparticle with higher magnetism is capable to increase conjugation ratio per pathogen and enhance the whole conjugation's magnetization, which is critical to the sensitivity of NMR biosensor.

Hence, for NMR application, amine-functionalized Fe_3O_4 (magnetite) magnetic nanoparticles (AMNPs) were synthesized separately in the lab based on thermal decomposition of Fe-chloride method [85], with improvement modifications. First, 1.08g of iron (III) chloride hexahydrate ($\text{FeCl}_3 \cdot 6\text{H}_2\text{O}$), 2g of sodium acetate and 7 ml of ethylenediamine were added in 30 ml of ethylene glycol for 2 h at room temperature to obtain a homogenous golden yellow mixture. The solution was transferred into a teflon-lined stainless-steel pressure vessel (Parr Instrument Company, Moline, IL) to be sealed and heated at 200°C for 15 h for thermal decomposition dehydration and Fe_3O_4 reaction. After cooling to room temperature, the synthesized nanoparticles were thoroughly cleaned by magnetic separation of three times of 20 ml water wash and three times of 20 ml ethanol wash. During each clean step, samples were placed inside a strong permanent magnet to remove the supernatant. Finally, the synthesized magnetic nanoparticles were dried under vacuum for 12 h.

3.2.3 Magnetic Nanoparticle Characterization

The synthesized conductive immunomagnetic nanoparticle and NMR amine nanoparticle have been characterized to evaluate particle size, conductivity and magnetic capability [82]. A high performance TEM, JEOL 2200 FS, with field emission cathode and acceleration voltage of 200 kV was used to investigate particle structure, size, and content uniformity. Both particles' magnetic properties were measured using a superconducting quantum interference device, MPMS SQUID (Quantum Design Inc., CA). And hysteresis magnetization was measured by cycling magnetic field from +15 kOe to -15 kOe, at constant temperature of 300 K. A four-point probe, Pro-4 (Lucas/Signatone Corp., CA), was used to evaluate polyaniline (PANI) particle's electrical

conductivity at room temperature, which uses separate pairs of current-carrying and voltage-sensing electrodes to increase accuracy.

3.3 Results and Discussion

3.3.1 Magnetic Nanoparticle Characterization and Synthesis

The electrical conductance of the conductive PANI magnetic nanoparticle was measured by four-point probe measurements to be 3.3 S/cm (+/- 0.04 S/cm, n = 3) at room temperature, whereas unmodified γ -Fe₂O₃ nanoparticles indicated 3.4×10^{-5} S/cm (0.17 S/cm standard deviation, n = 3) conductivity under the same measurement. The high conductivity of the synthesized PANI magnetic nanoparticles confirmed the insulator-conductor transition into the electrically active polyaniline. At 300 K temperature, the conductive PANI magnetic nanoparticles exhibited saturation magnetization of 44.1 emu/g measured at a magnetic field of 15 kOe using a SQUID magnetometer, while unmodified γ -Fe₂O₃ nanoparticles showed 64.4 emu/g measured under the same conditions. The magnetization reduction can be explained by a bipolaron conduction mechanism that caused conductive polyaniline to be diamagnetic [84]. However, the nanoparticles' magnetization is more than sufficient for the intended biosensor application of immuno magnetic separation. Transmission electron microscopy (TEM) studies confirmed the effective coating of PANI around the γ -Fe₂O₃ particles. The synthesized conductive PANI MNPs indicated a controlled diameter ranging from 50 to 100 nm, whereas the unmodified γ -Fe₂O₃ nanoparticles from Sigma-Aldrich (St. Louis, MO) had an average diameter of 20 nm (4.6 nm standard deviation). It qualifies as NP because it meets the criteria of diameter between 1 and 100 nm [86]. Different weight ratios of γ -Fe₂O₃ to aniline of 1/0, 1/0.1, 1/0.2, 1/0.4, 1/0.6, and 1/0.8 were evaluated and finally determined to be 1:0.6 to optimize both size and conductivity. The

lower weight ratio resulted in MNPs with lower electric conductance (≤ 0.768 S/cm), while the higher ratio led to mostly amorphous shape and smaller saturation magnetization (≤ 33.5 emu/g).

The conductive PANI MNPs and the amine NMR MNPs both exhibited excellent superparamagnetic behavior, which can be uniformly distributed in solution or became highly magnetized when exposed to external magnetic field. As reported in the lab, the amine-functionalized NMR particles were highly mono-dispersing with diameter of 25 nm, which was verified by TEM imaging. The saturation magnetization significantly increased to 80 emu/g at 300 K, compared to PANI MNPs. Due to advantages in both particle size and magnetization, more amine MNPs can be effectively conjugated with the target pathogen each with stronger magnetism, which is important to NMR biosensor sensitivity.

3.4 Conclusions

In this chapter, conductive PANI magnetic nanoparticles and amine-functionalized NMR magnetic nanoparticles were successfully generated with sizes ranging of 50 to 100 nm and 20 to 30 nm respectively. Particle size and conductance were optimized for electrospun lateral flow biosensor application. Size and magnetization were optimized for NMR biosensor. The particles were successfully functionalized with antibodies and implemented for the biosensors for pathogen detection in Chapter 4 and 5.

CHAPTER 4

BIOSENSOR BASED ON ELECTROSPUN NANOFIBERS AND MAGNETIC NANOPARTICLES FOR PATHOGEN DETECTION

4.1 Introduction

Biocompatible materials, such as nitrocellulose, polyvinylidene fluoride, and polyether sulfone, are proven for their excellent binding capability and can capture biomolecule and pathogen cells to be separated from bio-samples. Low cost and high sensitivity biosensors have been developed based on immunoassay or immunochromatography for infectious pathogen detection [87], ovulation monitoring, drugs and chemical analysis in different applications [88], including veterinary testing [89], agricultural and environmental monitoring, and product quality evaluation [90].

Nanomaterials are promising to fabricate biosensors with high sensitivity, rapid response, and low cost, owing to their unique structure and biochemical properties. In recent years, research progress has been made in developing new nano biosensors to enhance surface area and reduce cross section, thereby providing a more effective immobilization to capture bio-targets [91][92]. Most of the development work is focused on using nanomaterials with two-dimensional or three-dimensional structured mesoporous layers. New sensor materials with one-dimensional (1D) structures have been introduced, such as carbon nanotube and metal oxide nanowires, providing unparalleled capability of rapid mass transfer for analyte molecules [93]. The 1D nanostructure has a significant advantage in surface to volume ratio, which leads to an excellent binding effect and sensor response. However, sensors composed of single nanowires or nanofibers suffer from

sensing variation due to their difference in size and diameter, which is difficult to control in nanofabrication. On the other hand, sensors consisting of nanowire/nanofiber networks can effectively average the response of each individual nanomaterial, providing advantages of reliable performance, low noise, and high reproducibility and repeatability.

Electrospinning is a versatile, high-throughput, and cost-effective technology to produce the nanofiber networks, or nanofibrous membrane with controlled and uniform fiber diameter in nanoscale [94]. Its fabrication relies solely on the use of high-voltage electrostatics to extract ultrafine solid threads from the material solution without the need for coagulation chemistry, high temperatures, or high pressure. Owing to novel nanostructure, the surface area of the resultant nanofiber is significantly increased compared to that of the conventional planar material, thereby enhancing both biochemical reaction rate and target binding effect [95]. In addition, the electrospinning technology provides many attractive advantages for the development of high-performance nanomaterials for biosensor applications, such as inherent stability, high yield, low cost, and compatibility with other micro fabrication processes [96]. For biomedical applications, such as tissue engineering [97], drug delivery [98], and artificial organ implants [99], electrospinning methods have been developed to fabricate nanofibers with biomimetic structures in different morphologies. Moreover, electrospun nanomaterials also demonstrated improved performance in molecular absorption [100] and cell adhesion [101], owing to their enhanced binding capability. In past years, their applications for biosensors have attracted extensive attentions and demonstrated promising testing results, such as biomolecular detection and enzyme functionalization [102]-[104]. However, electrospun biosensors for whole cell detection of microbial or viral pathogens have not been reported in prior literature.

This chapter presents a new electrospinning method to synthesize nitrocellulose nanofibrous membrane, and its optimization and functionalization techniques of biological treatment for biosensor application. A new biosensor based on electrospun capture membranes has been developed. It integrates multiple techniques including magnetic separation, capillary immunoassay, and direct charge electrical measurement to achieve rapid and quantitative detection of whole cell bacteria and virus.

The electrospun nanofibrous membrane was synthesized from nitrocellulose polymer solution. The process conditions and parameters of the electrospinning were optimized to obtain aligned fiber networks. The membrane was treated with a plasma to further improve capillary action and a surface antibody functionalization method was developed for the membrane and optimized for the target pathogen. The resulting membrane has an ultrafine fiber diameter of about 150 nm. The high surface area of the material enabled more bio-reception events to occur, facilitated lateral flow assay kinetics, thereby enhancing pathogen capture and separation from supernatant. Finally, the electrospun biosensor was tested using bacterial and viral inoculated samples to evaluate the binding and separation performance of the novel bio-modified nanofibrous membrane.

4.2 Materials and Methods

4.2.1 Electrospun Material Synthesis

The electrospinning process uses electrostatics repulsion effect generated by high voltage power source between the needle spinneret and collector to produce an ultra-fine nanometer polymer jet delivered by a syringe pump from a polymer composite material liquid, as shown in Figure 4.1.

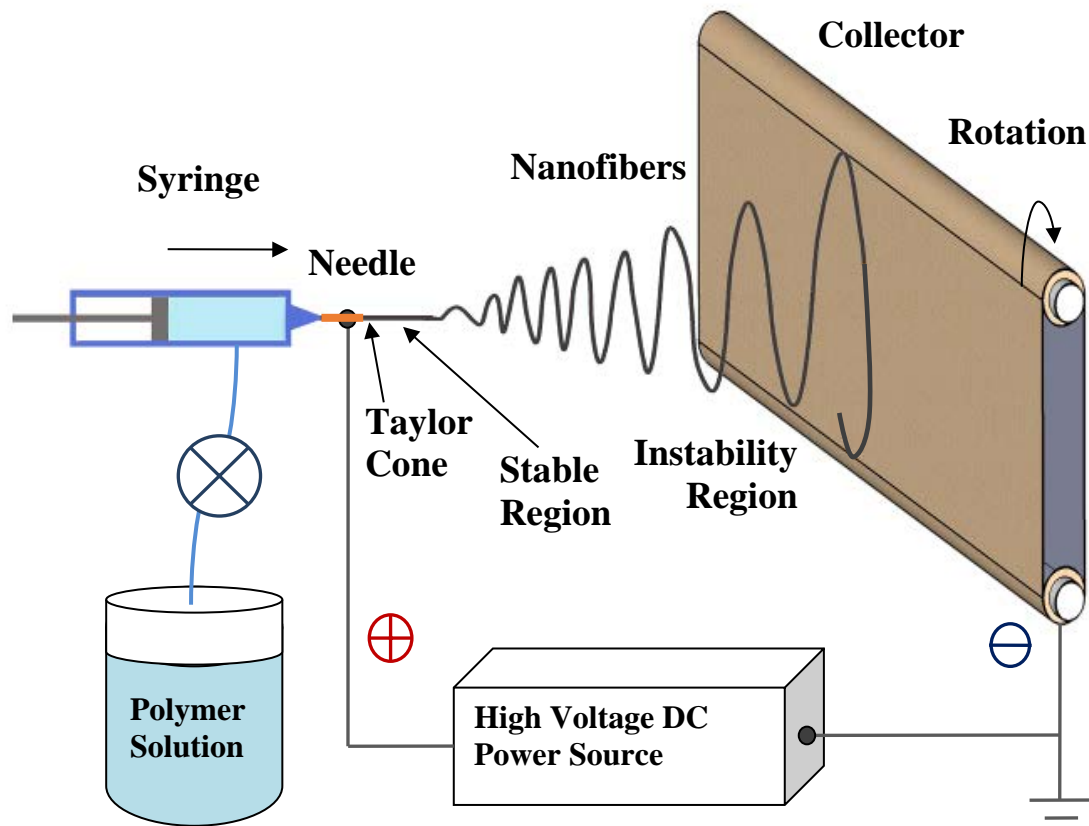


Figure 4.1 Schematic diagram of electrospinning setup for nanofibrous membrane fabrication, consisting of the syringe, the needle, the nanofiber jet (the Taylor cone, the stable region, and the instability region), and the rotating collector.

The electrospun nanofibrous membrane was fabricated using the Nanofiber Electrospinning Unit (NEU, Kato Tech Co. Japan), which is illustrated in Figure 4.2 below. The NEU device's high voltage power source can be adjusted from 0 to 39 kV, and self-contained for safety. The generated electrospun nanofiber was collected on its metal roller collector, which is capable to produce a uniform fiber membrane.

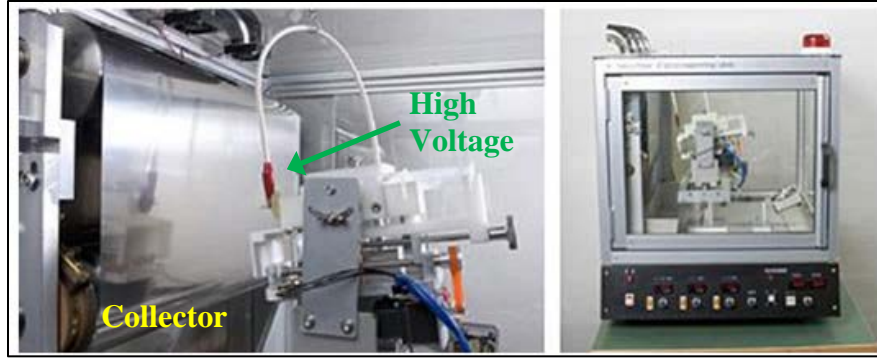


Figure 4.2 Self-contained Nanofiber Electrospinning Unit (NEU, Kato Tech Co. Japan) using rotating drum as collector for high yield fiber fabrication.

The electrospun biosensor membrane was fabricated using nitrocellulose polymer for its excellent biocompatibility and solubility in common solvent. The electrospinning process was controlled by the self-contained NEU device. Its fabrication conditions were optimized as follows, in order to control nanofiber diameter optimal for bio-detection. The nitrocellulose polymer of 8 wt% was dissolved in a mixed solvent system consisting of 60% tetrahydrofuran (THF) and 40% dimethylformamide (DMF), which provides optimal viscosity and surface tension for electrospinning [109]. A 20 ml syringe pump with 18-gauge needle was used to extrude the polymer solution at 0.2 ml/h. The applied high voltage between the needle and collector was tuned to be 10 kV and the distance was determined to be 6 cm. The polymer solution was electrospun on polyvinylidene chloride (PVDC) substrate into unwoven nanofibrous membrane. The fiber membrane quality was verified using Scanning Electron Microscope (SEM) imaging, which is demonstrated in Figure 4.3 below.

**Electrospun
Nanofiber**

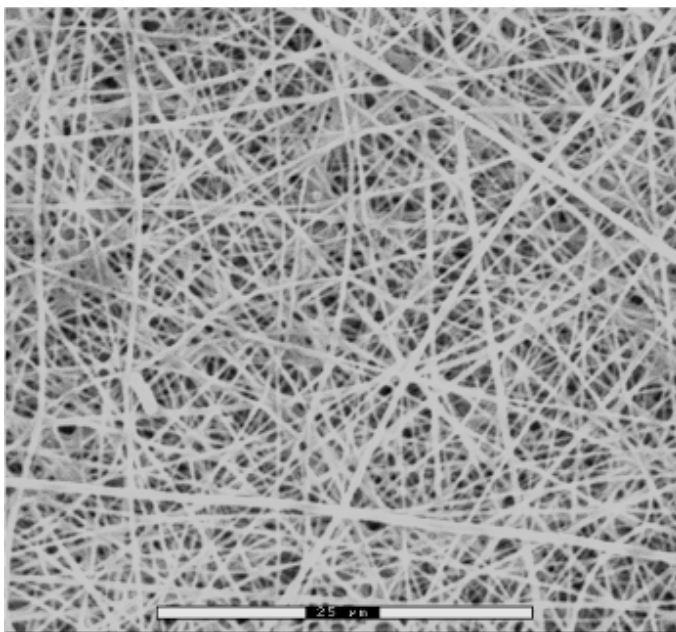


Figure 4.3 Scanning electron microscopy image of electrospun nitrocellulose nanofibers.

This electrospun fabrication system is capable to synthesize reproducible nanofibrous membrane made of 3D layers of smooth and defect-free nitrocellulose polymer nanofibers with uniform diameter of approximately 150 nm. When using the rotating drum collector, its synthesized electrospun fibers were typically in a random orientation, which limiting their capillary performance. A single parallel electrode pair used as collector enabled production of highly aligned mats to further enhance the capillary capability as shown Figure 4.4 below [111]. This unwoven membrane was uniform in fiber deposition depth and maintained surface and bulk chemical compositions which were expected for this material.

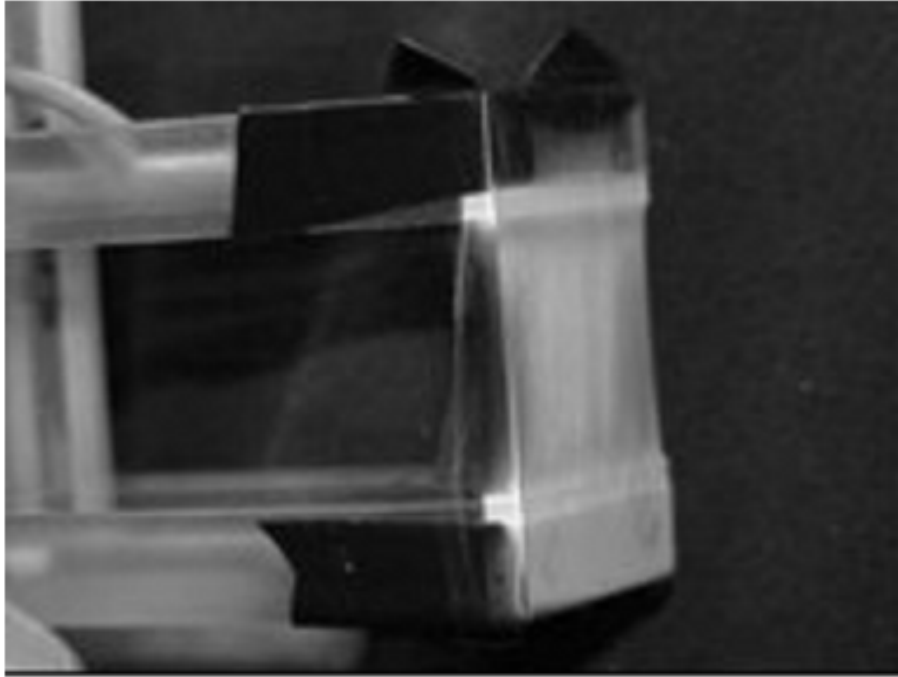


Figure 4.4 Nanofibers spun across the gap of a parallel electrode collector on the NEU unit

4.2.2 Plasma Enhancement for Capillary Flow

The IMNP electrospun biosensor utilized capillary flow and magnetic nanoparticle antibody conjugation to separate and detect biological target. In order to enhance capillary capability, surface nitrate groups of the electrospun nanofiber mat were removed by O₂ plasma using 120 W RF plasma at 13.6 MHz with O₂ at 250 mTorr, which was verified using X-ray Photoelectron Spectroscopy (XPS) spectrum analysis [109]. After plasma enhancement, the material property changed from hydrophobic to hydrophilic, and was verified by capillary contact angle test. As shown in Figure 4.5 below, before plasma treatment, contact angle between water droplet edge and nanofiber mat was 135°, which indicates that the surface was highly hydrophobic with low surface energy (>120°). After the plasma treatment, it changed to be 56° and indicated that the

electrospun mat became hydrophilic, which is good for capillary flow biosensor application ($< 90^\circ$).

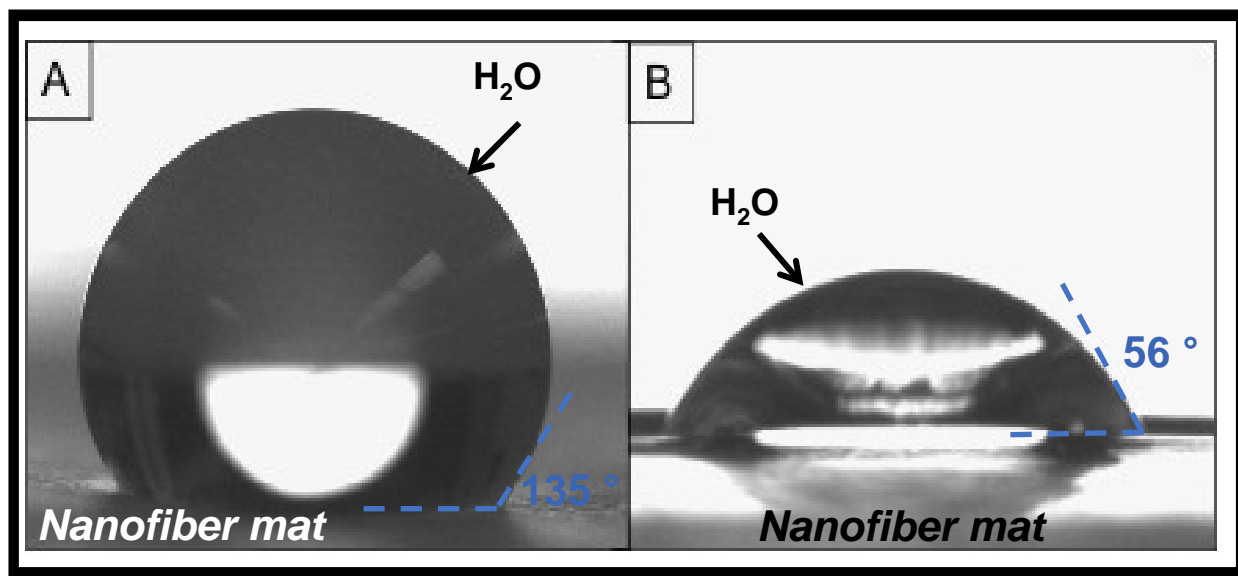


Figure 4.5. The capillary flow capability comparison of electrospun nanofibrous membranes (A) without and (B) with the plasma enhancement.

4.2.3 Sensor Architecture and Detection Principle

A conductometric lateral flow biosensor based on the electrospun material was designed to consist of three porous membranes: sample application pad, capture pad, and absorption pad [82]. The electrospun nitrocellulose membrane was implemented as the capture pad due to its excellent biocompatibility, surface area to volume ratio and capillary properties. The fiber surface was bio-modified for antibody attachment using glutaraldehyde ($\text{CH}_2(\text{CH}_2\text{CHO})_2$) as cross linker. A metal mask with pattern of parallel rectangular electrode pair was covered on top of the electrospun membrane. The colloidal silver ink was airbrush sprayed to fabricate a uniform silver electrode pair with gap distance of 0.5 mm. The mask protects the area between the electrodes from the corrosive silver ink solvent, which becomes the lateral flow channel of the capture pad as shown

in Figure 4.6. The sprayed electrode has uniform pattern and consistent resistance determined to be 1Ω . The chemical composition was carefully chosen to prevent the erosion of nanofibers.

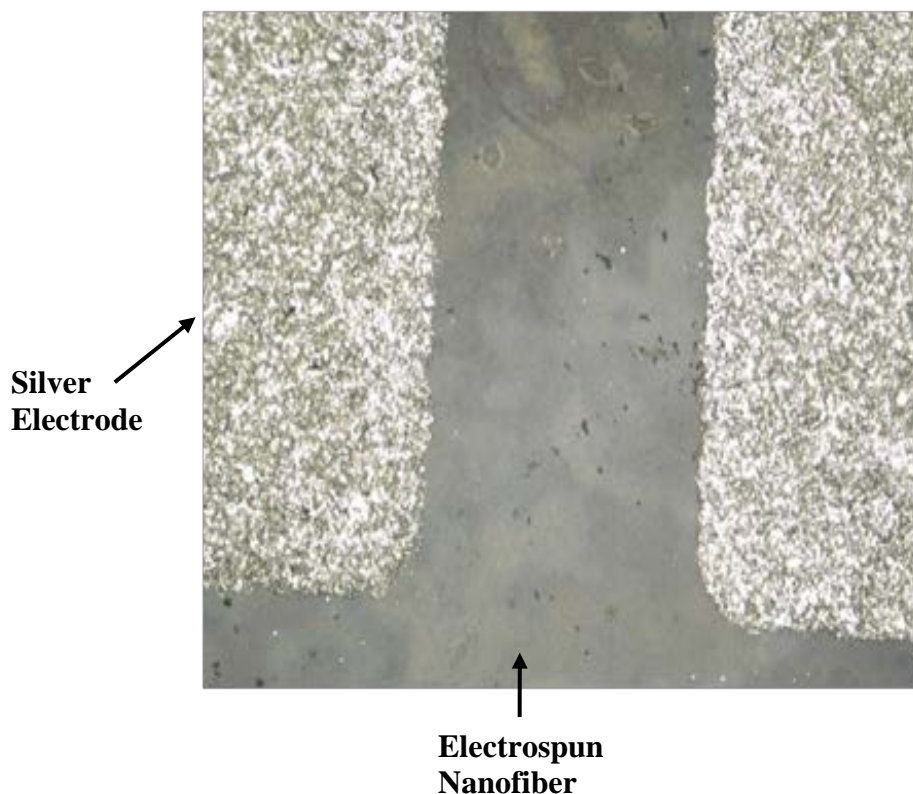


Figure 4.6 Silver electrodes fabricated on electrospun nanofiber membrane using spray deposition method.

The cellulose membranes with flow rate of 180 ml/min (Millipore, MA, USA) were used for the application and absorption pads due to their excellent filtration and sopping properties [110]. The application pad was used to control the flow of the sample onto the capture pad. The excess solution was absorbed in the absorption pad which modulated the capillary action. After cleaning with sterilized and deionized (DI) water, the application and absorption pads were cut into $7 \times 5 \text{ mm}^2$ and $10 \times 5 \text{ mm}^2$, respectively. Capillary experiments were performed to optimize the

membrane size for flow rate and sample volume. The larger pad sizes resulted in slower lateral flow across the application and absorption pads (> 20 min) and even partial flow stopped at the absorption or capture pad. The smaller pad sizes led to sample overflow on one or all three pads and unbound MNP to remain on the capture pad, which was verified in control (blank) sample testing through microscopy imaging. The optimized capture membrane had dimension of 23×5 mm² for a test sample of 100 μ L. The overall dimension of the IMP electrospun biosensor was 40×5 mm² (Table 4.1). Finally, the biosensor was assembled by attaching the three membrane pads onto a polyvinylidene chloride (PVDC) substrate via polystyrene adhesive backing as shown in Figure 4.7 below. The biosensor unit was connected to a data acquisition system linked to a computer via copper wiring substrate to measure the resistance of the biosensor which would indicate the target pathogen concentration (National Instrument, TX, USA).

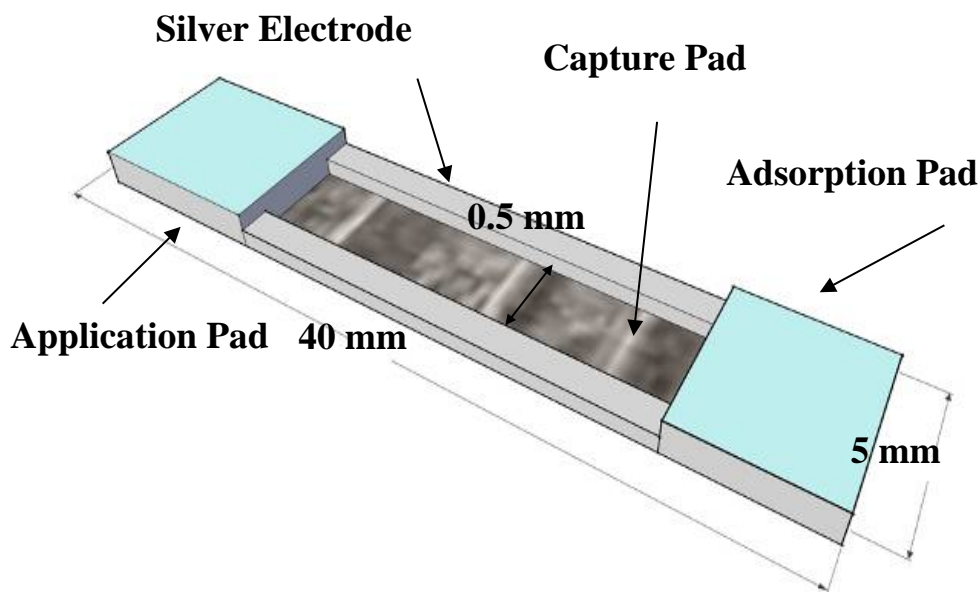


Figure 4.7. Schematic of the biosensor structure and membrane assembly consisting of cellulose application and adsorption pads and electrospun cellulose nitrate capture pad.

Table 4.1 Dimension of the biosensor and its components

Biosensor zone	Dimension (mm)
Application	7×5
Capture	23×5
Absorption	10×5
Overall	40×5

The pathogen detection principle of the biosensor is demonstrated in Figure 4.8. The antibody-modified conductive MNPs were mixed and incubated with the test sample to conjugate with the target pathogen. Then, the test sample was purified using magnetic separation process for 3 times [82] by holding the magnetically susceptible conjugation complex close to an external magnet to extract the supernatant by pipette. The purified sample, which was also conductively labeled by the MNPs, was dispensed on the application pad and initiated the lateral flow. The porous structure of the application pad modulated the flow and filtered large sized impurities. During the flow, the target pathogen was conjugated by the antibody in the electrospun membrane and captured in the capture pad. The non-target biomolecule and excess magnetic nanoparticles in the solution were subsequently removed by the capillary action and absorbed in the adsorption pad. Finally, when the entire process reached equilibrium, the conductive MNPs captured in the electrospun membrane were proportional to the target concentration since the sample volume is constant. Thus, the presence and concentration of pathogen could be determined by measuring the conductance signal of the membrane via its two silver electrodes, as shown in Figure 4.19 in the following section 4.3.

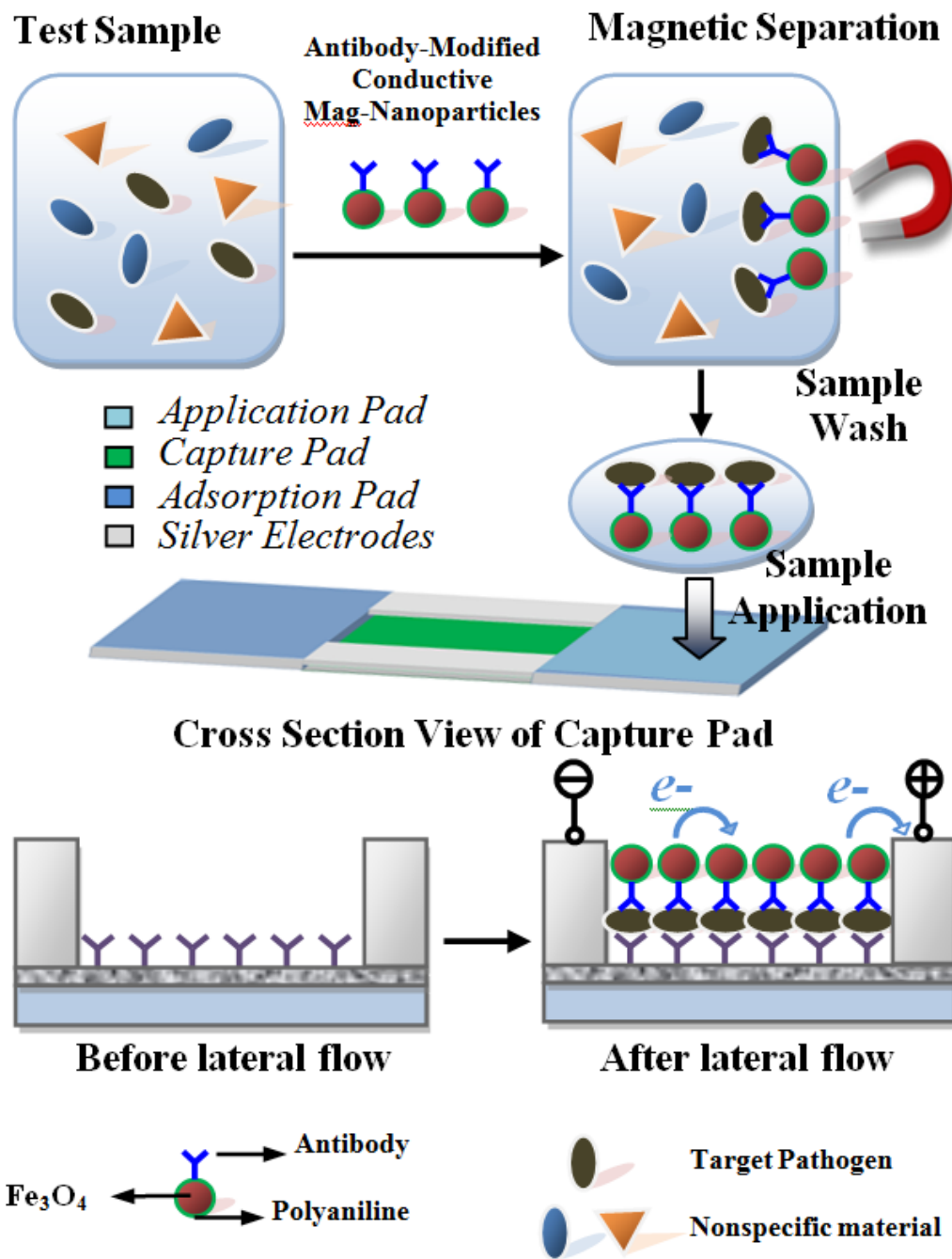


Figure 4.8. Detection scheme of the lateral flow immunosensor based on immunomagnetic nanoparticle and electrospun antibody functionalized capture membrane.

4.2.4 Test Pathogens and Antibodies

4.2.4.1 *Escherichia coli* O157:H7

A pure culture of *Escherichia coli* O157:H7 was obtained from the collection of the Nano-Biosensors Laboratory (Department of Biosystems and Agricultural Engineering, Michigan State University). To make a stock culture, *E. coli* O157:H7 test strains were inoculated using sterile loop into 10 mL of Tryptic soy nutrient broth from the Difco Laboratories (Detroit, MI) and incubated for 24 h at 37 °C. The 24 h stock culture was serially diluted in 0.1% peptone water in logarithmic scale to obtain different concentrations from 10^1 to 10^7 colony forming units per milliliter (CFU/mL). Each dilution was used as a test sample during the succeeding biosensor detection experiments.

The antibodies used for *E. coli* O157:H7 biosensor were an affinity purified goat anti-*E. coli* O157:H7 polyclonal antibodies from KPL, Inc. (Gaithersburg, MD), and purified mouse anti-*E. coli* O157:H7 monoclonal antibodies from Meridian Life Science, Inc. (Saco, ME).

4.2.4.2 Bovine Viral Diarrhea Virus

In addition to the bacterial pathogen detection, the biosensor was also evaluated to detect a viral pathogen, Bovine Viral Diarrhea Virus (BVDV). It is of genus Pestivirus of the family Flaviviridae, including BVDV1 and BVDV2. The virus consists of an envelope and a nucleocapsid in spherical shape. It has nano size with diameter ranges from 40 nm to 60 nm [113].

The BVDV not only infects bovine, but also various breeds of domestic and wild ruminants and pigs. In acute infections, BVDV can result in respiratory and reproductive symptoms, and enteric

symptoms, such as diarrhea and almost always immune suppression, causing the animal vulnerable to secondary infections. Some strains of BVDV leads to persistent infections without active symptoms for a long time. It is of greater harm as a major source to infect BVDV to the herds. Hence, the United States Department of Agriculture (USDA) urges the need of effective surveillance programs to reduce BVDV infections in the national heard, and reliable methods to detect both persistent and acute infections. The USDA states that “robust field-ready tests that both detect and differentiate viral pathogens” is needed in order to achieve this [114].

Samples of bovine viral diarrhea virus (BVDV) in serum were collected from BVDV-infected cattle maintained by the Department of Large Animal Clinical Sciences at the Michigan State University. These BVDV samples were stored at -80 °C before use. A BVDV test solution was thawed and serially diluted four times to get 10^{-1} , 10^{-2} , 10^{-3} , and 10^{-4} dilutions prior to use. Each dilution was used as a test sample during the succeeding biosensor detection experiments.

The antibodies used for the BVDV biosensor were affinity purified mouse anti-BVDV 15c5 (gp48) monoclonal antibodies (Ed DuBovi, Cornell University, Ithaca, NY) and purified swine anti-BVDV polyclonal antibodies (USDA National Animal Disease Center, Ames, IA). All the experiments were performed in a certified Biological Safety Level II laboratory.

4.2.5 Surface Functionalization

For pathogen detection application, the electrospun membrane was functionalized with the polyclonal antibody to act as capture pad of the biosensor, as illustrated in Figure 4.9. To further enhance protein binding and reduce pH effect, glutaraldehyde ($C_5H_8O_2$) was used as a cross-

linking agent to attach antibodies to the electrospun nanofiber membrane. The concentration and quantity were determined to be 20 μL of 0.1% glutaraldehyde solution per 1.0 in^2 of nanofibrous membrane. Less glutaraldehyde (10 μL and 15 μL) led to inadequate antibody binding to the member, which was verified by the confocal laser scanning microscopy imaging described in Section 4.3.1. First, glutaraldehyde solution was evenly dispensed on the membrane, and then allowed to dry in a biosafety cabinet for 10 minutes. After soaking with a phosphate buffer solution (PBS) buffer to remove excess solution, 0.5 mg/ml polyclonal antibodies (affinity purified goat anti-*E. coli* O157:H7 polyclonal antibodies or purified swine anti-BVDV polyclonal antibodies) were dispensed on the electrospun membrane with a concentration of 10 $\mu\text{g}/\text{in}^2$, and incubated at 25 °C for 30 minutes. The process was completed after a washing step using tris buffer with 0.1% tween-20 to remove excess chemical and block unbound antibody. The tween-20, or polysorbate 20, is a polysorbate-type nonionic surfactant formed by the ethoxylation of sorbitan, which is used to saturate binding sites on surfaces. The immuno-functionalized nanofiber membrane was stored at 4°C in a refrigerator until needed (up to about 1 week).

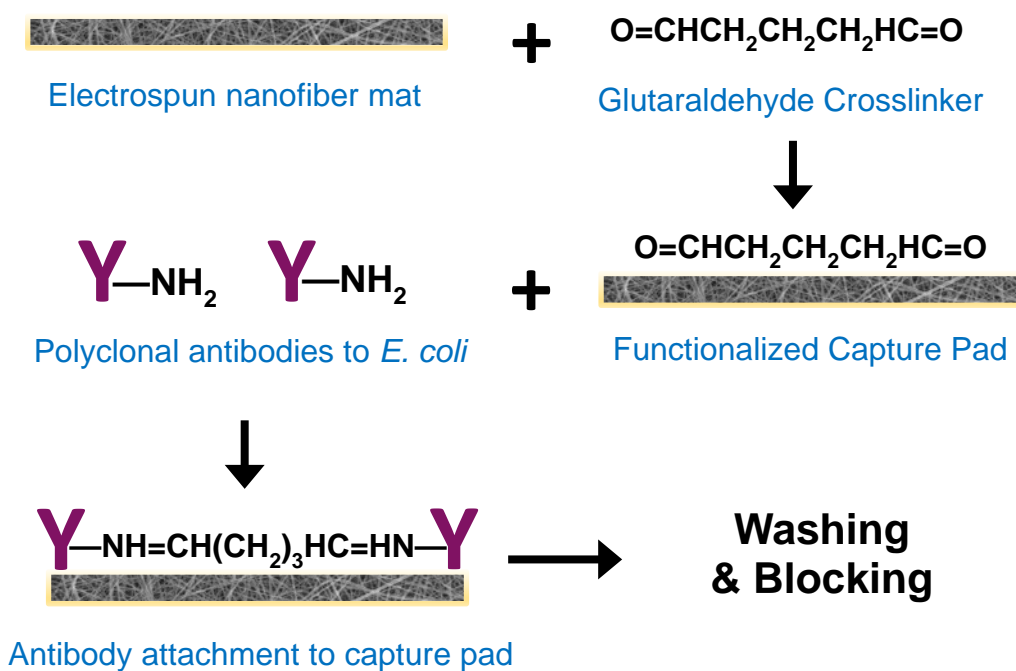


Figure 4.9. The surface antibody functionalization process for the electrospun biosensor capture pad.

The antibody attachment protocol was verified using fluorescein isothiocyanate (FITC) labeled antibody and confocal laser scanning microscopy (CLSM) to measure the amount of emission of fluorescent antibody. The significant emission at 530 nm optical wavelength confirmed an efficient antibody attachment on the electrospun membrane. Besides, CLSM images also demonstrated that the novel nanostructure by the electrospinning method was retained after immuno-surface functionalization.

4.2.6 Immunomagnetic Separation

The conductive magnetic nanoparticles were synthesized from aniline monomer and gamma iron (III) oxide ($\gamma\text{-Fe}_2\text{O}_3$) nanoparticles using a sol-gel chemical solution deposition method [82]. The

polymerized MNPs' polyaniline (PANI) shell was transformed to be electrically conductive by acid doping.

For *E. coli* antibody functionalization, 2.5 mg of the conductive PANI magnetic nanoparticles were dispensed to 150 μL of 0.1M PBS, and sonicated for 10 minutes for uniform dissolution. 100 μL of affinity purified mouse anti-*E. coli* O157:H7 monoclonal antibody (2.5 mg/mL) was added to the solution for conjugation, according to the tuning process developed in our lab [115]. For BVDV antibody functionalization, 100 μg of the conductive PANI magnetic nanoparticles dispensed in 1 mL PBS were sonicated for 10 minutes, and 100 μL of 0.15 mg/mL affinity purified mouse anti-BVDV 15c5 (gp48) in PBS was added. The mixture solution was then incubated at 25 $^{\circ}\text{C}$ in a hybridization oven rotating at 30 rpm for 1 hour. As a result, the antibody, which is negatively charged, was conjugated with the positively-charged PANI shell of the nanoparticles by electrostatic force [81].

After incubation, the antibody functionalized magnetic nanoparticles (AFMNs) were cleaned by magnetic separation to remove impurities. The magnetic separation wash was performed three times with a blocking buffer consisting of 100 mM Tris-HCl buffer (pH 7.6) and 0.1% (w/v) casein (Figure 4.10). After the final wash step, the antibody functionalized magnetic nanoparticles were re-suspended in 2.5 mL 0.1M PBS and stored in a 4 $^{\circ}\text{C}$ refrigerator until needed.

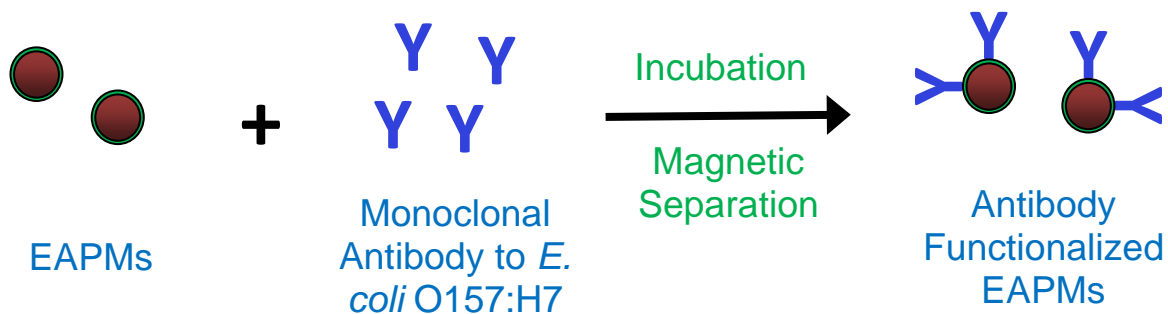


Figure 4.10. The antibody functionalization process for the conductive MNPs.

For immunomagnetic separation, the AFMNs were vortex mixed and placed in a magnetic separator for 2 minutes. The supernatant was discarded using a micropipette. Then 1 mL of pathogen sample solution obtained by serial dilution was added and incubated at 25 °C in a hybridization oven rotating at 30 rpm for 30 minutes. After three magnetic separation rinses (by adding 1 mL of tris buffer solution with 0.1% casein and removing the supernatant), the AFMNs which captured the target pathogen were finally re-suspended in 1 mL of PBS. As a result, the test sample solutions with different concentrations were purified by magnetic separation and labeled with electrical conductance, and ready for biosensor detection.

4.2.7 Detection and Data Analysis

The biosensor testing unit consisted of a plastic printed circuit board (PCB) base and imprinted parallel copper electrodes pair, which was connected to the input of a data acquisition system as shown in Figure 4.11 below. The parallel copper electrodes were 25 mm apart to mount the electrospun MNP biosensor in between. A pair of secondary copper electrodes, which appear as

flaps on the base electrodes, in Figure 4.11 (a), was placed over the silver electrodes of the biosensor's capture pad to form a low resistance sandwich structure. This ensured an excellent electrical contact to the capture pad to directly measure conductance of the conjugated MNPs in nanofiber membrane. The biosensor testing unit was designed to include multiple measurement units, in Figure 4.11 (b), to simultaneously measure three electrospun MNP biosensors.

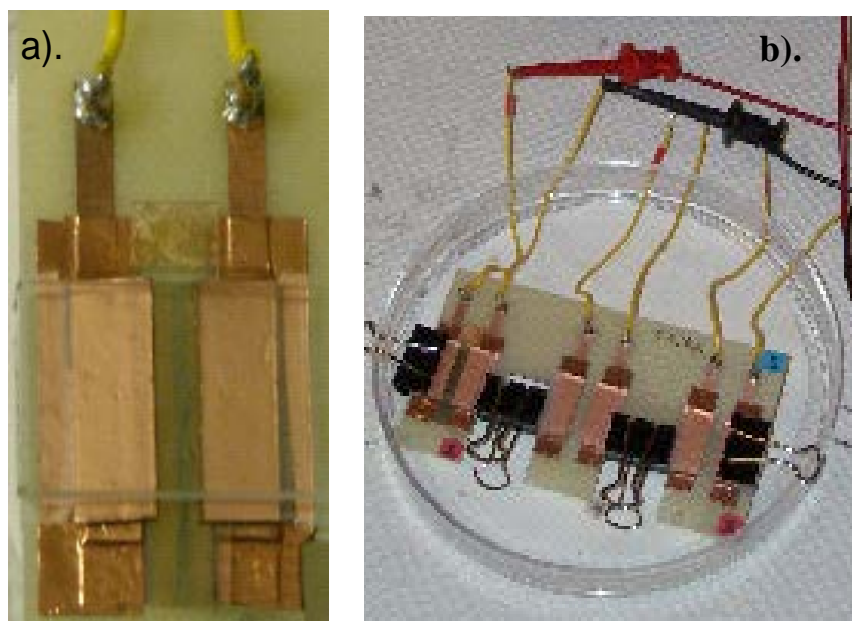


Figure 4.11 Testing platform of electrospun MNP biosensor. (a) Test strip mounted on platform and sandwiched by copper electrodes. (b) Design of the entire platform with three testing units

For signal measurement, the biosensor strips were connected via the testing unit to a data acquisition (DAQ) system, NI USB-6221 (National Instrument, Austin, TX). The DAQ system was linked to a computer with USB interface and controlled by graphical user interface software in LabVIEW (National Instrument, Austin, TX). For each sample, after immunomagnetic separation, a volume of 100 μL (*E. coli* O157:H7) of the test sample solution (200 μL for BVDV) was applied to the application pad of the biosensor and the conductance signal across the silver

electrodes was measured by the DAQ system. When capillary flow equilibrium was achieved at around 8 min, the biosensor resistance across the silver electrodes was recorded by the DAQ system to determine target concentration. The sample lateral flow time from the application membrane to the capture membrane was approximately 1 min. Conductance data was recorded 30 sec before test sample application and continued through 8 min until capillary flow equilibrium can be achieved. For data analysis, a minimum of three replications were performed for each experiment. All biosensors were calibrated using a control sample which consisted of the same AFMNs suspended in sterile DI water except pathogen. Standard deviations and mean values for the data of each experiment were calculated. Statistical analysis was performed based on a single factor analysis of variance using SAS ANOVA.

4.3 Results and Discussion

4.3.1 Surface Functionalization with Antibody

The effect of immuno surface functionalization was verified using the confocal laser scanning microscopy (CLSM) method. The fluorescein isothiocyanate (FITC) labeled antibody (530 nm and 435 nm) was functionalized on the electrospun nanofibrous membrane using the same immuno-functionalization process described in Chapter 4.2.5 above. After two additional washing process using tris buffer with 0.1% tween-20 to remove unbound antibody, CLSM was used to image the functionalized membrane, and measure its laser excited fluorescence wavelength to confirm antibody attachment. As shown in Figure 4.12 A and Figure 4.13 A, significant fluorescent emission at 530 nm (green) and 435 nm (red) were observed, respectively, which confirmed a strong antibody attachment to the electrospun membrane. The untreated nanofibrous membrane was also analyzed to compensate background noise generated by the substrate and

fibers (Figure 4.12 B and Figure 4.13 B). In addition, the CLSM image (Figure 4.12 A and Figure 4.13 A) and SEM image (Figure 4.14 A) also demonstrated that the unique nanostructure of electrospun membrane was retained after the bio-modification process, which is critical for biosensing performance.

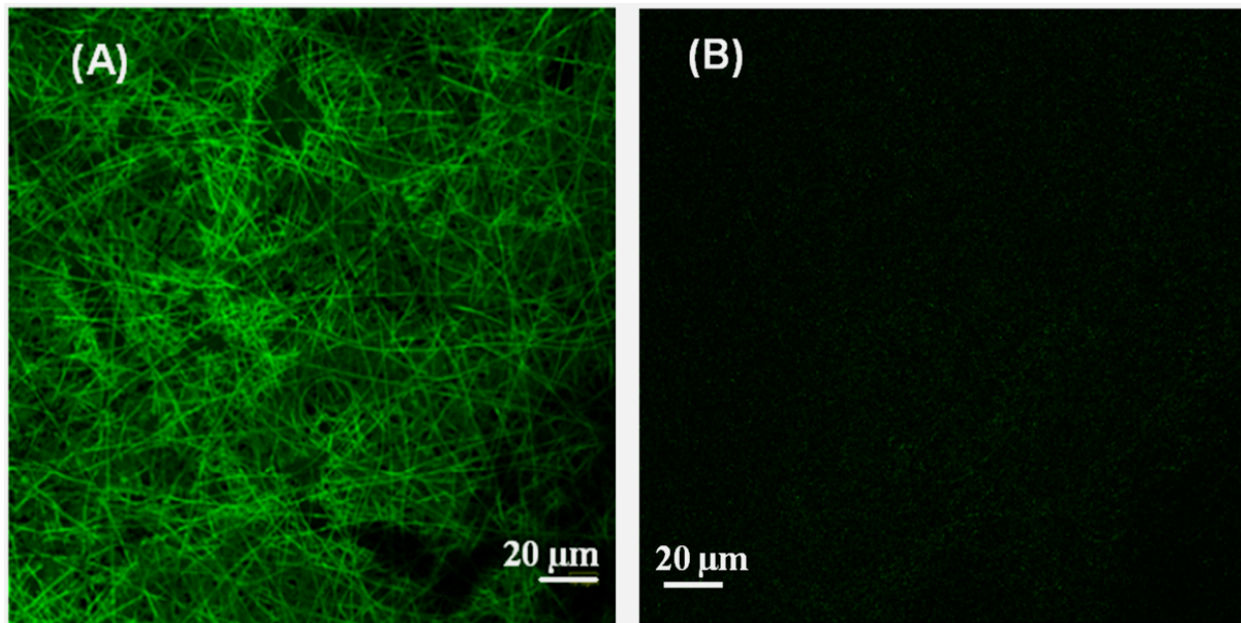


Figure 4.12 The CLSM image of functionalized membrane with FITC antibody, (A) CLSM image of nitrocellulose nanofibrous membrane with FITC antibody functionalization, (B) CLSM image of nitrocellulose nanofibrous membrane without antibody. Significant fluorescence emission at 530 nm verifies the antibody immobilization.

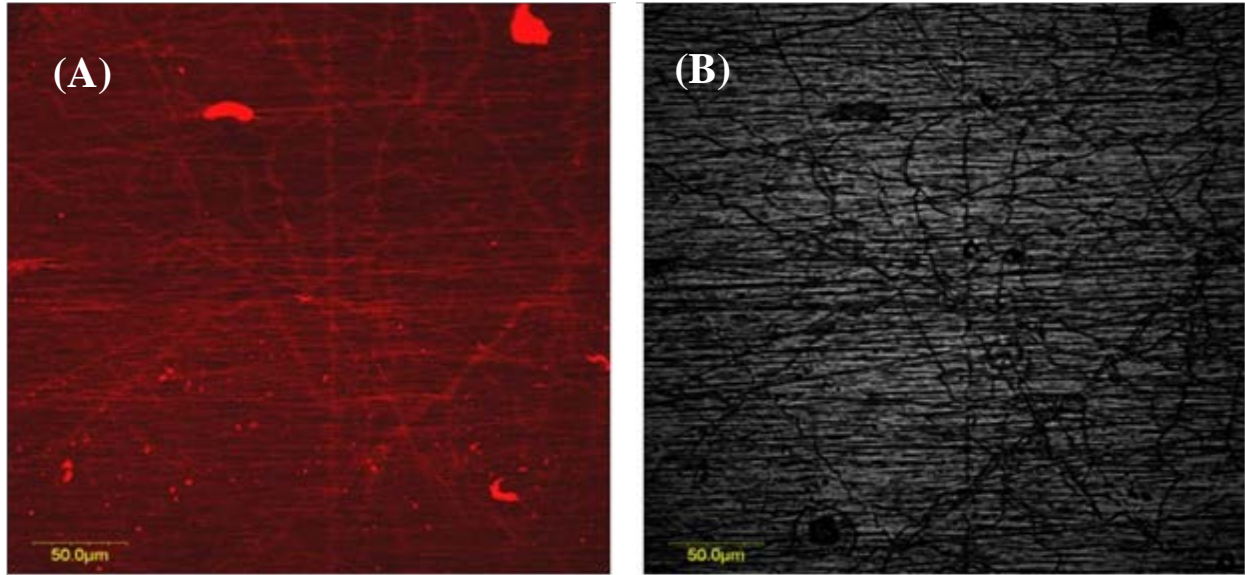


Figure 4.13 FITC antibody functionalized electrospun membrane: (A) CLSM image verified that the fiber morphology retains after antibody functionalization. (B) Fluorescence image confirmed that antibodies are attached on membrane after wash step by significant fluorescent emission at 435 nm.

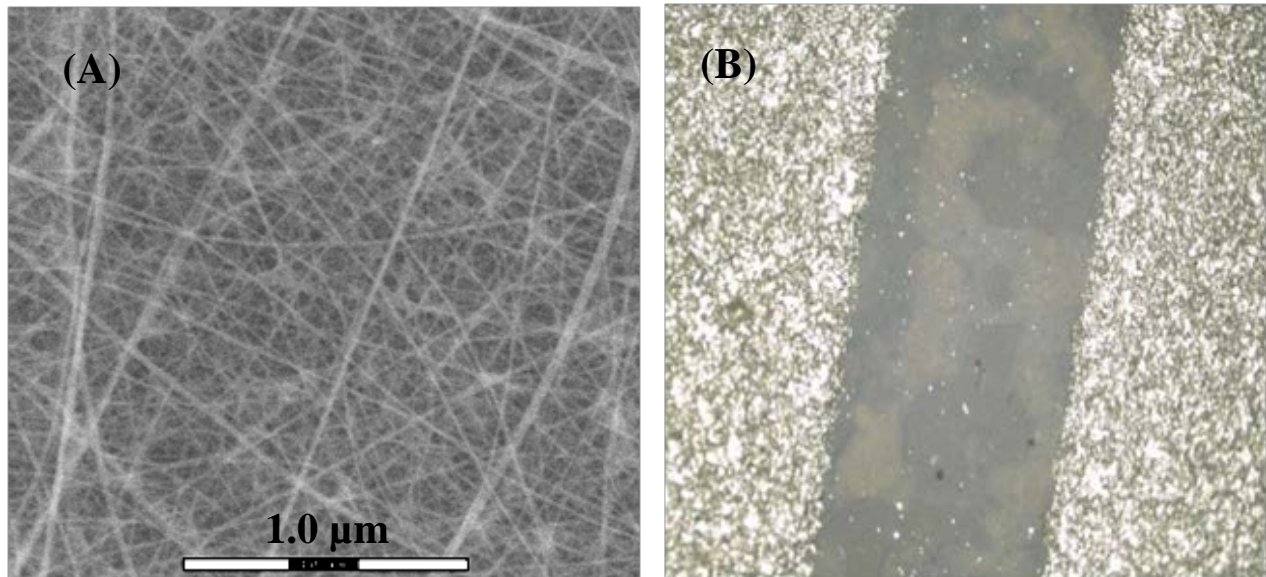


Figure 4.14 The SEM and optical microscope image of functionalized membrane with FITC antibody (A) SEM image of the electrospun nanofibrous membrane, (B) optical microscope image of nanofibrous membrane and silver electrodes after antibody functionalization.

4.3.2 Aligned Nanofibrous Membrane by Parallel Electrode Electrospinning

A special collector made of parallel electrodes was implemented in the NEU unit in order to create a membrane of highly aligned nanofibers [111]. In the vicinity of the parallel electrodes, the electrical field line direction was split symmetrically into two trends pointing towards edges of the gap along the electrodes. The spun polymer jet followed the electrical field force, which stretched the synthesized nanofibers as being across the electrodes and orthogonal to the gap direction. The spinning process created a reproducible ultra-fine and highly aligned nanofibrous membrane, which was confirmed by SEM image (Figure 4.15).

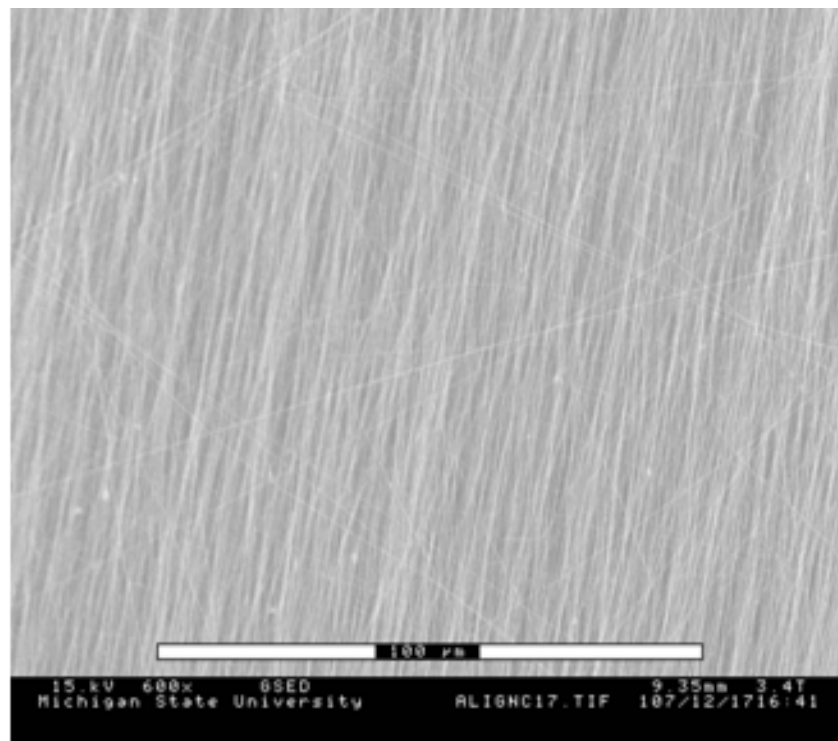


Figure 4.15 SEM image of highly-aligned nanofibrous membrane synthesized by the parallel electrode collector electrospinning.

A significant fluorescent emission was observed in the CLSM image at 600× magnification, which verified strong antibody functionalization. Besides, the highly aligned fiber morphology remained intact after the functionalization process, which is shown in Figure 4.16.

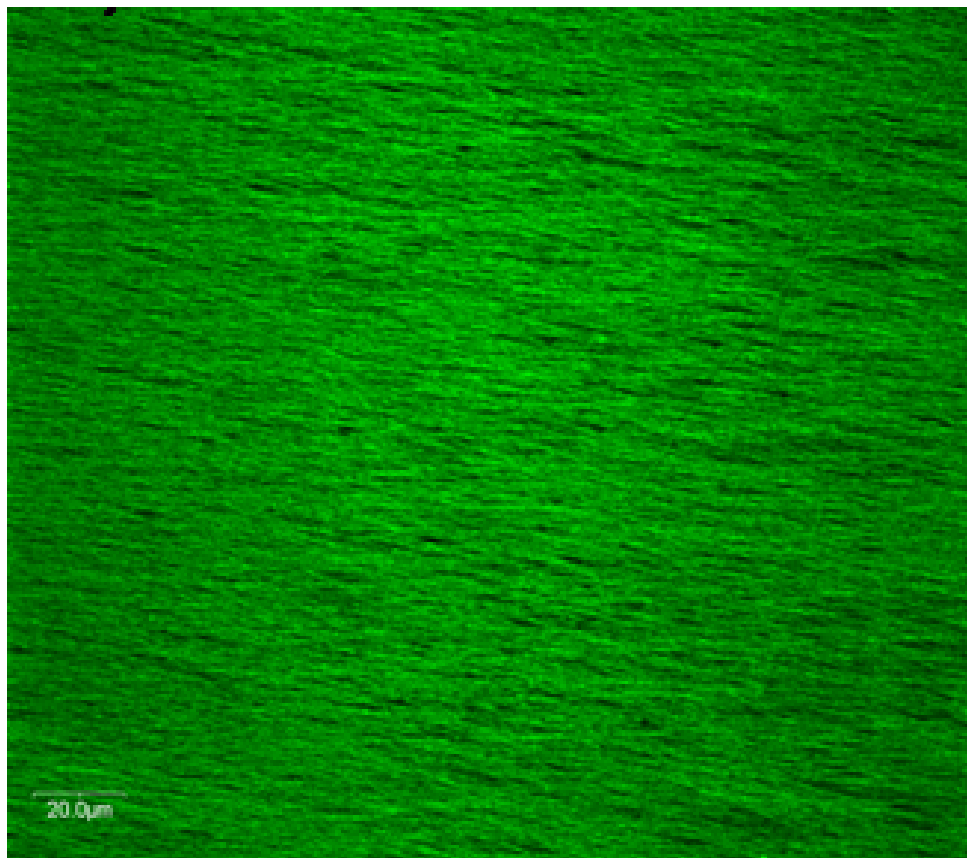


Figure 4.16 The CLSM image at 600×: significant fluorescent emission verified strong antibody functionalization, and the highly-aligned fiber morphology still remained intact.

4.3.3 Biosensor Detection

The process parameters and sensing conditions were determined to fulfil the biochemical conditions for the lateral flow immunoassay. The performance of lateral flow immuno biosensors depends on the capillary action which determines the effect of pathogen capture and impurity separation. The solution pH affects protein solubility, which affects antibody attachment and pathogen conjugation. Tris buffer was applied to sustain a neutral environment (pH 7.0) in the

assay to facilitate antibody-antigen reaction and reduce background noise [82] [112][116]. Due to high surface area and low cross section of the MNPs and nanofibers, the electrospun MNP biosensor significantly improved the pathogen binding and impurity separation event. The applied antibodies for electrospun membranes was optimized to be $10 \mu\text{g}/\text{in}^2$, which is more cost effective compared to conventional nitrocellulose planar material which typically requires 50 to $500 \mu\text{g}/\text{in}^2$ following the same functionalization protocol.

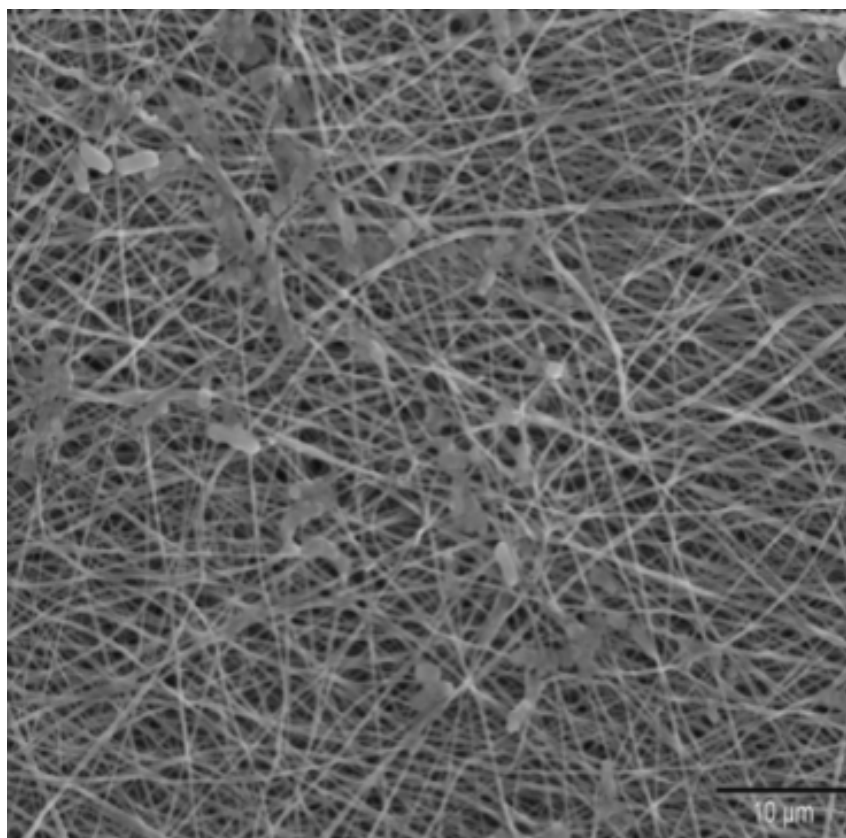


Figure 4.17 SEM images of electrospun membrane after test. *E. coli* O157:H7 were effectively captured on the functionalized fiber mat.

The pathogen capture by the immuno functionalized electrospun nanofibrous membrane was confirmed using SEM imaging. The lateral flow test using *E. coli* O157:H7 sample were conducted on the electrospun membranes with and without the immuno functionalization, respectively. After

flow equilibrium, the membranes were both washed and then dried for imaging. Figure 4.17 above demonstrated that the target pathogen can be effectively immobilized on the immuno-functionalized membrane. Nonspecific materials were not observed in the image. Furthermore, the specificity was based on affinity information of the purified and target-specific antibodies as provided by the manufacturer.

On the other hand, the untreated membrane failed to capture any organism (Figure 4.18). Furthermore, the SEM images verified that the unique nano structure of the nanofibrous membrane was retained after surface functionalization and capillary flow action.

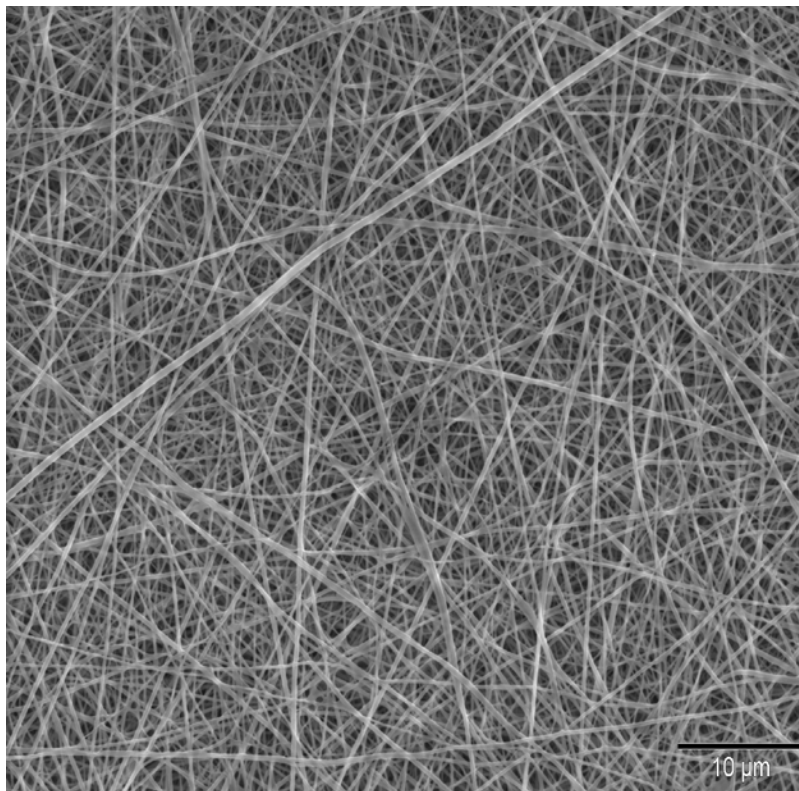


Figure 4.18 SEM images of electrospun membrane after test. No bacteria were observed in the nanofiber mat without functionalization.

The sensitivity and performance of the electrospun biosensor was verified by experiments using *E. coli* O157:H7 and BVDV of different concentrations, respectively. The real-time conductance signal of the electrospun MNP biosensor for samples of different *E. coli* O157:H7 concentrations are demonstrated in Figure 4.19 below. During the initial time around 50 sec after sample dispensing, the conductance signal increased with fluctuations as the antigen conductive MNP complex flowed to and along the capture pad. During the capillary action, the immunoreactions tethered the conductive MNPs in the nanofibrous membrane to form conducting bridges between the silver electrodes. After the flow reaches the absorption pad, the sensor conductance gradually decreased as the excess reagent were separated and absorbed by the capillary flow. When absorption achieved equilibrium after 8 min, the conductance signal became stable and was suitable for sensor reading for approximately 6 min. Afterwards the sensor conductance signal started to decrease rapidly due to drying effect, which caused reduction in the conductivity of polyaniline and antibody-antigen bonding [118]. As shown in Figure 4.19 below, the biosensor conductance signals of different test samples increased in proportion to the target concentration, and were all larger than that of the control sample. This result confirmed that a test sample with higher target concentration was able to create more electrical conducting bridges by the conductive MNP sandwich complex, which led to increase in biosensor conductance signal. The signals were differentiable at approximately 100 sec. We acquired the results at 10 min until the signals became stable (with small variations when the flows approaching equilibrium).

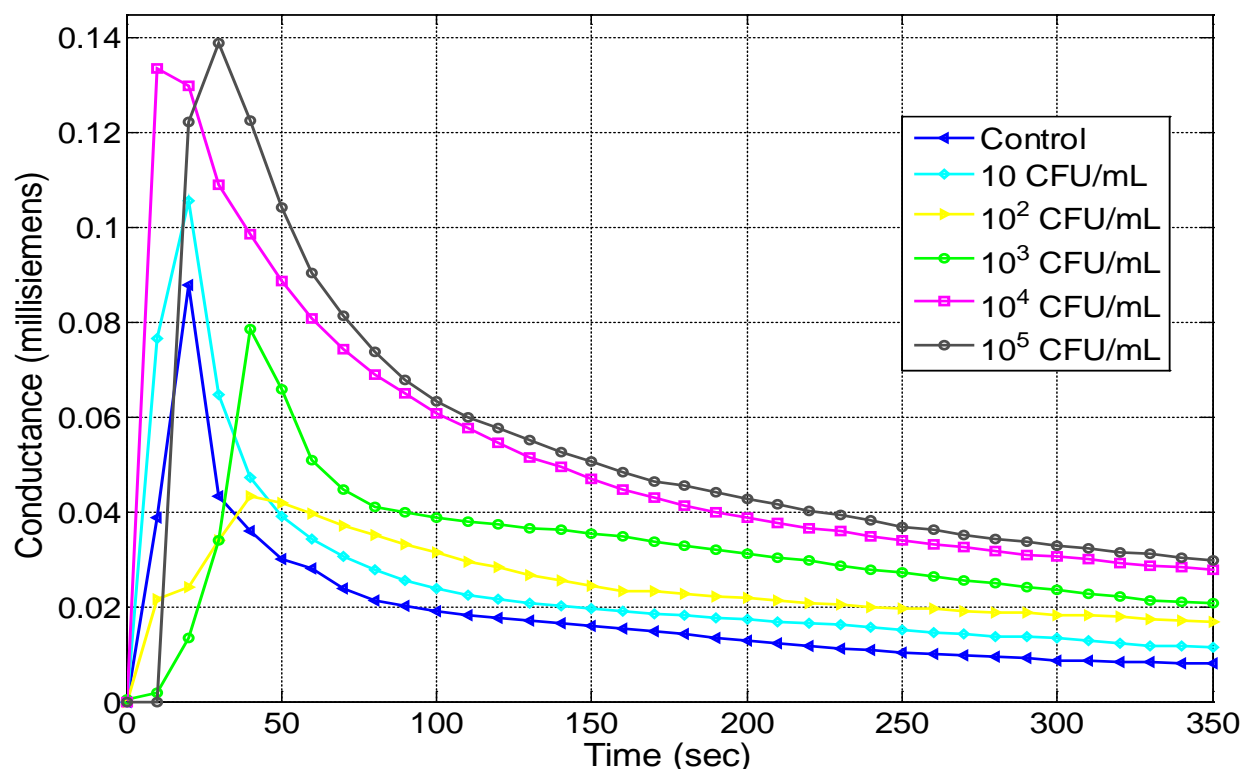


Figure 4.19 Biosensor conductance signal versus test time of *E. coli* O157:H7 samples with different target concentrations: aligned nanofibrous biosensor

The pathogen detection results of the biosensor using unaligned nanofibrous membrane are illustrated in Figure 4.20. The biosensor demonstrated linear sensing response for test samples with different *E. coli* O157:H7 concentrations from 0 to 10⁴ CFU/mL (Figure 4.21). Its sensitivity (detection limit) was measured to be 61 CFU/mL ($P < 0.05$, $n = 3$). It could detect a contamination from a 1 mL sample without the optional magnetic concentration, since the infectious dose is thought to be less than 100 cells [119]. The detection limit is comparable with or better than other lateral flow biosensors reported in the recent literature (ranging from 10¹ CFU/mL to 10⁴ CFU/mL) [120]-[122]. Unpaired t-tests were used for two group comparisons and the associated P-values were summarized in Table 4.2.

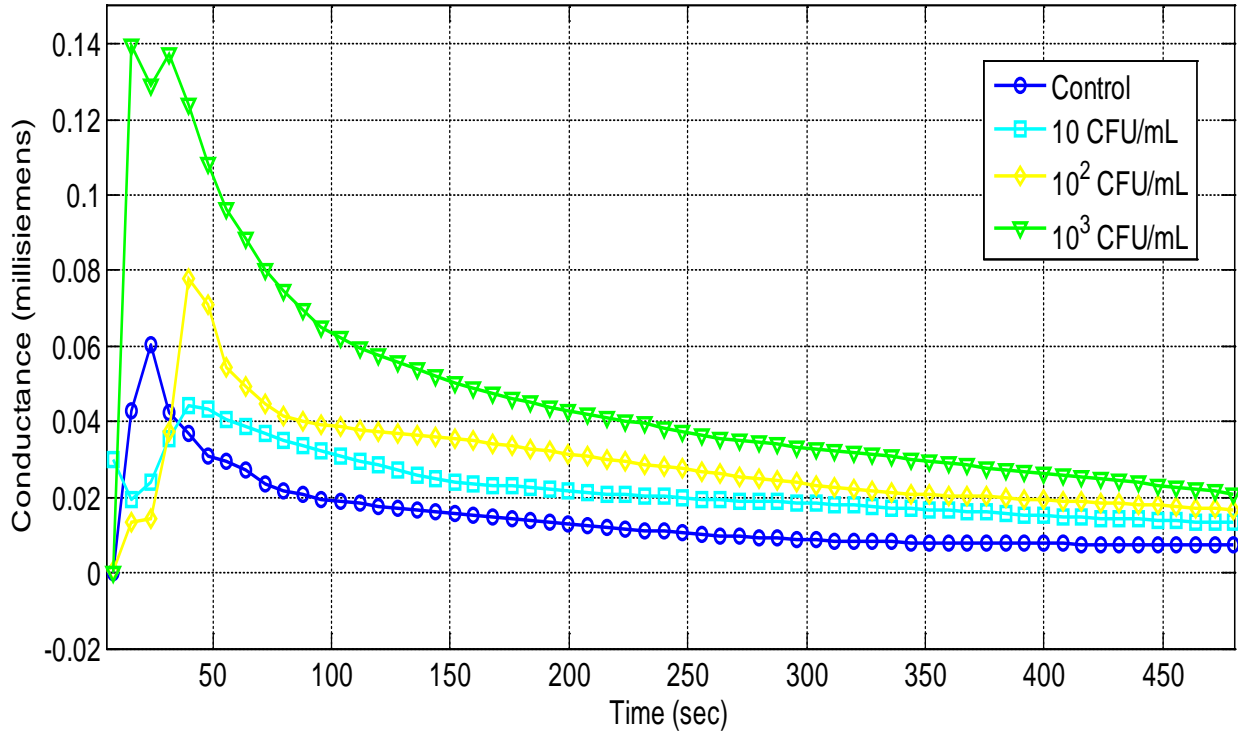


Figure 4.20 Biosensor (unaligned nanofibers) conductance signal versus test time of *E. coli* O157:H7 samples with different target concentrations: randomly oriented nanofibrous biosensor

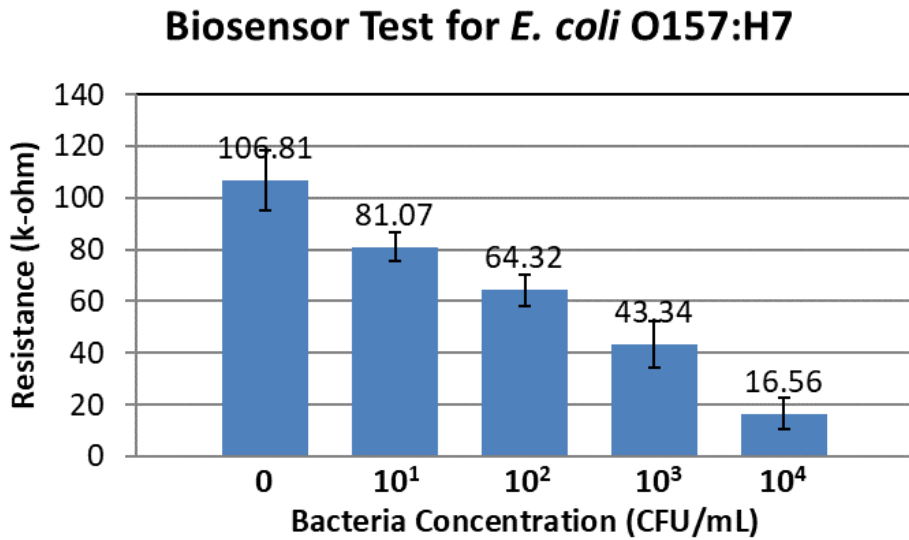


Figure 4.21 Biosensor test results (unaligned nanofiber) for *E. coli* O157:H7 demonstrate a linear sensing response from 0 to 10⁴ CFU/mL.

Table 4.2 P-value of biosensor test results (unaligned nanofiber) for *E. coli* O157:H7

Sample Pair (CFU/mL)	P-value (n = 3)
0 (control) vs 10^1	0.041
10^1 vs 10^2	0.025
10^2 vs 10^3	0.031
10^3 vs 10^4	0.023

The biosensor was also tested for potential application of virus detection. The results of BVDV test sample measurements are illustrated in Figure 4.22. The associated P-values were calculated and summarized in Table 4.3. The biosensor also exhibited linear response to different BVDV concentrations. The estimated viral concentration before dilution was 10^6 CCID/mL. The lowest detectable sample was 10^3 dilution ($P < 0.05$, $n = 3$), which had virus concentration of approximately 10^3 CCID/mL and was equivalent to 1/1000 viral concentration in the blood serum of infected bovine [117].

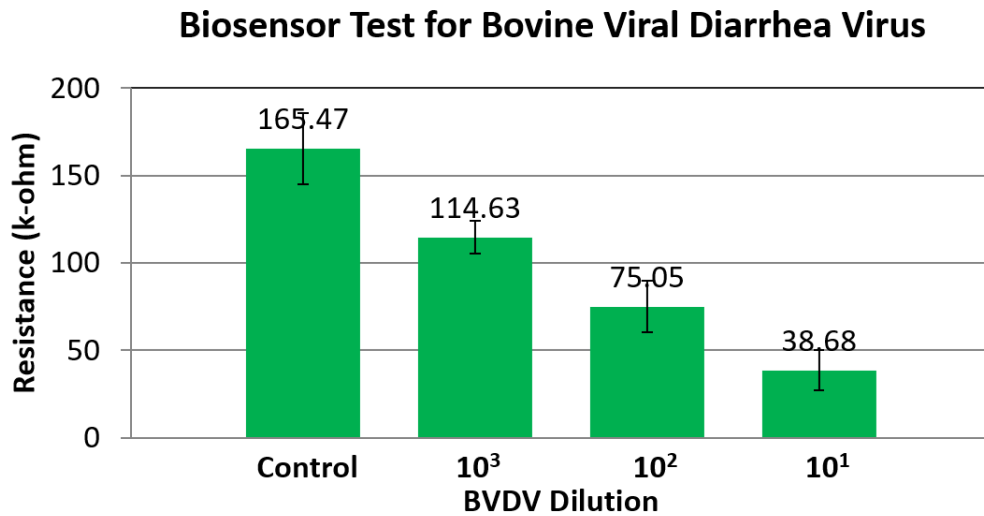


Figure 4.22 Biosensor test results (unaligned nanofibrous mat) for BVDV virus demonstrate the linear sensor response from 10^1 to 10^3 virus dilution and control sample.

Table 4.3 P-value of biosensor test results (unaligned nanofiber) for BVDV

Sample Pair (dilution)	P-value (n = 3)
Control vs 10 ³	0.003
10 ³ vs 10 ²	0.027
10 ² vs 10 ¹	0.029

The MNP biosensor was further improved by using aligned electrospun nanofibrous membrane, which was described in Chapter 4.2.1. The test results for test samples of different *E. coli* O157:H7 concentrations are demonstrated in Figure 4.23 below. The associated P-values were calculated and summarized in Table 4.4. The aligned nanofiber biosensor exhibited a linear response in electrical resistance signal for *E. coli* O157:H7 concentrations from 10¹ up to 10⁴ CFU/mL. The baseline signal appeared to be increasing owing to the aligned nanofibers. However, no improvement in sensitivity was observed. The next level, 10⁰ CFU/mL, was of extremely low concentration, which was difficult to detect due to variability in biochemical events and environmental noise. For concentrations at and above 10⁵ CFU/ml, the measured resistance of the biosensor became non dose-responsive. However, the signals of 10⁵ to 10⁷ CFU/mL samples showed resistance that were still significantly below the control sample (0 CFU/mL) ($P < 0.05$, $n = 3$). This sensor behavior was due to the over-crowding effect due to the nature of sandwich immunoassays [123]. Above certain high concentrations, the binding site of the capture membrane was saturated by the excess amount of antigen, which kept the resistance signal from decreasing [124].

Biosensor Test for *E. coli* O157:H7

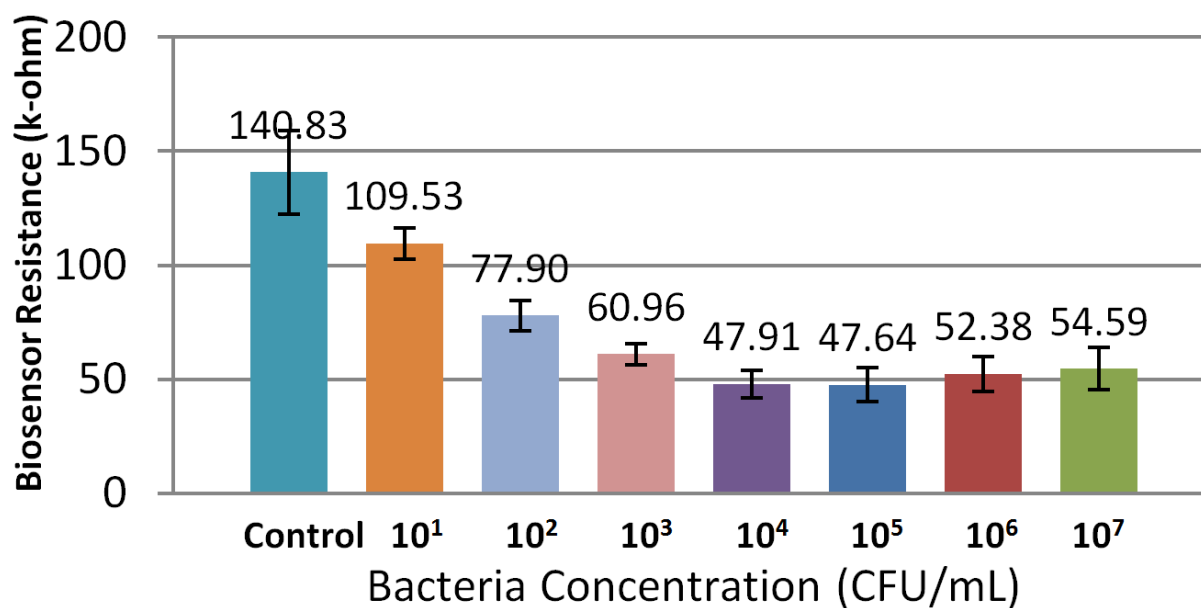


Figure 4.23 Biosensor test results (aligned nanofibers) for *E. coli* O157:H7 demonstrated a linear relationship between resistance signal and bacterial concentration from 10¹ to 10⁴ CFU/mL. The signal was significantly below the control from 10⁵ to 10⁷ CFU/mL.

Table 4.4 P-value of biosensor test results (aligned nanofiber) for *E. coli* O157:H7

Sample Pair (CFU/mL)	P-value (n = 3)
0 (control) vs 10 ¹	0.015
10 ¹ vs 10 ²	0.004
10 ² vs 10 ³	0.021
10 ³ vs 10 ⁴	0.040
10 ⁴ vs. 10 ⁵	0.963
10 ⁵ vs. 10 ⁶	0.484
10 ⁶ vs. 10 ⁷	0.766

The MNP biosensor fabricated using electrospun membranes with/without fiber alignment both exhibited higher sensitivity and wider linear response for microbial pathogen detection than that of conventional mesoporous membrane. To compare detection performance, biosensors using nitrocellulose porous membrane (Millipore, MA, USA) were fabricated following the same functionalization and sensor assembly process. Under the same testing, the electrospun biosensor remained linearly responsive from 10^1 to 10^4 CFU/mL, whereas nitrocellulose biosensor's linear range was from 10^1 to 10^2 CFU/mL, as shown in Figure 4.24 below. The detection limit of the nitrocellulose biosensor was 10^2 CFU/mL ($P < 0.05$, $n = 3$). The associated P-values for nitrocellulose biosensor test results were calculated and summarized in Table 4.5. Due to the unique nano porous structure and high surface area, the electrospun capture membrane provided more binding site and capillary flow action, which enhanced the immuno reaction and excess material separation. Compared to conventional mesoporous membranes, the contact area between the active mass transfer region of the nanofibrous membrane and the underlying substrate was greatly reduced. This substantially decreased electrical background noise in the direct charge measurement, which was caused by electronic charge interactions through different material interface. Hence, the electrospun biosensor was able to detect not only the presence of lower target pathogen concentration, but also provide linear detection response.

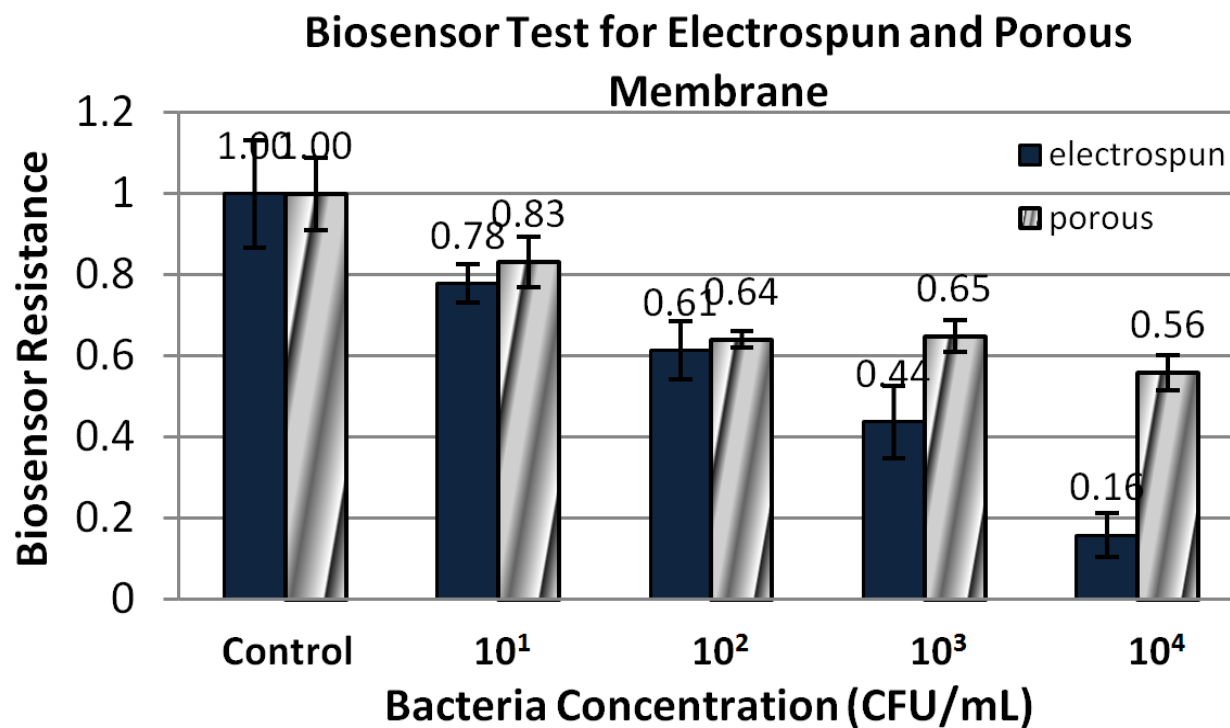


Figure 4.24 Pathogen detection comparison of biosensors made of electrospun nanofibrous membrane and nitrocellulose mesoporous membrane.

Table 4.5 P-value of biosensor test results (nitrocellulose mat) for *E. coli* O157:H7

Sample Pair (CFU/mL)	P-value (n = 3)
0 (control) vs 10 ¹	0.057
10 ¹ vs 10 ²	0.038
10 ² vs 10 ³	0.765
10 ³ vs 10 ⁴	0.023

4.4 Conclusions

In this chapter, the immuno-functionalization of PANI magnetic nanoparticles for biosensor application was successfully accomplished. The reaction solution and temperature were optimized for antibody functionalization affinity. The assay conditions were determined to be 0.25 mg of affinity purified mouse anti-*E. coli* O157:H7 monoclonal antibody for 2.5 mg PANI MNPs in a total volume of 250 μ L PBS solution [115]. The immuno PANI MNPs were successfully implemented for magnetic separation for impurity removal and sample concentration.

To fully investigate *E. coli* O157:H7 detection, the PANI MNP based immunoassay was successfully integrated into an electrospun lateral flow biosensor system. Due to the unique nanostructure and biocompatibility of PANI MNPs, the biosensor had linear detection response of *E. coli* O157:H7 sample concentration from 10^1 to 10^4 CFU/mL and exhibited a detection limit of 61 CFU/mL. The application of the biosensor can be extended to other microbial or viral organisms by appropriately changing the antibodies. Due to the unique property of the magnetic nanoparticles, this simple measurement system makes applications possible for low cost detection and rapid on field testing.

The MNP based electrospun lateral flow biosensor demonstrated excellent detection performance and rapid response compared to other conventional *E. coli* detection methods. The total detection time required 15 min, which includes 5 min of magnetic separation and 10 min of lateral flow process (until the flows are stable) and data acquisition.

To further improve detection time, a new type of advanced biosensor was designed based on NMR and MNPs in our lab. Its development, optimization and experimental testing are summarized in Chapter 5.

This chapter is adapted from our recently published work in the journals of Biosensors and Bioelectronics, and IEEE Transactions on Nanotechnology:

Yilun Luo, Steven Nartker, Hanna Miller, David Hochhalter, Michael Wiederoder, Sara Wiederoder, Emma Settingington, Lawrence T. Drzal, Evangelyn C. Alocilja. Surface functionalization of electrospun nanofibers for detecting *E. coli* O157:H7 and BVDV cells in a direct-charge transfer biosensor. *Biosensors and Bioelectronics*. 2010. 26(4):1612-1617.

DOI: 10.1016/j.bios.2010.08.028

Yilun Luo, Steven Nartker, Michael Wiederoder, Hanna Miller, David Hochhalter, Lawrence T. Drzal, Evangelyn C. Alocilja. Novel Biosensor Based on Electrospun Nanofiber and Magnetic Nanoparticles for the Detection of *E. coli* O157:H7. *IEEE Transactions on Nanotech*. 2011. 11(4): 676 – 681.

DOI: 10.1109/TNANO.2011.2174801

CHAPTER 5

BIOSENSOR BASED ON NMR AND MAGNETIC NANOPARTICLES FOR PATHOGEN DETECTION

5.1 Introduction

The Nuclear Magnetic Resonance (NMR) is a versatile scientific instrument to analyze the nuclear magnetic properties of atomic nuclei and determine chemical properties of biomolecules. As its signal is powerful to penetrate turbid raw samples, NMR instruments have wide applications in non-destructive biomedical diagnosis, which can simplify sample preparation process, and save analysis time [125]. However, the commercial NMR systems are expensive, bulky and heavy (around 1,000 kg), which limit their application for portable pathogen detection [126]. A portable NMR system was developed using integrated circuit technique [133]. It was designed to detect avidin and cancer cells by measuring the test sample's NMR relaxation, which was proportional to the immunological clustering of magnetic nanoparticles [134] [140]. The fabrication for integrated circuit is high in cost. And besides integrated circuits, it still required additional systems, such as signal generator, filters, and data acquisition system, which considerably increase the system cost and size. Their sensitivity for cancer cell detection was in the range of 1000 CFU/mL.

The detection of *E. coli* O157:H7 is time consuming and requires complex instruments and extensive training. The Sorbitol-MacConkey (SMAC) agar method is used for identification but takes about 2 to 4 days, including culture, morphological identification, and confirmation techniques [145][146]. The polymerase chain reaction (PCR) based detection assays are sensitive and accurate [147]. However, the PCR techniques require complex sample preparation steps, such

as DNA extraction and amplification, which increase additional diagnosis time. Fast detection methods have been reported based on immunological detection. However, most of these diagnosis systems have sensitivity limit greater than 100 CFU/mL, detection time of 1 hour, and are not applicable for in-field applications [148][149]. To minimize the spread of infection and costly product recall, a rapid, sensitive, and portable detection of *E. coli* O157:H7 is essential in food supply and healthcare applications. This chapter reports a new design of portable NMR system including NMR probe and transceiver for a biosensor to detect *Escherichia coli* O157:H7 using the magnetic nanoparticles as biomarker. The system is low in cost and small in size, and it is thus suitable for portable pathogen detections.

5.2 Materials and Methods

5.2.1 Design of Portable NMR Biosensor

A complete NMR system was designed consisting of proton NMR probe, high power and high sensitivity transmitter and receiver, field-programmable gate array (FPGA) based pulse controller, and communication interface. The system utilized an ultra-strong permanent magnet, PM-1055, by Metrolab Instruments Inc. (Geneva, Switzerland). Its magnetic field strength is 0.49 Tesla with field homogeneity of 10 ppm. It has a compact size of 80 mm diameter and 55 mm height, and weighs 1250 g [150]. A gauss meter was used to calibrate the magnetic field strength and determined its most homogeneous region to place the test sample for NMR detection. A solenoid coil of 5 mm diameter and 5 mm length was fabricated in lab. A matching network using low-parasitic capacitor trimmers was designed to achieve impedance matching and high-quality factor, Q [151]. The signal to noise ratio (SNR) was optimized in the NMR design as described in the following sections.

The portable NMR system was designed and built in the Nano-Biosensors Lab. It consisted of an NMR transmitter, a transmit/receive (T/R) switch, an NMR probe, and an NMR receiver, which are illustrated in Figure 5.1. In the NMR transmitter, the FPGA controls a Direct Digital Synthesis (DDS) to generate a 19.918 MHz RF signal for NMR excitation and signal demodulation in the receiver. After noise removal by a low pass filter (LPF), the RF signal was amplified by a linear power amplifier to reach 20 W, capable of exciting water nuclei resonance spin inside the NMR probe. The input to the power amplifier was switched off to reduce its background electrical noise. The T/R switch was designed using high speed crossed diodes and quarter wavelength transmission lines to protect a low noise amplifier from high-power during excitation and block the electrical noise from the NMR transmitter during receiving.

In the NMR receiver, the weak NMR signal was amplified by a low noise amplifier, which has a high amplification gain and very low noise. It is able to detect signal in $0.1 \mu\text{V}$, which is reemitted from the excited nuclei spinning in resonance. After noise removal using band pass filters (BPFs), the NMR signal was demodulated using RF mixers and LPFs. Quadrature demodulation was implemented to obtain the direct and quadrature components of the NMR signal to enhance the signal. With excellent concurrent calculation capability and high integration, an embedded system was designed in the FPGA using a multilayer state machine to receive commands, display results via HyperTerminal graphical interface, control NMR transmitter gain and frequency, acquire data through an analog to digital converter (ADC), data processing, and provide precise control to generate versatile NMR pulse sequence.

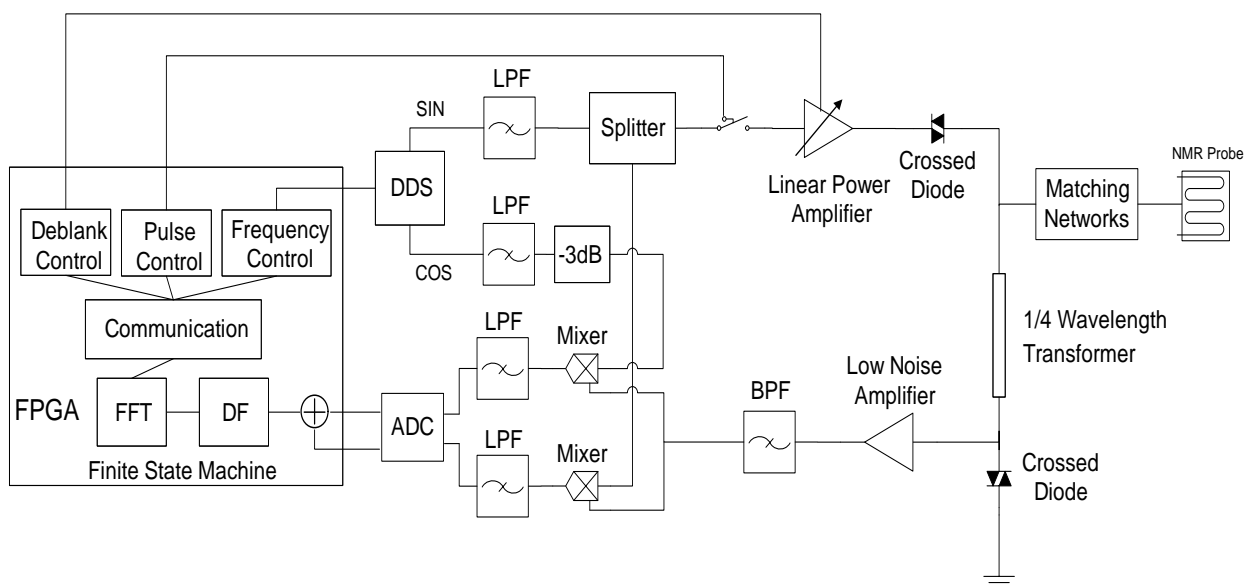


Figure 5.1 System Architecture of the Portable NMR, including FPGA control, modulation and demodulation system, and NMR sub-systems.

A prototype of the portable NMR system has been built as shown in Figure 5.2. The magnet holder, NMR probe holder, and gauss meter probe holder were designed using aluminum and wood, which does not interfere with the magnetic field. An X-Y-Z precision linear positioner was used to determine the most homogeneous region of the magnet, and adjust the NMR sample position, to optimize the NMR sensitivity. The prototype system was built using a low-cost amplifier, 50B power amplifier (Henry Radio), and AU-1467 linear amplifier (Miteq Inc.). The overall size of the prototype was 32 mm × 24 mm × 14mm. The system can be integrated in a mini personal computer enclosure, 20 mm × 18 mm × 8mm for better portability and electromagnetic compatibility (EMC) performance. A commercially available low-cost $\Phi 5$ mm NMR tube was used as test sample holder and is reusable by acetone washing. The sample volume of the prototype system was 100 μL . It could be further reduced by using thinner NMR tubes, such as a standard 20 μL NMR tube.

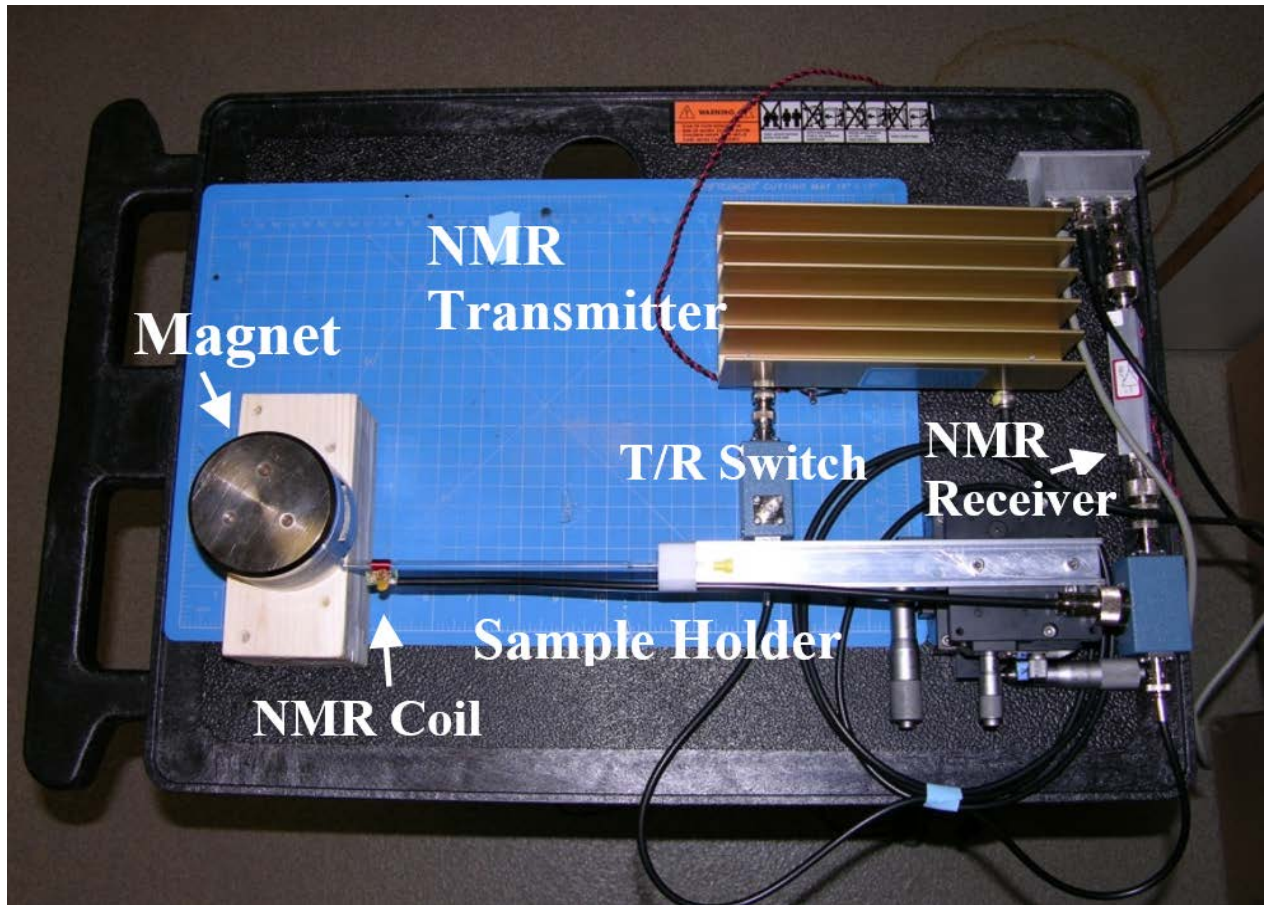


Figure 5.2 System prototype of the portable NMR, including a palm-sized permanent magnet, NMR transmitter, NMR receiver, T/R switch, sample holder, and NMR probe.

5.2.2 Design of Portable NMR Duplexer

The NMR duplexer is an RF switch in the NMR system, which automatically switch the NMR probe to connect with the power amplifier (PA) of the NMR transmitter or the low noise amplifier (LNA) of the NMR receiver. It was designed and built using a crossed diodes pair (1) in series with a quarter-wave impedance transformer followed by a second crossed diodes pair (2)

connecting to the ground, as shown in Figure 5.3. A second quarter-wave impedance transformer and crossed diodes pair (3) were added to improve the blocking of high-power signals.

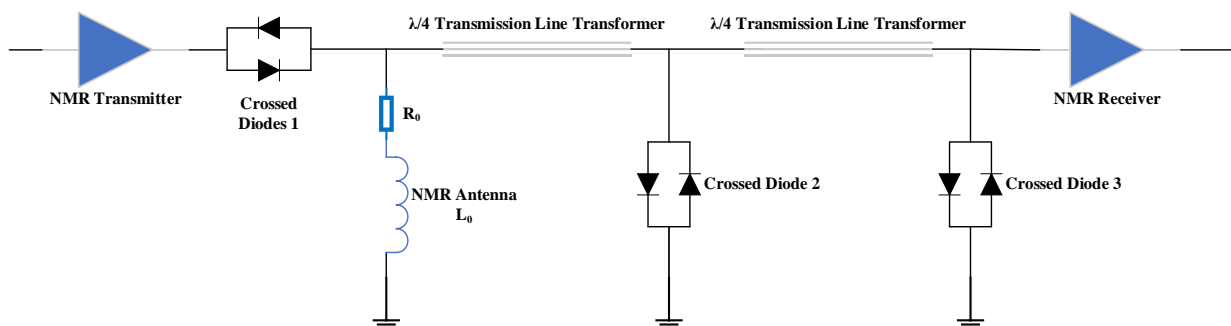


Figure 5.3 Complete set up of NMR coil antenna and duplexer switch for the NMR transmitter and receiver

During the NMR excitation process, the duplexer transmits the 20 W high-power RF signal from the power amplifier to the NMR probe while blocking that from the LNA to prevent any overrating damages. The antiparallel crossed diode pair operates as a high-frequency switch for RF signals. It is open for signals larger than the diode's built-in potential and is closed for small signals (Figure 5.4). The 20 W RF signal is greater than the built-in voltage of the diodes. The crossed diodes pair (1) is turned on as both of its diodes have been given an external forward bias.

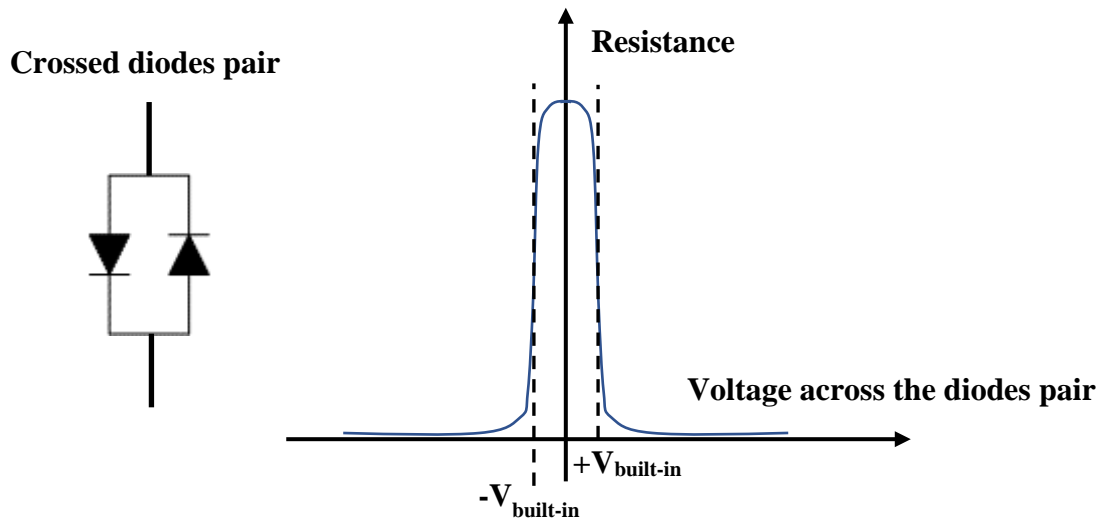


Figure 5.4 The crossed diodes pair shows high impedance for low voltages, and low impedance for high voltages. The threshold is the built-in voltage.

For the quarter-wave impedance transformer, the relationship between its input impedance, Z_{in} , and its load impedance, Z_{load} , is as defined in Equation 2.

$$Z_{in}Z_{load} = Z_0^2 \quad \text{Equation 2}$$

where Z_0 is the characteristic impedance of the transmission line, 50Ω . The high-power RF signal after the conducting crossed diodes pair (1) is sufficient to turn on the crossed diodes pair (2), which makes Z_{load} equal to the forward resistance of the diode (close to 0Ω). This makes Z_{in} become very high as $Z_{in} = Z_0^2/Z_{load}$. The more sets of quarter-wave impedance transformer and crossed diodes pair are added, the higher the impedance at the input port. As a result, the NMR duplexer circuit makes the NMR probe being closed-circuit to the NMR transmitter and disconnected from the NMR receiver (Figure 5.5).

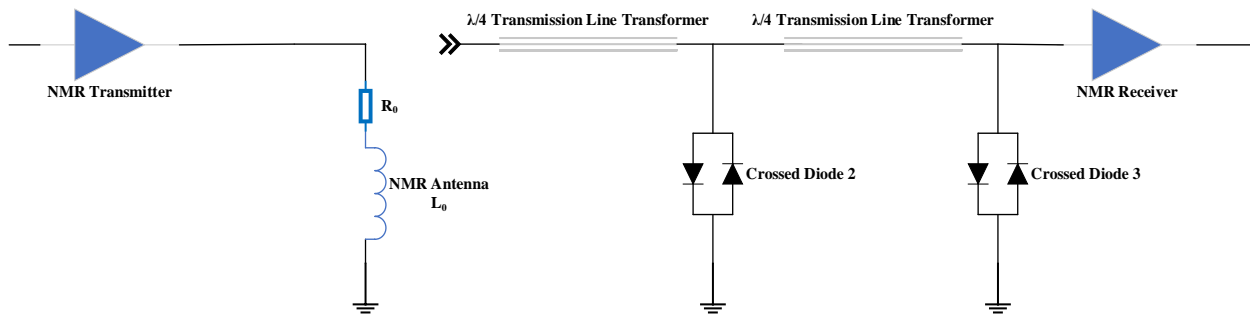


Figure 5.5 NMR coil antenna and duplexer switch based on quarter-wave impedance transformer: transmitter ON

During the NMR signal pick up process, the power amplifier is off. However, its background noise is still overwhelming for the LNA, whose detection range is in $0.1 \mu\text{V}$. As the crossed diodes pair (1) is reversed biased, it becomes open-circuit to block the signal noise from the power amplifier. Meanwhile, under NMR echo signal in μV , the crossed diodes pair (2) is still reversed-biased and therefore is open-circuit from the ground, which makes Z_{load} equal to the input impedance of the LNA, 50Ω . This makes Z_{in} become 50Ω as $Z_{in} = Z_0^2/Z_{load}$, which is equivalent to be closed-circuit on its input port. As a result, the NMR duplexer circuit makes the NMR probe being open-circuit to the NMR transmitter and closed-circuit to the NMR receiver (Figure 5.6).

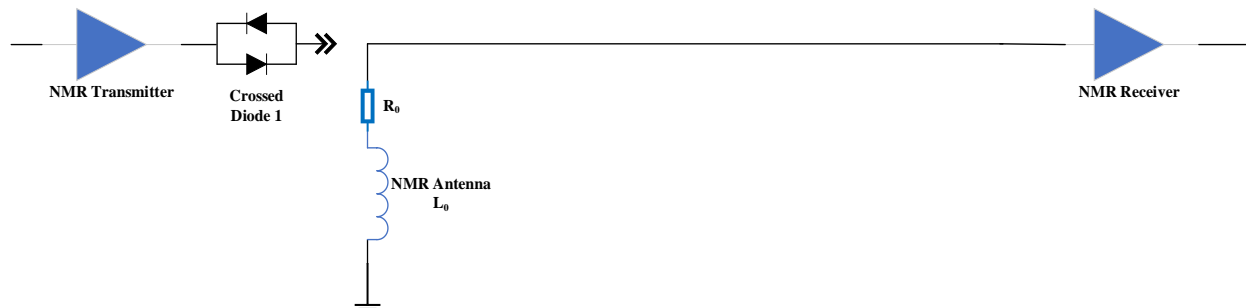


Figure 5.6 NMR coil antenna and duplexer switch based on quarter wavelength transformer:
transmitter OFF

The quarter-wave impedance transformer is built in the Nano-Biosensors Lab. The line length is calculated, $\frac{1}{4} \lambda = 8.1515''$, for the 19.918 MHz NMR frequency. Different diodes are tested to optimize the NMR duplexer performance. It was observed that PIN (p-type/intrinsic/n-type) diodes with fast switching and low parasitic internal resistance yields the best performance. Finally, one set of quarter-wave impedance transformer gave a -20.14 dB signal reduction from the input to the output. Hence, an additional quarter-wave impedance transformer was added to the receiver end of the duplexer for improving filtering of the source signal to -33.98 dB in total. This is sufficient for blocking the background noise from the power amplifier so the weak NMR signal could be detected by the LNA.

5.2.3 Design of Portable NMR Antenna

The NMR probe is an RF antenna, which is installed on the NMR tube to deliver high-power RF energy to sample for NMR excitation and receive echo signal from NMR nuclei precession. The pNMR probe was designed consisting of a coil antenna and the matching networks to optimize both functionalities.

5.2.3.1 Antenna Frequency

The operating frequency of the pNMR probe is determined by the Larmor or precessional frequency, which defines the precession rate of the magnetic moment of the proton under an external magnetic field. The Larmor frequency of nuclei of a substance can be calculated from the Larmor equation as shown in Equation 3 [154].

$$\omega = \gamma B_0 \quad \text{Equation 3}$$

where ω is the Larmor frequency in MHz, γ is the gyromagnetic ratio in MHz/Tesla, and B_0 is the static magnetic field strength in Tesla. The γ of proton, H_1 , equals to 42.58 [155]. Hence the frequency of pNMR probe is calculated as 19.918 MHz.

5.2.3.2 Signal to Noise Ratio

NMR signal is radio frequency radiation released from excited spin state to thermal equilibrium by a small number of hydrogen nuclei in the NMR antenna coil. Due to the weak magnetic field by the handheld magnet, the NMR signal is small, typically in the range of 0.1 μV , and hence difficult to detect. Noise is produced from multiple sources in the system, such as the coil antenna, discrete circuit components, cables, the amplifier, and the receiver. Thus, the signal to noise ratio, SNR, was studied in the design of the portable NMR system to achieve biosensor detection from the complex superimposed background noise.

The SNR of an NMR system can be calculated as the voltage level of the received NMR signal divided by that of the noise signal. During the NMR reception, the voltage difference in the NMR

probe, or the electromotive force ζ (EMF), is induced by a time-varying magnetic field flux passing through a surface, S enclosed by path C , which can be calculated by the Faraday's law of induction as in Equation 4.

$$\zeta = \oint_C \vec{E} \cdot d\vec{l} = - \iint_S \frac{d\vec{B}}{dt} \cdot d\vec{S} \quad \text{Equation 4}$$

where \vec{E} is the electric field, \vec{B} is the magnetic field, \oint_C , and \iint_S are the close integral and surface integral enclosed by path C , respectively.

Based on the principle of reciprocity, for the single coil used in NMR for both transmission and detection, the receive field can be assumed to be equal to the transmit field [156]. Hence, the voltage signal induced by magnetic dipole, \vec{m} , can be calculated using the transmit field strength, \vec{B}_1 , at the same location while current is applied to the same coil, C , during the transmission (Equation 5).

$$\zeta = - \frac{\partial}{\partial t} \{ \vec{B}_1 \cdot \vec{m} \} \quad \text{Equation 5}$$

The values of EMF in all locations of the sample are integrated to calculate the signal produced by the whole sample (Equation 6).

$$\zeta = - \int_{V_s} \frac{\partial}{\partial t} \{ \vec{B}_1 \cdot \vec{M}_0 \} dV_s \quad \text{Equation 6}$$

where V_s is the sample volume in the RF coil, and \vec{M}_0 is the magnetization along the x-y plane (perpendicular to the field plane of the permanent magnet, z).

The value of B_1 is determined by the coil shape. For the long-cylinder shaped coil antenna selected in this pNMR designed, it can be considered as homogeneous over the sample sensing volume. Hence, the Equation 6 can be simplified to as Equation 7.

$$\zeta = K\omega_0 B_{1xy} M_0 V_s \cos \omega_0 t \quad \text{Equation 7}$$

where K is an inhomogeneous factor, ω_0 is the Larmor equation as defined in Equation 3, B_{1xy} is B_1 's component along the x-y plane. The total nuclear magnetism, M_0 can be calculated as shown in Equation 8.

$$M_0 = N(\gamma\hbar)^2 I(I + 1)B_0/3kT_s \quad \text{Equation 8}$$

where N is the spin density at resonance per unit volume, unit volume, γ is the gyromagnetic ratio, I is the main total angular momentum quantum number ($I = 0, 1/2, 1, 3/2, 2, \dots$), and T_s is the sample temperature.

For water proton, a spin $1/2$ system, Equation 9 can be derived using Equation 8 and the population difference between $N_{1/2}$ and $N_{-1/2}$, and further simplified to obtain Equation 10.

$$M_0 = \sum \mu_z N_m = \gamma\hbar(N_{1/2} - N_{-1/2})/2 \quad \text{Equation 9}$$

$$M_0 = 1.02 * 10^{-3} \gamma\hbar B_0/4T_s \quad \text{Equation 10}$$

Therefore, the signal to noise ratio, SNR , can be calculated as Equation 12 by substituting Equation 10 to Equation 7.

$$SNR = \frac{\text{peak voltage of signal}}{\text{rms voltage of noise}} \quad \text{Equation 11}$$

$$= \frac{1.02 * 10^{-3} K \omega_0 B_{1xy} \frac{\gamma \hbar B_0}{4 T_s} V_s}{V_{noise}} \quad \text{Equation 12}$$

where V_{noise} is the rms voltage of noise at the output of the NMR coil, and B_{1xy} is the magnetic field in the transverse plane produced by the unit current in the NMR coil. As a result, to detect the weak NMR signal from the background noise, the SNR should be maximized in the NMR design by optimizing the antenna design for field homogeneity and transmission efficiency, by increasing sample volume and transmit power, and by reducing noise to the receiving amplifier.

5.2.3.3 Antenna Quality Factor

The quality factor, Q could improve SNR by reducing noise and improving antenna efficiency for nuclei excitation. It is a concise performance metric for bandwidth of an antenna [157]. It is defined as the ratio of the power stored in the reactive field over the radiated power [158]. High Q antennas store a lot of power in the near field, which is desirable for NMR proton excitation. In addition, a high value of Q also corresponds to a narrower bandwidth. The higher the quality factor of the NMR probe, the better the signal-to-noise ratio. Hence, high quality factor is desirable for the NMR receiver to discriminate the NMR signal against noise of different frequencies other than the Larmor frequency (Figure 5.7).

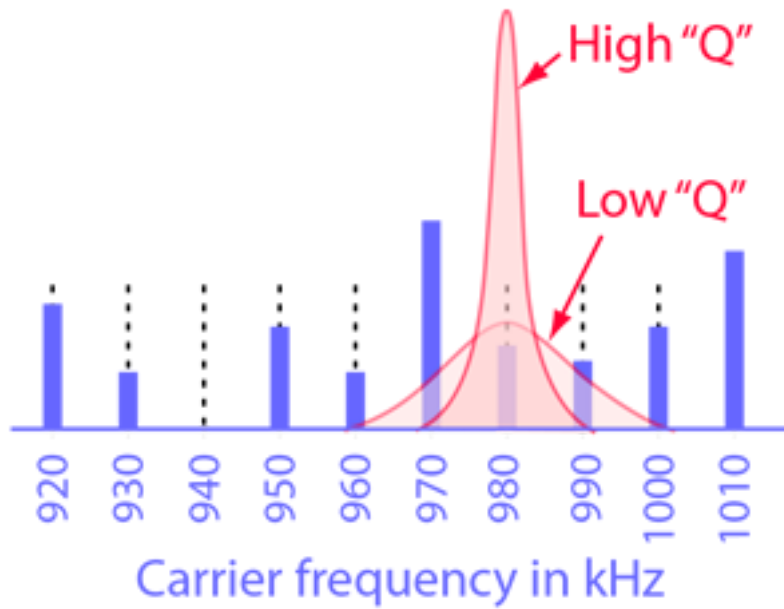


Figure 5.7 A high Q NMR antenna corresponds to higher selectivity, and is more immune to noise for the NMR receiver [153]

The coil antenna is modeled as an inductor in series with parasitic resistance as shown as blue components in Figure 5.8. As a L-R circuit, the quality factor of a coil antenna is calculated as Equation 13.

$$Q = \frac{\omega_0 L_0}{R_0} \quad \text{Equation 13}$$

where ω_0 is the frequency, L_0 is the inductance of the coil antenna, and R_0 is the parasitic resistance of the coil antenna.

5.2.3.4 Sample Volume

Based on Equation 12, the SNR is linearly proportional to the sample volume, which is determined by the coil antenna. NMR antennas in other portable NMR systems, such as flat solenoid and spiral

surface coil, are small in size, but are difficult to achieve uniform field and high volume in the sample due to their coil shapes [132] [134].

5.2.3.5 NMR Antenna

The antenna of the pNMR system selected the design of long-cylinder shaped coil, which is beneficial to achieve high field homogeneity and sample volume. It was fabricated using high-quality enameled copper wire by winding on a steel rod of the same diameter as the NMR sample tube, $\Phi 5$ mm. Antennas by different wire diameters were fabricated and tested for L_0 and R_0 using an Agilent LCR meter at 19.918 MHz, to optimize quality factors and sample volume for NMR performance. The test results indicate that coil by 8 turns of $\Phi 1$ mm wire (8 mm in length and 5 mm in inner diameter) is the optimal for NMR antenna. Antenna made with thinner wires leads to higher parasitic resistance, while thicker wires end up with fewer turns, thereby reducing inductance. Hence, both cases have a negative impact on the quality factor. Such designs lead to a big sample with volume of 180 μL , which is more than 10 times larger compared to other portable NMR systems reported in the literature [132] [134].

5.2.4 Design of Matching Networks of the pNMR Probe

The function of NMR probe is to deliver RF energy from the power amplifier on the transmitter and pick up NMR echo signal to the low noise amplifier on the receiver. Impedance matching is an essential design practice to maximize the power transfer and minimize signal reflection from the load.

Based on the transmission principle of wave or RF signal, the reflection is calculated by reflection coefficient, the complex ratio of the voltage of the reflected wave to that of the incident wave Equation 14.

$$\begin{aligned}\Gamma_{LS} &= \frac{V_{Reflect}}{V_{Incident}} \\ &= \frac{Z_S - Z_L}{Z_S + Z_L}\end{aligned}\tag{Equation 14}$$

where Γ_{LS} is the reflection coefficient from load to source, $V_{Reflect}$ and $V_{Incident}$ are the voltage of the reflected and incident wave, the Z_S is the source impedance, and Z_L is the load impedance. Thus, when the input impedance of the electrical load matches with the output impedance of its corresponding signal source, the reflection equals to zero, therefore transmitting all the RF signal to the load.

The coil antenna is an inductor but with parasitic resistance (Figure 5.8). Hence, a matching network is required to transform its impedance to 50Ω in order to match with the output impedance of the power amplifier and the input impedance of the low noise amplifier (both being 50Ω) for maximum signal/power transmitting and receiving.

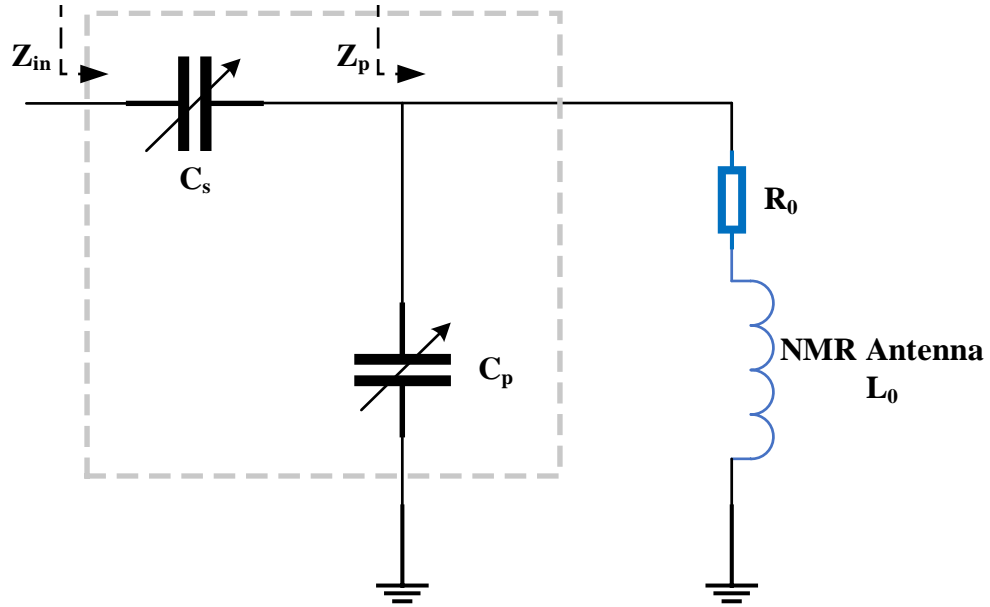


Figure 5.8 The NMR probe, consisting of NMR coil antenna and a matching network, was designed to achieve high quality factor to optimize NMR signal acquisition.

The matching network is designed based on series-parallel resonance circuit comprising of a parallel capacitor, C_p , and a series capacitor, C_s , onto the coil antenna. The total impedance can be modeled as, Equation 15, where Z_{in} is the input impedance of the NMR probe, including the NMR coil antenna and the matching network.

$$Z_{in} = \frac{1}{j\omega C_s} + \frac{\frac{1}{j\omega C_p} (j\omega L_0 + R_0)}{\frac{1}{j\omega C_p} + j\omega L_0 + R_0} \quad \text{Equation 15}$$

The complex impedance of Z_{in} can be decomposed as the real component, $R(\omega)$, and the reactive component, $X(\omega)$, as Equation 16. $R(\omega)$ and $X(\omega)$ can be further calculated based on the resistance, capacitance, and inductance of each circuit component.

$$Z_{in} = R(\omega) + jX(\omega) \quad \text{Equation 16}$$

$$R(\omega) = \frac{R_0}{(1 - \omega^2 L_0 C_p)^2 + \omega^2 R_0^2 C_p^2} \quad \text{Equation 17}$$

$$X(\omega) = -\frac{1}{\omega C_s} + \frac{(1 - \omega^2 L_0 C_p)\omega L_0 - \omega^2 R_0^2 C_p}{(1 - \omega^2 L_0 C_p)^2 + \omega^2 R_0^2 C_p^2} \quad \text{Equation 18}$$

As indicated in Equation 17 and Equation 18, the real part of Z_{in} can be adjusted by C_p to match with that of the power amplifier output, Z_{PA} . Meanwhile, the inductive reactance of Z_{in} can be resonated out by C_s , therefore corresponding to $Z_{in} = Z_{LNA} = Z_{PA} = 50 \Omega$.

The resistance and inductance of the coil antenna was measured as described above to determine the capacitance of C_s and C_p . The coil antenna, that with an empty NMR tube, and with DI water were measured by an Agilent LCR meter, respectively. The measurement and calculation results are summarized in Table 5.1.

Table 5.1 Matching network design based on NMR probe characterization through resistance and inductance measurement

	R_0 (Ω)	L_0 (nH)	C_p (pF)	C_s (pF)
Coil only	1.36	685.70	77.8	15.43
NMR tube	1.45	712.29	74.41	15.33
NMR tube with DI water	1.46	714.69	74.12	15.32

It is observed that inserting the NMR tube impacts both resistance and inductance of the coil antenna, while that of water, the NMR target, was negligible. The NMR tube is of instrumental grade and commercially available. It is made of pure high-quality quartz and is non-magnetic, which will not affect the electromagnetic field generated by the coil antenna. Hence, its antenna impact is mainly by coil enlargement due to the insertion. Considering this factor, the C_p and C_s are accurately calculated as 74.12 pF and 15.32 pF, respectively. A 50 pF fixed capacitor in parallel with a 50 pF variable capacitor were chosen for C_p , while a 10 pF fixed capacitor in parallel with a 10 pF variable capacitor were chosen for C_s . It is worth noting that the quality of the capacitor: high Q and low parasitic resistance, is essential to achieve high quality factor for the NMR probe.

Based on the design, an NMR probe comprising of NMR coil antenna, NMR sample tube, tuning circuit, and non-magnetic probe holder is fabricated in the Nano-Biosensors Lab. Its RF performance was tuned and evaluated as described as follows.

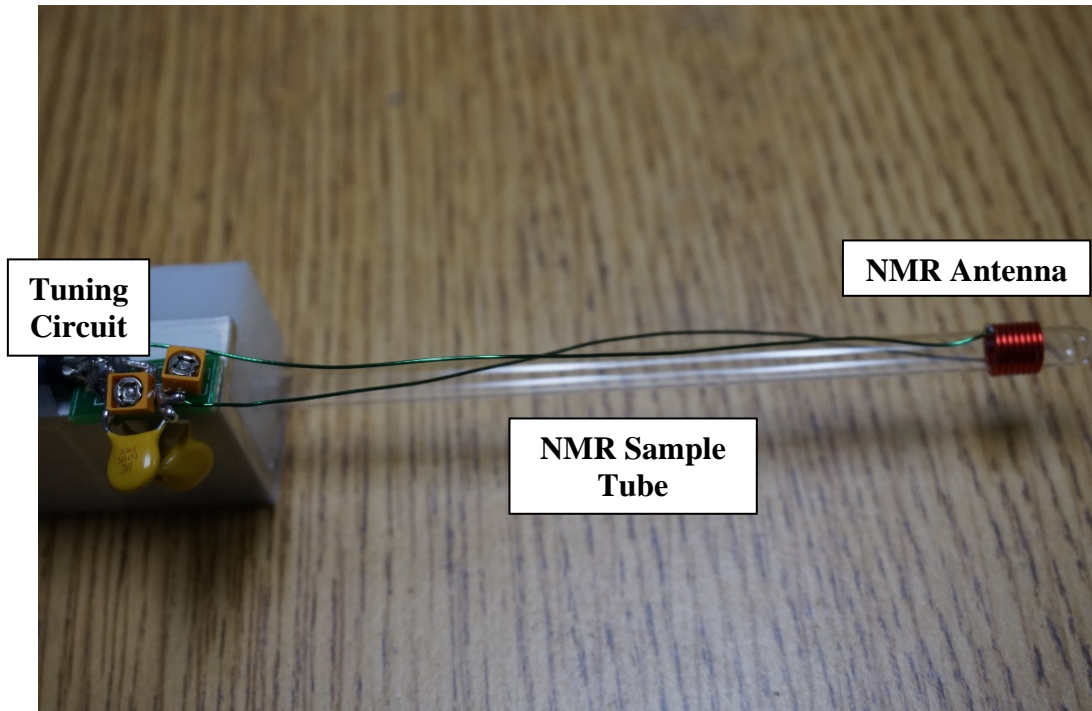


Figure 5.9 NMR probe comprising of NMR coil antenna, NMR sample tube, tuning circuit, and non-magnetic probe holder is designed and fabricated in the Nano-Biosensors Lab.

5.2.5 Evaluation of the Portable NMR Probe and the Matching Networks

The performance of the NMR probe, including reflection coefficient (S_{11}) and quality factor (Q), were evaluated using a Keysight E5062 vector network analyzer (VNA). During the testing, the NMR probe system, including the coil antenna and the matching networks, is connected to the port 1 of the VNA, as shown in Figure 5.10. The VNA transmits RF signals to the NMR probe at frequencies scanning from 0 to 40 MHz and measures the reflected power from the probe for each frequency point. The VNA measures the reflection coefficient, S_{11} , which describes how much of a RF signal is reflected by an impedance discontinuity in the transmission system. It is defined by the two-port theory as Equation 19 [152].

$$S_{11} = 20 \log_{10} \left| \frac{E_r}{E_i} \right| = 10 \log_{10} \left(\frac{P_r}{P_i} \right) \quad \text{Equation 19}$$

where E_r and E_i are the reflected and incident fields, P_r and P_i are the reflected and incident power, respectively. The S_{11} measures how much power is reflected back to the power amplifier. Since the input power to the probe equals to the sum of the incident power and the reflected power, the S_{11} measures the probe's total efficiency of power transmission into the sample for the NMR excitation.

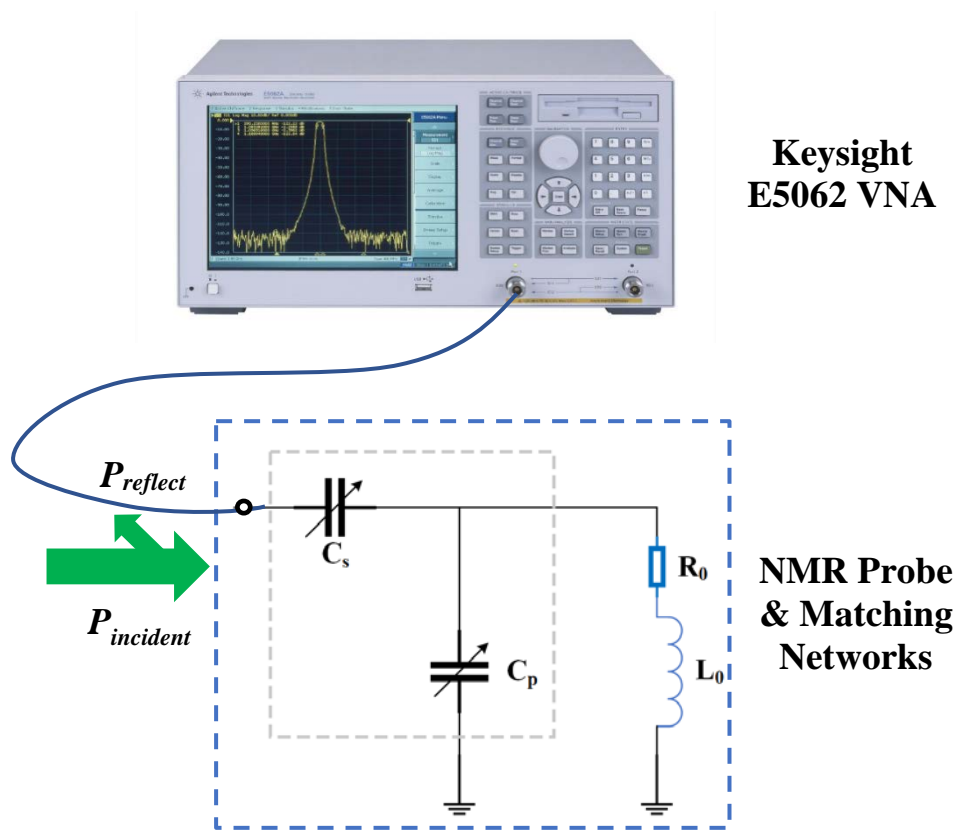


Figure 5.10 The NMR probe evaluation using a Keysight E5062 VNA for reflection coefficient and quality factor. Its matching network was tuned while measuring using the VNA to optimize the reflection coefficient (S_{11}) and achieved -23.6 dB.

The matching networks was tuned by adjusting two tuning capacitors, C_p and C_s to minimize the reflection coefficient at the NMR operating frequency, 19.918 MHz. A S_{11} of -23.6 dB was achieved for 19.918 MHz, which indicated that 0.4% of input power was reflected and 99.6% was transmitted for NMR (Figure 5.11).

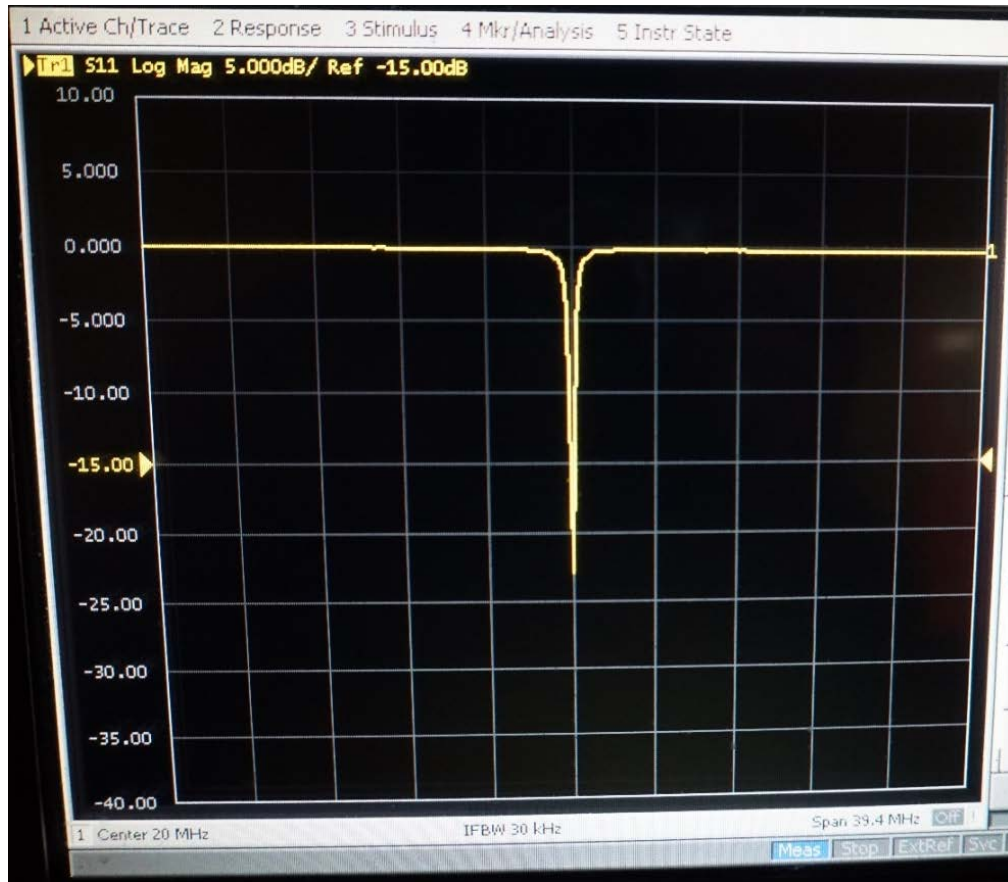


Figure 5.11 The NMR probe was designed to achieve high quality factor to optimize NMR signal acquisition. Its matching networks was tuned to optimize the reflection coefficient using a VNA and achieved -23.6 dB at 19.918 MHz.

The matching networks consisted of two capacitors, which were reactive circuit elements. The remaining signal that was not reflected was assumed to be transmitted and passed to the sample.

Thus, the quality factor of the NMR probe could be calculated from the reflection coefficient results using Equation 20 below.

$$Q = \frac{f_0}{\Delta f} \quad \text{Equation 20}$$

where f_0 is the antenna frequency, and Δf is the antenna bandwidth. Based on the S_{11} experimental data (Figure 5.11), the bandwidth is the frequency difference at 3 dB points below the peak amplitude, where $f_0 = 19.918$ MHz at -23.6 dB, $f_1 = 19.898$ MHz at -20.6 dB, and $f_2 = 9.927$ MHz at -20.6 dB. Hence, the quality factor could be calculated as, $Q = 19.918 / (19.927 - 19.898) = 686.8$. However, an accurate measurement of the Q -factor using a one-port measurement is difficult, and two-port techniques should be implemented [159].

To compare performance, two NMR probes (from Bruker Inc.) were evaluated for the quality factor using the VNA as described above. After tuning the matching networks, their Q 's were measured as, 64.04 and 538.32, respectively. Liu et al. built a solenoidal coil-based NMR probe with Q of 200 [132]. Sun et al. built a planar microcoil-based NMR probe with Q of 16 [134]. In summary, the pNMR's probe, designed and fabricated in the Nano-Biosensors Lab, achieved better Q than those in the commercially available systems and in the existing literature. Hence, the probe of the pNMR is very efficient at delivering energy to the sample and achieving a high SNR for the detected NMR signal, which are beneficial for detecting lower concentration pathogens in complex samples.

5.2.6 NMR Power Amplifier

The power amplifier is used in the pNMR system to amplify the RF pulses to a specific power level in order to rotate the sample magnetization to the desired angle effectively and repeatably. When the input impedance of the NMR probe is tuned to match with the power amplifier output (50Ω), all the output power of the amplifier will flow in the coil without any reflection. The amplifier power required for magnetization rotation can be calculated by the equivalent resistance, R_{eff} , and the NMR probe current, I (Equation 21).

$$P = \frac{1}{2} I^2 R_{eff} \quad \text{Equation 21}$$

$$R_{eff} = R_{sample} + R_{probe} + R_r \quad \text{Equation 22}$$

The equivalent resistance is contributed by the sample, R_{sample} , the coil, and matching network circuit, R_{probe} , and radiation resistance, R_r (Equation 22). This was measured on the NMR probe loaded with a test sample using a VNA at the NMR frequency of 19.918 MHz. The measurement result is shown in Table 5.1.

The probe current is determined by the induced magnetic field strength, B_{1xy} , the pulse width, τ_p , and the flip angle α as shown in Equation 23. One example of the application is the Carr-Purcell-Meiboom-Gill (CPMG) experiment, which is based on RF pulses to achieve flip angles of 90° and 180° .

$$\alpha = \omega T = (\gamma B_{1_{xy}})\tau_p \quad \text{Equation 23}$$

The magnitude of the induced magnetic field $B_{1_{xy}}$ is determined by the antenna. For the coil antenna of the pNMR, it can be modeled as Equation 24.

$$B_{1_{xy}} = \mu_0 n I \frac{1}{\sqrt{d^2 + l^2}} \quad \text{Equation 24}$$

where l is the coil length, d is the coil diameter, and n is solenoid turn number of the coil. Hence, the coil current, I , can be obtained from Equation 23 and Equation 24. Substituting I to Equation 21, the required amplifier output power can be calculated as defined in Equation 25.

$$P = \frac{1}{2} R_{eff} \left(\frac{\alpha}{\gamma \tau_p \mu_0 n} \right)^2 (d^2 + l^2) \quad \text{Equation 25}$$

To generate a 90° magnetization RF pulse in 7 μsec , or a 180° RF pulse in 14 μsec , the transmit power was calculated to be, 13.57 W using Equation 25. The required amplifier output power was calculated to be 20 W, taking into account of the crossed diode loss and the harmonics loss, which were measured as 1.11 dB and 0.76 dB, respectively. These losses occurred in the T/R switch and power amplifier, which were before the NMR probe. Therefore, they did not affect the NMR probe evaluation by Q measurement in section 5.2.5.

NMR detection relies on sinusoidal RF waves to excite the nuclear spins of the test sample. Therefore, a linear power amplifier is required for this application. In addition, the NMR signal is

weak, ranging around 0.1 μV . The NMR reception can still be interfered by the amplifier noise leaking to the receiver, even after the $\lambda/4$ duplexers has switched the antenna from the power amplifier to the receiver. To solve this problem, a high-speed solid-state RF switch, ZYSW-2-50DR (mini-circuits Inc.) was selected to switch the RF signal from the input of the power amplifier to a 50 Ω RF load [135]. The input switching along with the CPMG sequence pulsation were precisely controlled by an embedded software programmed in Very High Speed Integrated Circuit Hardware Description Language (VHDL) on the Spartan-3 FPGA control board running at 300 MHz operation speed [136]. As a result, a linear amplifier with continuous wave (CW) capability was required to fulfill the requirements of transient response and high-speed switching.

Based on the pNMR requirements on frequency, power, and operating mode, we identified the 50B HF power amplifier from Henry Radio Inc. as suitable for the pNMR application. The RF performance of the 50B HF amplifier is summarized in Table 5.2 below [137].

Table 5.2 RF performance of Henry Radio 50B HF power amplifier, including output power, frequency range, and operating mode.

Henry Radio 50B HF Power Amplifier	
Parameter	Specification
Watts In/Out	CW – 1 mW to 40 W
Bandwidth	1.8 to 30 MHz
Mode	SSB, CW or FM
DC Volts/amps	26.0 VDC - 4 A

To transfer 20 W output power to the NMR probe, the input power was calibrated through testing of the NMR transmitter, consisting of the RF switch, power amplifier, crossed diodes, and two $\lambda/4$ wavelength duplexers, using the testing setup shown in Figure 5.12. A Tektronix AFG3021 function generator was connected to the transmitter input to provide RF signal at 19.918 MHz. An oscilloscope was connected to the transmitter output to measure the RF signal on a 50 Ω load simulating the antenna, and the output's sinusoidal waveform, switching performance, frequency, and RF power were verified and measured.

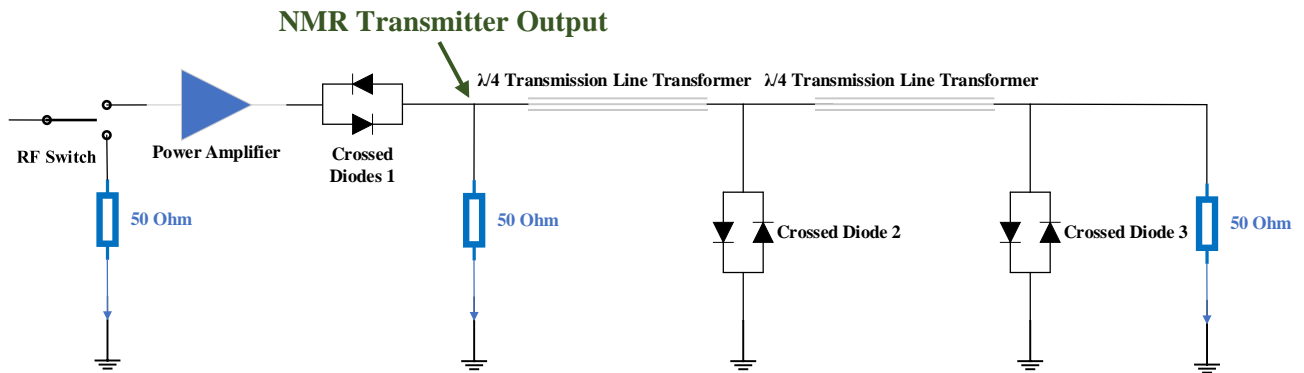


Figure 5.12 Testing set up of the NMR transmitter using the function generator, 50 Ω loads and oscilloscope to calibrate the input power required for pNMR application.

The input power of the NMR transmitter was calibrated to be 0.02 mW, 0.06 mW, and 0.08 mW to achieve output powers of 5.2 W, 16.0 W, and 20.0 W (45.6 Vpp, 80.0 Vpp, and 89.5 Vpp), as illustrated in Figure 5.13. The amplification gains were measured as 55.0 dB, 54.5 dB, and 54.0 dB, respectively. It is specified to be 53.0 dB by the supplier. Hence, the calibration experiment is essential to make an accurate detection for NMR.

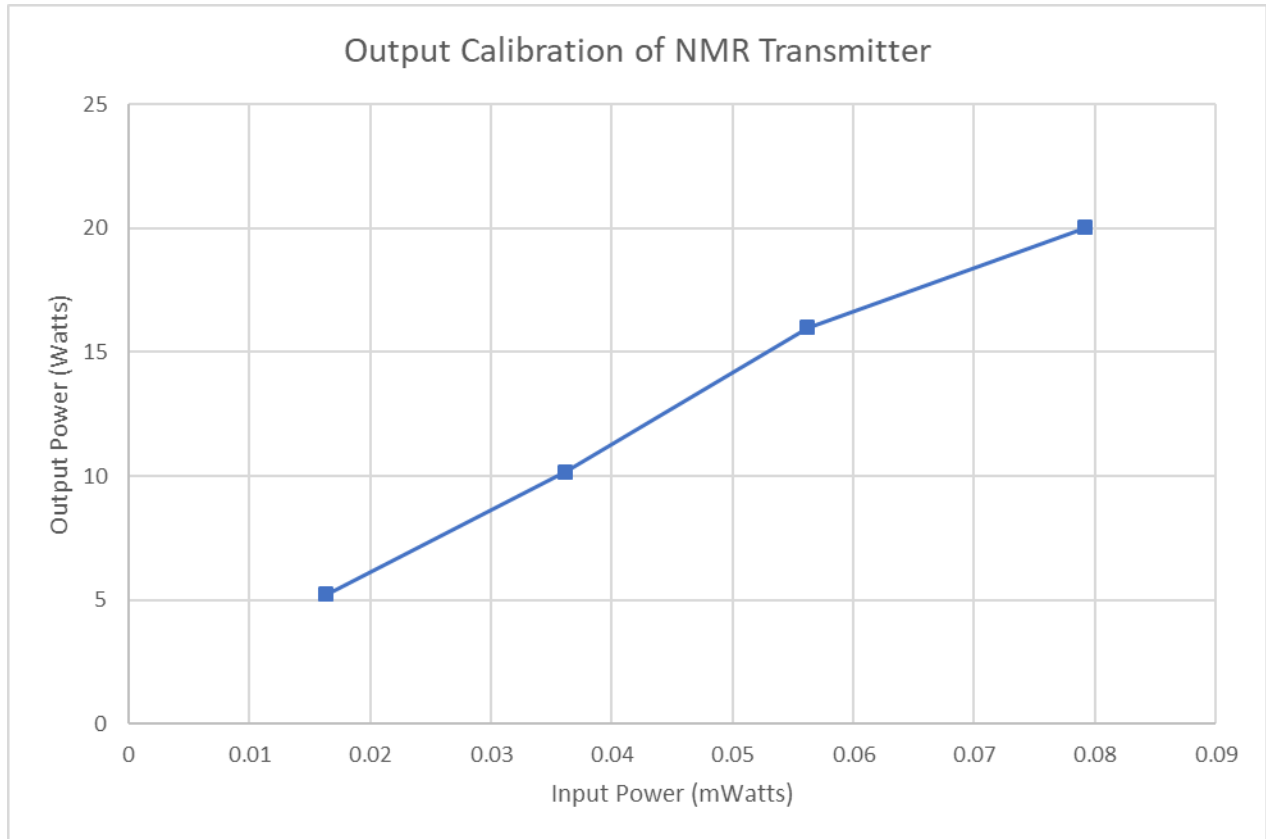


Figure 5.13 The input power to the NMR transmitter was calibrated to achieve 20 W output to the NMR probe.

5.2.7 NMR Low Noise Amplifier

To detect NMR signal of $0.1 \mu\text{V}$ in a noisy environment, the receiving amplifier is required to be low in its own noise and have high a gain higher than 60 dB to allow RF demodulation by the mixer. We identified AU-1467 low noise amplifier (LNA) from Narda Miteq Inc. with an amplification gain of 67.9 dB and noise figure of 1.2 dB suitable for this NMR application [138]. Its RF performance is summarized in Table 5.3 below.

Table 5.3 RF performance of Miteq AU-1467 low noise amplifier, including frequency range, gain, and noise figure.

Miteq AU-1467 Low Noise Amplifier	
Parameter	Specification
Frequency Range	10-600 MHz
Gain	65 dB Min, 67 dB Typical
Gain Flatness	+/- 1 dB Max
Input VSWR	2.0:1 Max
Output VSWR	2.0:1 Max
Noise Figure	1.2 dB
Output P1dB	+12 dBm Min

The LNA was tested using the NMR receiver setup (including two $\lambda/4$ transmission line transformers) as shown in Figure 5.14. A sinusoidal test signal of 0.1 V amplitude and 19.918 MHz frequency was generated by the function generator. It was attenuated to be 0.1 μ V using Mini-circuits RF attenuators (120 dB total attenuation) to simulate the NMR output signal. Finally, the attenuated signal was transmitted to the LNA through two $\lambda/4$ transmission line transformers so that the circuitry remained the same as it was in the full pNMR system.

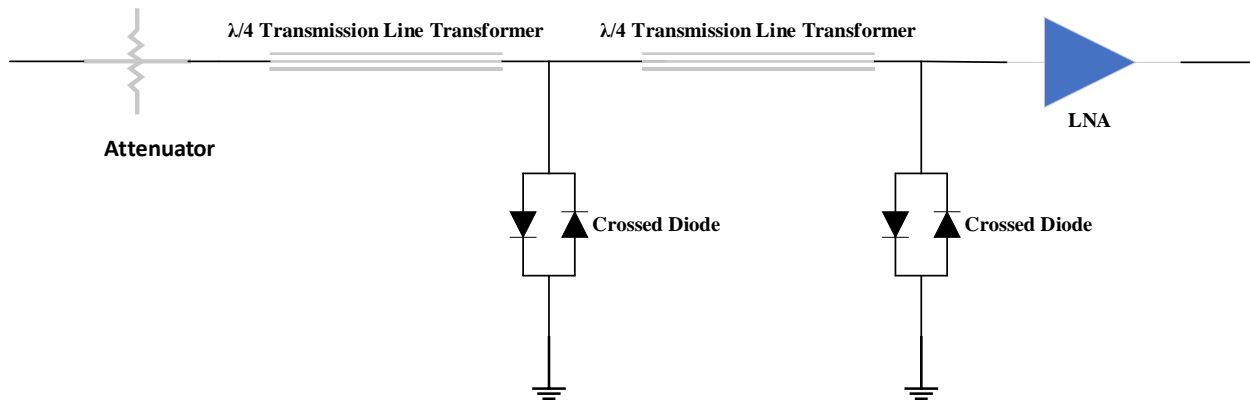


Figure 5.14 Testing set up of the NMR receiver using the function generator, attenuators, and the oscilloscope to evaluate the LNA with the $\lambda/4$ wavelength duplexers.

The LNA output was evaluated using a Tektronix oscilloscope. With the scope's built-in amplification by 40 dB, the amplitude of the LNA output was measured to be 24.8 mV, indicating that the amplification gain of LNA is 67.9 dB (fulfill the design requirement). The output waveform was sinusoidal with frequency measured to be 19.918 MHz. These test results demonstrated that the LNA could detect the weak NMR signal in the range of 0.1 μ V.

A previous attempt was to use a Sonoma Instrument 310 amplifier as the LNA of the pNMR [139]. Its performance of bandwidth and noise figure both meet the system requirement (Table 5.4), however its gain of 32.5 dB was insufficient to recover the weak NMR signal. It could not detect the 0.1 μ V test signal in the set up above or the pNMR detection of pure water sample.

Table 5.4 RF performance of Sonoma Instrument 310 low noise amplifier, including frequency range, gain, and noise figure.

Sonoma Instrument 310 Low Noise Amplifier	
Parameter	Specification
Frequency Range	9 kHz - 1 GHz
Gain	32.5 ± 1.5 dB
Gain Flatness	+/- 0.5 dB Max
Noise Figure	1.8 dB typ.
Output P1dB	+10 dBm

5.2.8 NMR Detection using Magnetic Nanoparticle

A nuclear magnetic resonance (NMR) instrument allows analyzing the content of a sample and its molecular structure by measuring frequency and duration of electromagnetic signal emitted from nuclear spin relaxation [162]. Both features of the NMR signal are determined by the atomic and molecular properties of the sample as well as its applied external magnetic field. To better analyze the sample's intrinsic properties, the magnetic field needs to be close to the ideal states: being strong in strength in order to achieve dispersion of response frequencies, while of very high homogeneity and stability over the entire sample space in order to deliver frequency resolution to reveal the details of chemical shifts and the Zeeman effect. To fulfill these conditions, the NMR system has complex and expensive magnet system to achieve highly uniform magnetic field ranging from 1.5 to 20 Tesla, which needs to be made of rare-earth strong magnetic magnets with complex design for field uniformity, or even by liquid- helium/nitrogen cooled superconducting

coils consuming large currents. Although the configuration produced accurate results, the NMR instruments were rather large, heavy, not portable, and expensive [163][164]. This has made the NMR technique less practical and less useful for on-site applications, as demonstrated in Figure 5.15.



Figure 5.15 The Conventional nuclear magnetic resonance (NMR) spectrometer, Bruker 700 MHz NMR system [165].

Magnetic nanoparticle (MNP) is a unique material with a range of desirable properties, including nano sizing, high surface-to-volume ratio, self-prevention from agglomeration, and strong magnetization strength (hundreds of emu) [166]. Each MNP can function as a separate nanomagnet. Owing to its high quantity-to-volume ratio, a tiny amount of MNPs could achieve

tens of millions of nano magnets, each interacting with the external magnetic field, and effectively inducing field distortion. As aforementioned in the previous paragraph, since nuclear spin interaction is very sensitive to the uniformity of the external magnetic field, when a few MNPs bound to their intended molecular target through antibody affinity, this can lead to an effective reduction in the bulk spin-spin relaxation time (T_2) of the surrounding water molecules. Using a palm-sized permanent magnet with lower strength and uniformity, the difference in T_2 shortening caused by different target concentration could be effectively detected without the need for an instrument-level NMR system.

In addition, owing to the excellent penetrability of the detection signal, MNP-based NMR biosensor can be used to measure turbid samples with less sample preparation. The detection time is shorter than those with surface-based techniques relying on the targets' molecular diffusion to the sensing elements. The measurement is non-destructive, allowing characterization by other detection methods afterwards. These advantages make the MNP-NMR ideal for fast, simple, and high-throughput sensing applications, especially in portable form factor. Being more flexible and smaller in size, the MNP-NMR is suited for on-site and field-based measurements. This class of biosensors can be developed and manufactured in low cost and are less costly to operate and maintain as compared to bulky conventional NMR instruments.

In the Nano-Biosensors Lab, we developed and built a portable MNP-NMR biosensor using a palm-sized magnet of 0.5 Tesla field strength [160][161]. We also developed an antibody-functionalized superparamagnetic MNP for the biosensor application [160][167]. Each superparamagnetic MNP consists of a maghemite ($\gamma\text{-Fe}_2\text{O}_3$) magnetic core and a polyaniline shell.

The synthesis process was tuned for size and magnetic property, achieving a uniform average diameter of 80 nm and a total distribution of 50 nm to 100 nm. The MNP has strong saturation magnetization (M_s), 38 emu/g as indicated by M-H hysteresis measurement. The coercivity (H_c) was found to be the same as the unmodified Fe_2O_3 particles, 180 Oe. This indicates that the polyaniline shell did not affect the MNP's anisotropy energy, which is essential to modify both the NMR precession frequencies and the thermodynamic occupation probability of the crystal magnetic states. Hence, our superparamagnetic MNP is favorable to shorten the NMR relaxation, and to be used as proximity sensors to amplify molecular interactions.

For the target pathogen detection, we developed surface-functionalization method to conjugate antibodies onto the MNP by physical non-covalent adsorption [160][161]. We designed and optimized the process to label the target pathogen with MNP by antibody-antigen binding. Owing to signal penetration capability of the NMR, simple filtration method using a syringe filter was found to be effective to remove excessive MNPs for both water and food samples. Then, the MNP concentration becomes proportional to the target pathogen concentration.

Finally, the target pathogen concentration can be detected by the MNP-NMR biosensor by measuring the NMR spin-spin relaxation time (T_2) of water proton in the sample, which is inversely proportional to the MNP concentration. The MNP effect on NMR relaxation is described based on the general theory as follows.

5.2.9 Effects of MNP on NMR Relaxation

Like electrons, the nucleus with unpaired protons or neutrons have an intrinsic quantum property of nuclear spin, which is characterized as quantized angular momentum, S . As circular current generates a magnetic field by Ampere's law, a spinning nucleus also acts like a magnet of magnetic moment of μ defined in Equation 26,

$$\mu = \gamma S = \gamma m \hbar \quad \text{Equation 26}$$

where m is the magnetic quantum number, \hbar is the reduced Planck constant, and γ is the gyromagnetic ratio, a constant specific to the type of the nucleus.

When placed in a magnetic field, nucleus would align along or against the field direction, creating a low energy state and a high energy state in Equation 27,

$$E = \mu B_0 = \gamma m \hbar B_0 \quad \text{Equation 27}$$

where m equals to 1/2 or -1/2 as quantum spin number for proton. The energy "bandgap" between the high- and low- energy states equals to, $\gamma \hbar B_0$, which is linearly proportional to B_0 , as illustrated in Figure 5.16.

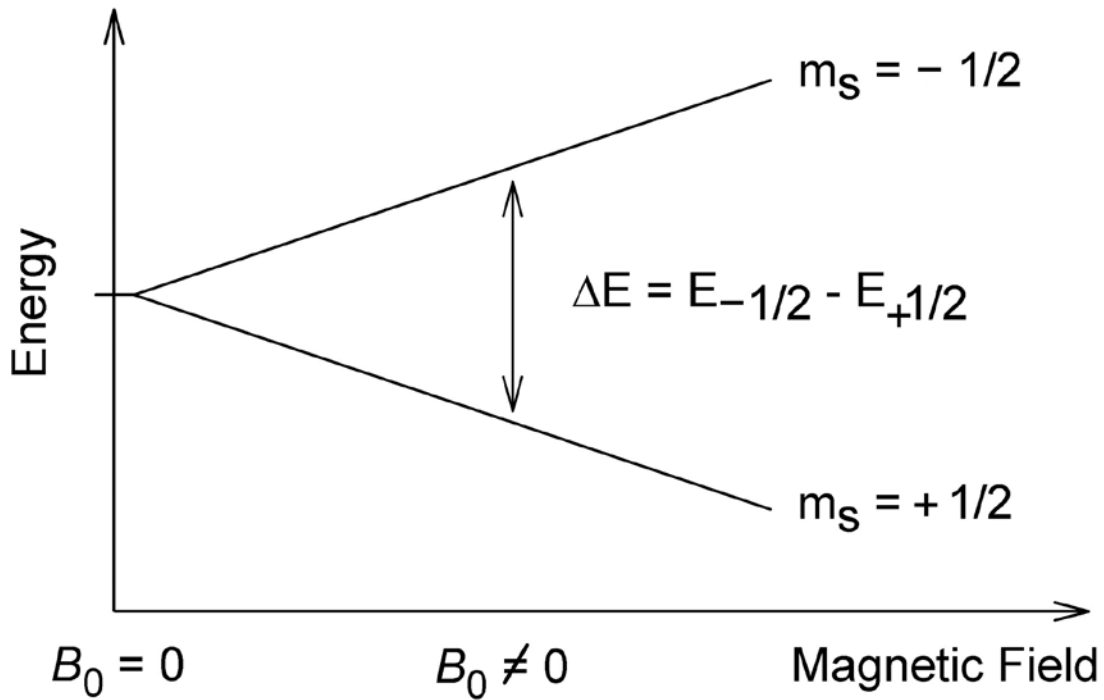


Figure 5.16 The Zeeman effect: nuclei spin energies split when placed in an external magnetic field [168].

Similar to charged particles precessing around a magnetic field, a charged nucleus, such as protons of water molecules, will exhibit precession motion at a characteristic resonance frequency, called Larmor frequency, ω_0 , which is determined by nucleus's intrinsic quantum property and strength of the magnetic field where the sample was placed in (Equation 28).

$$\omega_0 = E/\hbar = \gamma B_0 \quad \text{Equation 28}$$

The nucleus can be excited from low-energy state to high-energy state by absorbing energy from the oscillating magnetic field generated by the radio frequency (RF) signal at or close to Larmor frequency.

After the excitation, the nucleus continues to exchange energy with their surroundings, also called lattice, through thermal motion induced magnetic dipole-dipole interactions, and eventually bring the population of spin energy state back to the thermal equilibrium. This process is called spin-lattice relaxation, or T_1 relaxation, in which T_1 denotes the duration.

Similar with nucleus' absorption of RF signal, the energy exchanges between the spin and lattice require the thermal motion/fluctuation occurring at a frequency at or close to the NMR resonance frequency. Thus, the effectiveness of the process is determined by the number of the frequency matched population.

For a simple case of uncoupled spins of 1/2, the major source of T_1 relaxation is dipolar coupling (DC), which is the interaction between adjacent nuclear spins, I and S , through space (Figure 5.17). The spin S induces a local field B_{loc} at the spin I , characterized by spin position function, $F(t)$, as defined in Equation 29.

$$B_{loc}(t) = \mu_s \frac{[3\cos^2\theta(t) - 1]}{r_{IS}(t)^3} = \mu_s F(t) \quad \text{Equation 29}$$

where $r_{IS}(t)$ is the distance between spin I and S , and $\theta(t)$ is the angle between I - S axis and the external magnetic field, B_0 .

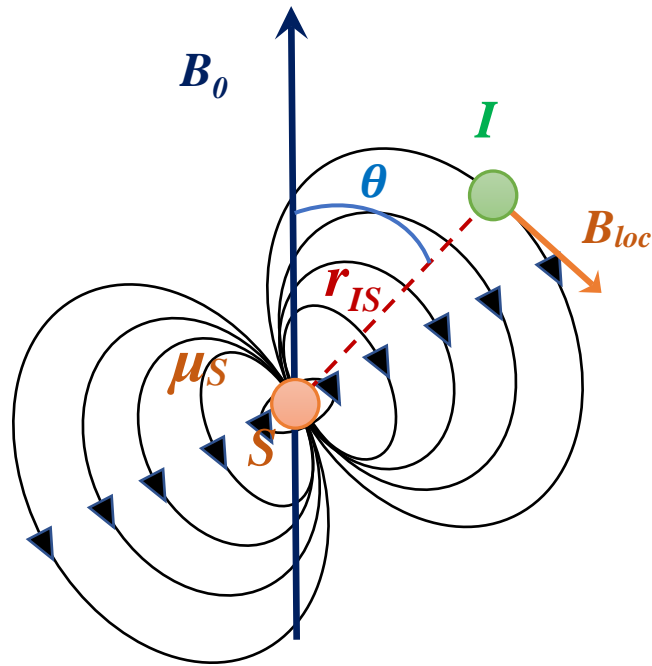


Figure 5.17 Dipolar interaction between nuclear spins, I and S, through space. The spin S induces a local field B_{loc} at the spin I.

Nuclei fluctuated by thermal motion experience different local field, causing Zeeman interaction fluctuating randomly with B_{loc} [169]. The physical effect of this random process can be described in the frequency domain by a spectral density function, $J(\omega)$, which is the Fourier transform, defined in Equation 31, of an autocorrelation function, $C(t)$ (Equation 30), for the randomly fluctuating local magnetic field, B_{loc} . As a result, $J(\omega)$ is the amount of motion at different frequencies, as derived in Equation 32.

$$\begin{aligned}
 C(t) &= \langle B_{loc}(0)B_{loc}(t) \rangle \\
 &= \mu_S^2 \langle F(0)F(t) \rangle
 \end{aligned}
 \tag{Equation 30}$$

$$J(\omega) = \frac{1}{2\pi} \int_{-\infty}^{+\infty} C(t) e^{-i\omega t} dt \quad \text{Equation 31}$$

$$J(\omega) = 2\langle B_{loc}^2 \rangle J(\omega) \quad \text{Equation 32}$$

where $F(t)$ is the function of the relative position interacting spins, the brackets represent an averaging, and $J(\omega)$ is the normalized spectral density function.

The T_1 of spin-lattice relaxation is the decay time of the net spin magnetization along the external magnetic field direction (z -axis), M_z , that is reduced by the DC energy exchange. For two spin system, M_z can be modeled as Equation 33,

$$M_z = \frac{2}{B} (\rho_{1/2} - \rho_{-1/2}) \quad \text{Equation 33}$$

where $\rho_{1/2}$ and $\rho_{-1/2}$ are the population at the two spin states, 1/2 and -1/2, respectively, and B is the Boltzmann factor, $B = \frac{\hbar\gamma B_0}{k_B T}$.

The kinetic of population variation of $\rho_{1/2}$ and $\rho_{-1/2}$ are derived as Equation 34 and Equation 35, respectively.

$$\frac{d}{dt} \rho_{1/2} = -P_{1/2}^{-1/2} \rho_{1/2} + P_{-1/2}^{1/2} \rho_{-1/2} \quad \text{Equation 34}$$

$$\frac{d}{dt}\rho_{-1/2} = +P_{1/2}^{-1/2}\rho_{1/2} - P_{-1/2}^{1/2}\rho_{-1/2}) \quad \text{Equation 35}$$

$P_{1/2}^{-1/2}$ and $P_{-1/2}^{1/2}$ are the transition probability between the two spin energy states defined as Equation 36 and Equation 37 respectively, where P is the mean transition probability.

$$P_{1/2}^{-1/2} = P(1 - B/2) \quad \text{Equation 36}$$

$$P_{-1/2}^{1/2} = P(1 + B/2) \quad \text{Equation 37}$$

Thus, the kinetic of M_z can be obtained the last four equations as Equation 38,

$$\begin{aligned} \frac{d}{dt}M_z &= \frac{2}{B} \left(\frac{d}{dt}\rho_{\frac{1}{2}} - \frac{d}{dt}\rho_{-\frac{1}{2}} \right) \\ &= -2P(M_z - 1) \end{aligned} \quad \text{Equation 38}$$

Solving the above first order differential equation, the normalized $M_z(t)$ can be obtained as derived in Equation 39,

$$M_z(t) = [M_z(0) - 1]e^{-2Pt} + 1 \quad \text{Equation 39}$$

Hence the relaxation rate, R_1 , or the reverse of T_1 can be obtained from this exponential decay function as defined in Equation 40.

$$R_1 = \frac{1}{T_1} = 2P \quad \text{Equation 40}$$

As aforementioned previously, $J(\omega_0)$ gives the amount of thermal motion at the resonance frequency, and hence determines the mean transition probability, as derived in Equation 41.

$$P = \frac{\gamma^2}{4} J(\omega_0) = \frac{\gamma^2}{2} \langle B_{loc}^2 \rangle J(\omega_0) \quad \text{Equation 41}$$

Hence, the spin-lattice relaxation rate, R_1 , is then described by the spectral density at the spin resonance frequency, $J(\omega_0)$, or the Fourier transform for the autocorrelation of spin position function, $F(t)$, as derived in Equation 42.

$$\begin{aligned} R_1 &= 2P = \frac{\gamma^2}{2} J(\omega_0) = \frac{\gamma^2}{4\pi} \int_{-\infty}^{+\infty} C(t) e^{-i\omega t} dt \\ &= \frac{\gamma^2 \mu_s^2}{4\pi} \int_{-\infty}^{+\infty} \langle F(0)F(t) \rangle e^{-i\omega t} dt \end{aligned} \quad \text{Equation 42}$$

The mathematical form of the spectral density function $J(\omega)$ is determined by the actual motional process. For isotropic diffusion, $C(t)$ is an exponential decay function, and τ_c is the motional correlation time (Equation 43).

$$C(t) = \langle B_{loc}^2 \rangle e^{-t/\tau_c} \quad \text{Equation 43}$$

The derivation for spin-lattice relaxation time T_1 can be expanded to describe the spin-spin relaxation time T_2 of water proton influenced by superparamagnetic MNP, since both relaxations are of spin $\frac{1}{2}$ and caused by fluctuating dipolar interaction. Their difference is that, the DC of the former is between the nuclear magnetic moment of protons, while the latter is between the proton's nuclear magnetic moment, and the MNP's global magnetic moment, contributed by the exchange interaction, the Zeeman coupling, and the anisotropy energy. A superparamagnetic MNP has a

strong coupling between electronic spins, and its global magnetic moment is the total electronic magnetic moment of all the electrons in the crystal. Thus, the relaxation mechanism of water proton with MNP can be modeled based on the outer sphere theory, describing the effect of the interaction of the magnetic moment of a proton (I) with the magnetic moment of unpaired electrons (S), as derived in Equation 44 [170][171][172].

$$\begin{aligned}
R_2 = \frac{1}{T_2} = & \frac{1}{8} \int_{-\infty}^{+\infty} C(t) [\langle S_- S_+(t) \rangle e^{i\omega_I t} + \langle S_+ S_-(t) \rangle e^{-i\omega_I t}] dt \\
& + \frac{3}{4} \int_{-\infty}^{+\infty} C(t) [\langle S_- S_+(t) \rangle + \langle S_+ S_-(t) \rangle] dt \\
& + \frac{3}{4} \int_{-\infty}^{+\infty} C(t) [\langle S_+ S_-(t) \rangle e^{i\omega_I t} + \langle S_- S_+(t) \rangle e^{-i\omega_I t}] dt \\
& + 2 \int_{-\infty}^{+\infty} C(t) \langle S_z S_z(t) \rangle dt \\
& + \frac{3}{2} \int_{-\infty}^{+\infty} C(t) \langle S_z S_z(t) \rangle e^{-i\omega_I t} dt
\end{aligned} \tag{Equation 44}$$

where ω_I is the Larmor frequency of the proton, $C(t)$ is the autocorrelation of the spin position function, $F(t)$, as defined in Equation 45 and Equation 46, just like the case of proton dipole interaction as derived previously.

$$C(t) = \frac{3}{4} \hbar^2 \gamma_S^2 \gamma_I^2 \langle F(0)F(t) \rangle \tag{Equation 45}$$

$$F(t) = -\frac{[3\cos^2\theta(t) - 1]}{r(t)^3} \quad \text{Equation 46}$$

And $S_+ = \frac{1}{2}S_x - \frac{1}{2}iS_y$ and $S_- = \frac{1}{2}S_x + \frac{1}{2}iS_y$ are the raising and lowering operators of the Hamiltonian by quantum mechanics. $\langle S_-S_+(t) \rangle$ and $\langle S_+S_-(t) \rangle$ are the transverse spin-spin correlation functions and $\langle S_zS_z(t) \rangle$ is the longitudinal spin-spin correlation function. Superparamagnetic MNPs have very large anisotropy energy. They align with the external magnetic field, or the longitudinal axis. The contribution by longitudinal spin-spin correlation to relaxation is the square of the magnitude by the transverse correlation. Hence, the first three terms of the R_2 equation regarding transverse effect could be neglected with respect to the last two terms for longitudinal effect, and hence is simplified as Equation 47,

$$R_2 = 2 \int_{-\infty}^{+\infty} C(t) \langle S_zS_z(t) \rangle dt + \frac{3}{2} \int_{-\infty}^{+\infty} C(t) \langle S_zS_z(t) \rangle e^{-i\omega_1 t} dt \quad \text{Equation 47}$$

The relaxation rate [172], is obtained by solving the simplified equation above, which is in a general form similar to the T_1 proton 1/2 spin case, but with more complexity describing the additional fluctuating dipole interaction with a MNP, as derived in Equation 48.

$$\begin{aligned}
R_2 = & \left(\frac{32\pi}{135000} \right) \hbar^2 \gamma_S^2 \gamma_I^2 \left(\frac{N_A C}{RD} \right) \left\{ \left[\frac{3}{2} J^F(\omega_I, \tau_D, \tau_N) \right. \right. \\
& \left. \left. + 2J^F(0, \tau_D, \tau_N) \right] \Delta S_z^2 \right. \\
& \left. + \left[\frac{3}{2} J^A(\sqrt{2\omega_I \tau_D}) + 2J^A(0) \right] \langle S_z \rangle^2 \right\}
\end{aligned} \tag{Equation 48}$$

where C is the MNP concentration. γ_S is the electron gyromagnetic ratio. γ_I is the proton gyromagnetic ratio. N_A is the Avogadro constant. R is the effective radius of the MNP. And D is the water diffusion coefficient.

J^F is Freed's spectral density function, which takes into account for both the proton diffusion and the fluctuation of the magnetic moment around its mean value [173]. It is defined as shown in Equation 49.

$$J^F(\omega_I, \tau_D, \tau_N) = Re \left[\frac{1 + \Omega^{1/2}/4}{1 + \Omega^{1/2} + 4\Omega/9 + \Omega^{3/2}/9} \right] \tag{Equation 49}$$

where $\Omega = i\omega_I \tau_D + \tau_D/\tau_N$, $\tau_D = R^2/D$ is the characteristic diffusion time, and τ_N is the Neel relaxation time of the MNP.

J^A is Ayant's spectral density function accounting for the proton diffusion in a nonuniform magnetic field created by the mean electronic magnetic moment of the superparamagnetic MNP [174]. It is defined as Equation 50, as shown below.

$$J^A(z) = \frac{1 + 5z/8 + z^2/8}{1 + z + z^2/2 + z^3/6 + 4z^4/81 + z^5/81 + z^6/648} \quad \text{Equation 50}$$

The R_2 equation above could be rewritten in terms of magnetic moment μ by substituting $S = \mu/\gamma$. Accordingly, S_z becomes μ_z , which is μ projected on the axis of the external magnetic field, B_0 .

In this way, the R_2 equation is better related to the actual physical mechanism. The first term by $\Delta\mu_z^2$ represents the relaxation induced by the fluctuating part of μ , or $\Delta\mu_z$. The second term by $\langle\mu_z\rangle^2$ describes the effect caused by the diffusion related mechanism. Hence, R_2 can be derived as Equation 51 [172].

$$R_2 = \left(\frac{32\pi}{135000}\right) \hbar^2 \gamma_I^2 \left(\frac{N_A C}{RD}\right) \left\{ \left[\frac{3}{2} J^F(\omega_I, \tau_D, \tau_N) + 2J^F(0, \tau_D, \tau_N) \right] \Delta\mu_z^2 + \left[\frac{3}{2} J^A(\sqrt{2\omega_I \tau_D}) + 2J^A(0) \right] \langle\mu_z\rangle^2 \right\} \quad \text{Equation 51}$$

In a high external magnetic field, the MNPs' magnetic vectors are fixed along the B_0 direction. Although the local fields of the MNPs are quite strong, their temporal variations in magnitudes are relatively small. Hence, the Curie relaxation dominates: the first term by $\Delta\mu_z^2$ can be neglected with respect to the second term by $\langle\mu_z\rangle^2$. Consider a simple example for solid system, Equation 52,

$$\Delta\mu_z^2 = \langle\mu_z^2\rangle - \langle\mu_z\rangle^2 = \mu^2 \left(\frac{1}{\xi^2} - \frac{1}{\sinh(\xi)^2} \right) \quad \text{Equation 52}$$

where $\langle\mu_z\rangle^2 = \mu^2 \tanh(\xi)^2$, which is the expectation value of the magnetization μ , derived based on Curie's law [175]. For our superparamagnetic MNP and NMR biosensor with the saturated magnetization of 38 emu/g and $B_0 = 0.5$ T, then $\xi = \mu B_0 / kT = 148.9$ at $T = 300$ K. Finally, we obtained the ratio of $\frac{\langle\mu_z\rangle^2}{\Delta\mu_z^2} = 2.2 \times 10^4$. Thus, the effect by $\Delta\mu_z^2$ is considerably insignificant compared to that of $\langle\mu_z\rangle^2$.

Finally, the spin-spin relaxation of water proton with superparamagnetic MNP in the liquid system are derived and simplified as shown in the Equation 53.

$$R_2 = 1/T_2 = C \left(\frac{32\pi}{135000} \right) \hbar^2 \gamma_I^2 \left(\frac{N_A}{RD} \right) \left[\frac{3}{2} J^A(\sqrt{2\omega_I \tau_D}) + 2J^A(0) \right] \langle\mu_z\rangle^2 \quad \text{Equation 53}$$

The MNPs effectively induce nonuniformity of the NMR magnetic field in the sample, and hence enhance transverse magnetization dephasing and relaxation signal decay. The relaxation time T_2 , is inversely proportional to the concentration of the MNP, C in linear relationship. With unique superparamagnetic MNPs synthesized for strong magnetization, antibody-MNP functionalization and conjugation methods to label the target pathogen, we developed a new portable MNP-NMR biosensor system in this graduate research, which could be used to detect the target pathogen of different concentrations in water or food samples.

5.2.10 Detection of pNMR Relaxation Time

The pNMR selects a palm-sized permanent magnet of 0.5 Tesla to facilitate portable application. However, compared to the bulky conventional super-conducting magnet, it has trade-offs in magnetic field homogeneity and is challenging to implement a shim coil inside its limited internal space. Hence, the CPMG spin-echo technology is applied in the pNMR system to treat the less homogenous field. First, as with the free induction decay detection, the CPMG starts with an RF pulse applied to the sample ($90^\circ B_1$ pulse) to rotate the magnetic dipole 90° from the field direction of the magnet (Figure 5.18). This results in the net magnetization being in the x-y plane or the transverse plane, leading to the maximum signal during the NMR relaxation. However, in an inhomogeneous field, as determined by Equation 28, magnetic dipoles in different locations will have different Larmor frequencies, precessing at different speeds, which causes the dipoles de-phasing and get out of step with each other in the transverse plane. This leads to a rapid decay of the total magnetization vector after the 90° pulse is turned off, which causes the NMR signal to decay too quickly, faster than the real spin-spin relaxation, T_2 . The CPMG method mitigates this problem by applying a $180^\circ B_1$ pulse after waiting for the magnetization to decay away, at time τ following the 90° pulse [151]. The $180^\circ B_1$ pulse reverses the direction of the magnetic dipoles, causing them to change from de-phasing to refocusing and eventually come back to step with each other. This will lead to a signal peak at time 2τ (a spin-echo), revealing the actual peak as it were induced by T_2 relaxation in a homogeneous field.

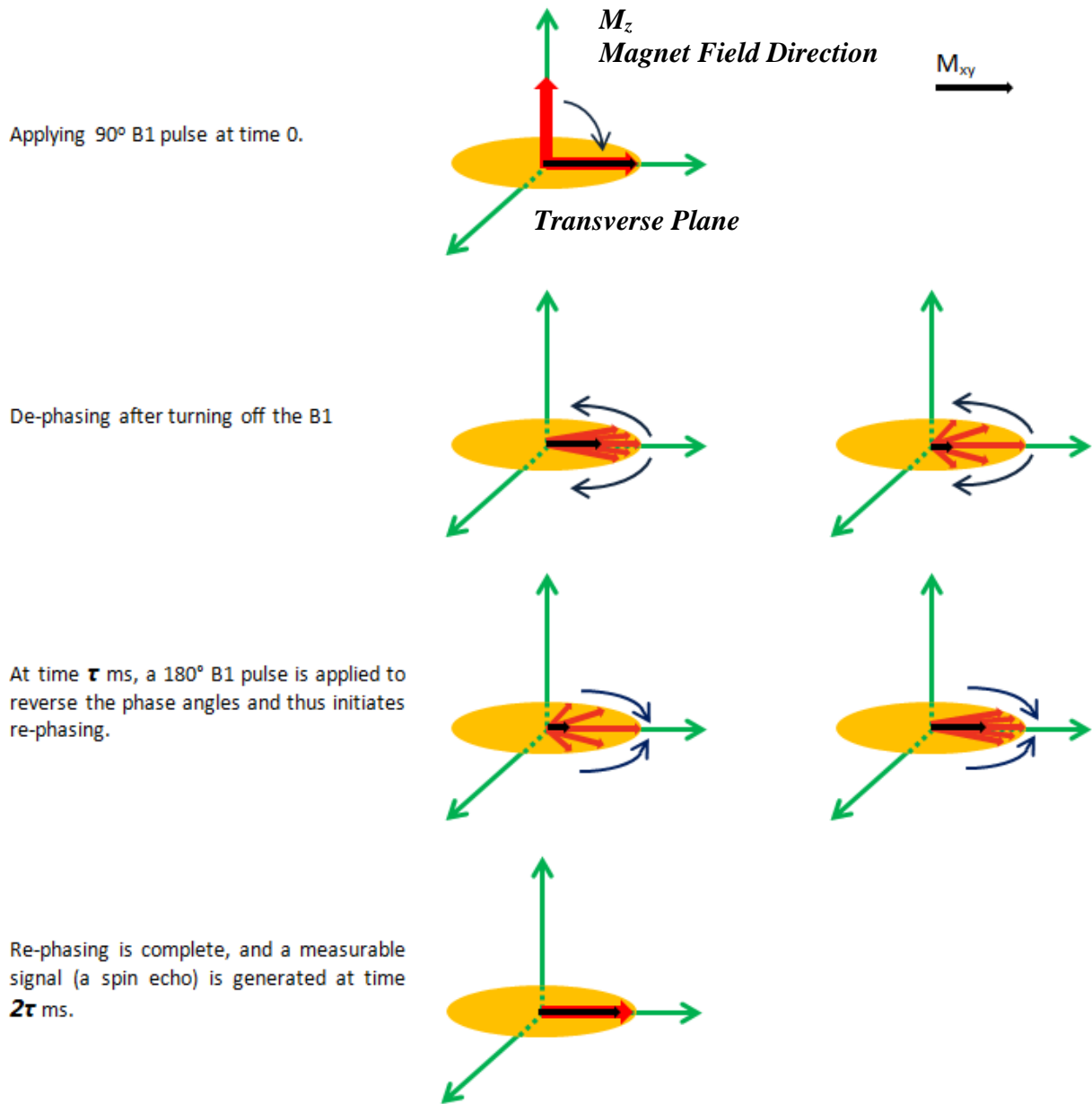


Figure 5.18 NMR spin-echo technique to treat the inhomogeneous field of a small permanent magnet using 90 degree and 180 degree RF pulse trains. (adapted and modified from [176])

Based on Equation 23, the 180° B_1 pulse can be achieved by applying the same oscillating transverse magnetic field to the coil for a duration twice long as the 90° B_1 pulse. After the peak, the signal will start to decay rapidly, corresponding to magnetic dipoles' de-phasing again. The

solution to this is to apply multiple 180° pulses with intervals all equal in the time space, every 2τ , as shown in Figure 5.19.

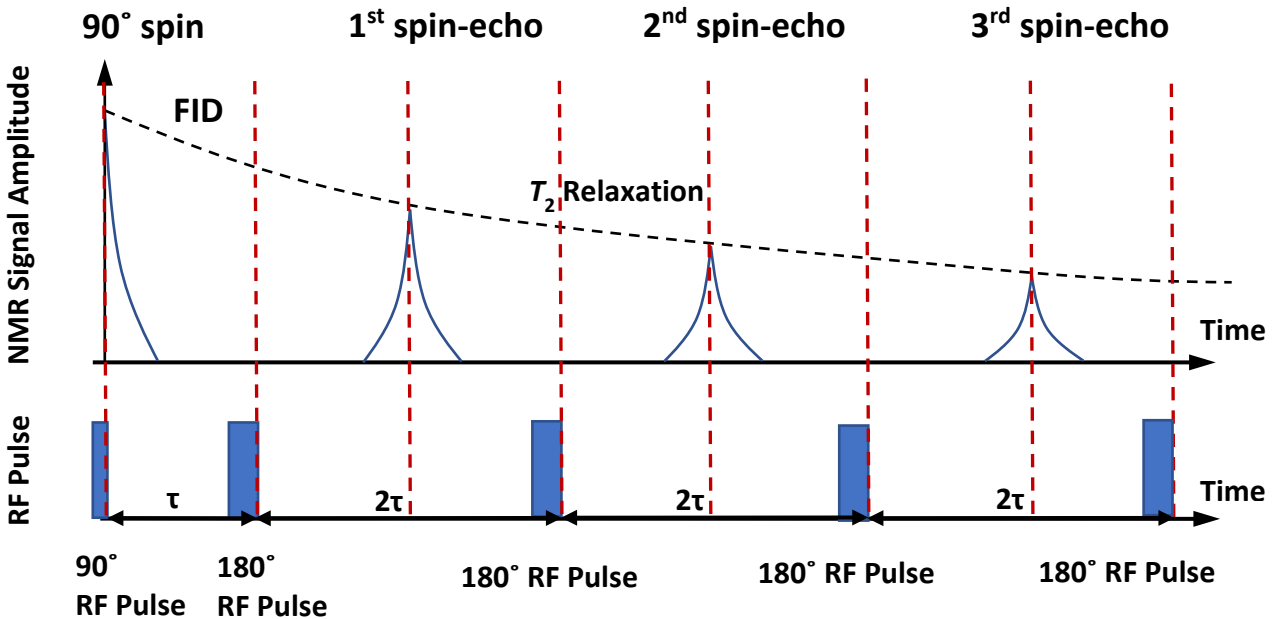


Figure 5.19 NMR spin-echo technique and CPMG pulse sequence to detect the spin-spin relaxation time, T_2 in a less homogeneous magnetic field.

As shown in Figure 5.1, a VHDL software was implemented at 300 MHz operation speed on a Xilinx Spartan-3 FPGA controller based on state machine to control the output switching of the power amplifier to generate the CPMG sequence. The pulse frequency is determined by the magnet field strength (0.5 Tesla) and proton's gyromagnetic ratio, as 19.918 MHz. During the pulse-on time, the power amplifier is turned on to amplify at full power for the 19.918 MHz pulse generated by the FPGA. During the pulse off time, the power amplifier was turned off to minimize noise interference to the receiver. The frequency, timing, width, duty cycle, and sequencing of pulse train were tested and verified using an oscilloscope. Through the free induction decay experiment on the pNMR system, the pulse widths of the 90° pulse and 180° pulse were tuned to be 7 μ sec and

14 μsec , respectively and the pulse interval, τ , was optimized to be 1.2 msec. The source code of the FPGA pulse control software is provided in Appendix A.

5.2.11 Test Pathogen and Antibodies

Escherichia coli O157:H7 was obtained from the collection of the Nano-Biosensors Laboratory at Michigan State University. *E. coli* O157:H7 test strains were inoculated using a sterile loop into 10 mL of Tryptic soy nutrient broth from Difco Laboratories (Detroit, MI) and incubated for 24 h at 37 °C to make a stock culture. The stock culture was then serially diluted in 0.1% peptone water in logarithmic scale to obtain different concentrations. All the experiments were performed in a certified Biological Safety Level II laboratory. The antibody used for NMR biosensor was purified mouse anti-*E. coli* O157:H7 monoclonal antibody (Meridian Life Science, Inc. Saco, ME).

5.2.12 Magnetic Pathogen Separation

Before pathogen conjugation, the antibody-MNP conjugates were filtered by 0.22 μm syringe filter (Millipore, MA, USA) to remove large particles. Then, 50 μL of antibody- MNP conjugates and 50 μL of pathogen sample dilution were mixed in 400 μL of 0.01M PBS. For negative control (blank sample), 50 μl of 0.1% (w/v) peptone water was used instead of pathogen sample dilution. The solution was incubated at 25 °C at 60 rpm for 30 minutes for MNP-pathogen conjugation [82][177]. To enhance NMR sensitivity, the incubated solution was filtered using a 0.45 μm syringe filter (Millipore, MA, USA) to remove impurities and unbound MNPs. The syringe filter's pore size was determined to be as large as possible (0.45 μm) in order to ensure all the unbound particles can flow through but keep blocking all the target bacteria. After a wash process using 0.01M PBS for 3 times, the syringe filter was backflushed using 5 mL of 0.01M PBS to release

the MNP-pathogen conjugates for further test using NMR. During separation, wash, and back-flush process, strong-field magnet was used to attract the MNPs in solution in order to facilitate the separation of unbound MNPs, hold the MNP-pathogen conjugates during washing, and help elute the MNP labeled pathogen, respectively. The filter based magnetic separation process is illustrated in Figure 5.20.

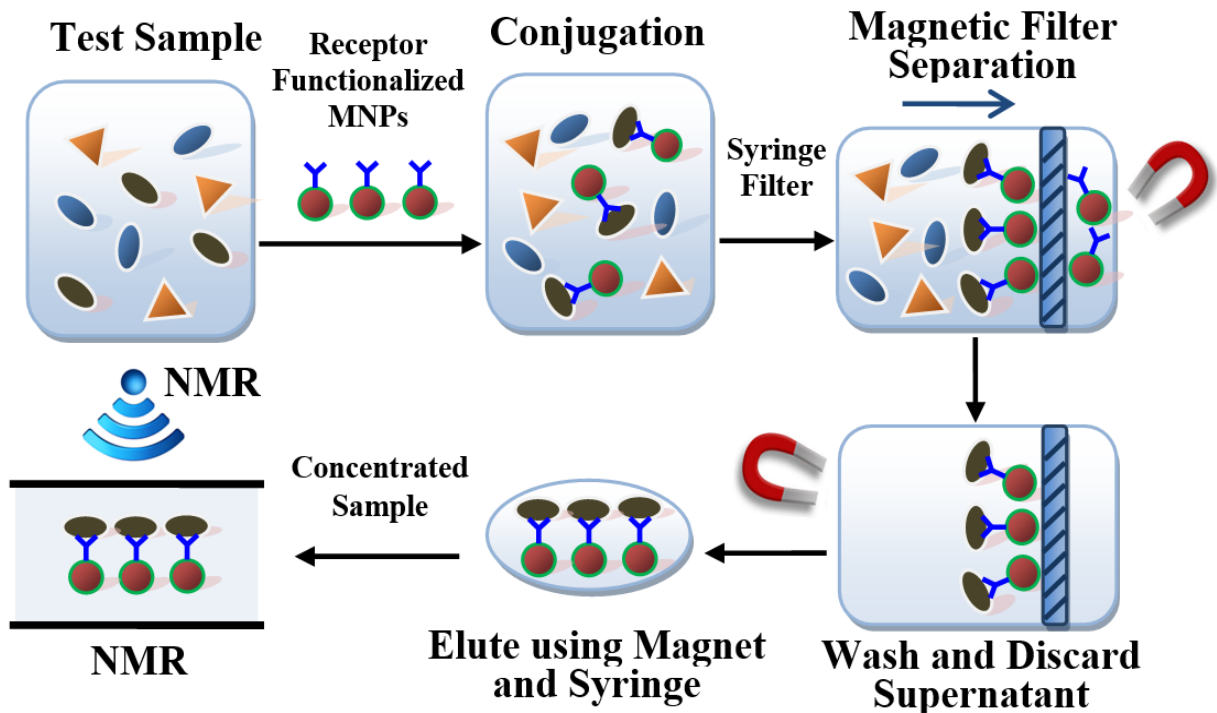


Figure 5.20 Working principle of the NMR based biosensor for pathogen detection

5.2.13 Sensor Architecture and Detection Principle

After the filter based magnetic separation process, the interference of unbound MNPs was effectively reduced, and MNPs in the eluted solution were proportional to the pathogen concentration. As paramagnetic material, the MNPs induced spatial and temporal disturbance in

the homogeneity and strength of the local magnetic field (Figure 5.21). Due to the high surface area to volume ratio, this disturbance introduced precession frequency variations in millions of protons of the surrounding water molecules, which accelerated the decay of the spin system's phase coherence. It was earlier shown that the MNP's concentration has a linear relationship to the water proton's spin-spin relaxation time, T_2 [178]. Therefore, the concentration of target pathogen in test solution could be measured from T_2 signal using the portable NMR biosensor.

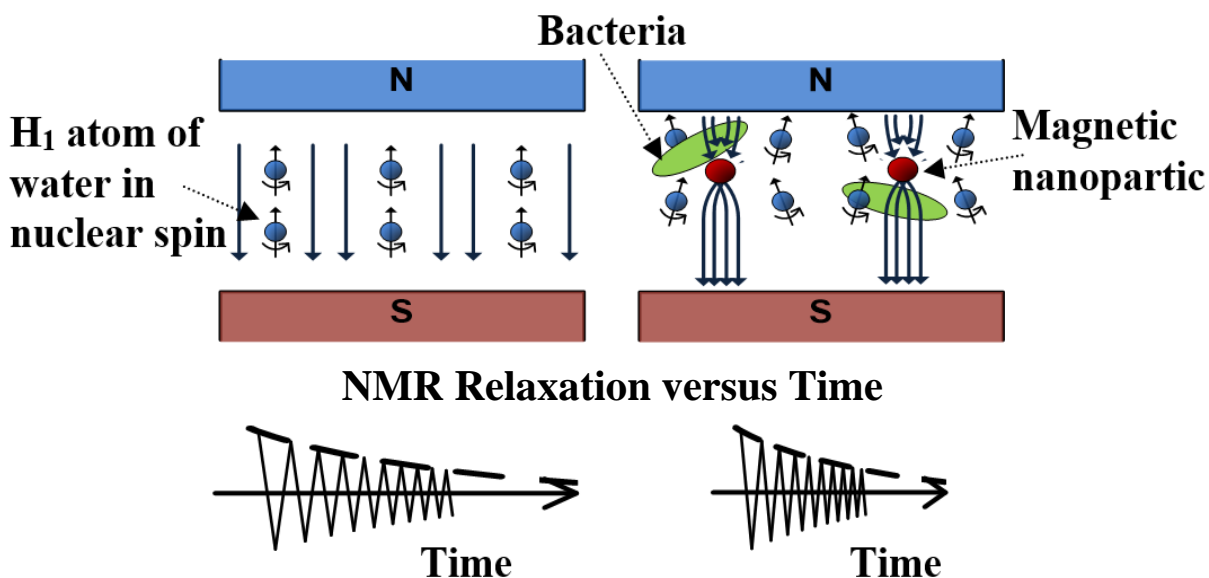


Figure 5.21 Magnetic nanoparticles as biomarker to detect the target pathogen by the NMR measurement.

5.2.14 Detection and Data Analysis

The NMR biosensor signal was measured using a digital oscilloscope: Model Agilent DSO1024A (Agilent Technologies, Santa Clara, CA) the connected to the NMR's signal output using BNC cable. For the biosensor test, a volume of 180 μL of the test solution by immunomagnetic

separation was applied to the biosensor. The NMR spin-echo relaxation signal was recorded by the oscilloscope, which is controlled by FPGA synchronization signal. The whole process of NMR relaxation was less than one minute. For data analysis, a minimum of three replications were performed for each experiment. All biosensors were calibrated using a control sample which consisted of immunomagnetic-separated solution prepared using the same test solution but without the pathogen. Standard deviations and mean values for the data of each experiment were calculated using Excel.

5.3 Results and Discussion

5.3.1 Functionalization of Magnetic Nanoparticles with Antibody

The magnetic nanoparticles used in pNMR biosensor are synthesized from amine functionalized Fe₂O₃ magnetic nanoparticle. The particle synthesis was described in Chapter 3. The MNPs were evaluated using transmission electron microscopy (TEM) and electron diffraction measurement. As indicated in the TEM image in Figure 5.22, the MNPs have spherical shape with a uniform average size of 80 nm and a total distribution between 50 to 100 nm [167]. The MNPs' crystalline nature is confirmed from the electron diffraction rings as demonstrated in the inset of Figure 5.22. As confirmed earlier by M-H hysteresis measurement [167], the MNP (1:0.6)'s saturation magnetization, M_s, was found to be 38 emu/g at room temperature. The MNPs' measured coercivity (H_c) was measured to be the same as the unfunctionalized Fe₂O₃ MNPs, 180 Oe, indicating that its anisotropy magnetic energy was not affected by the polyaniline nano-shell functionalization.

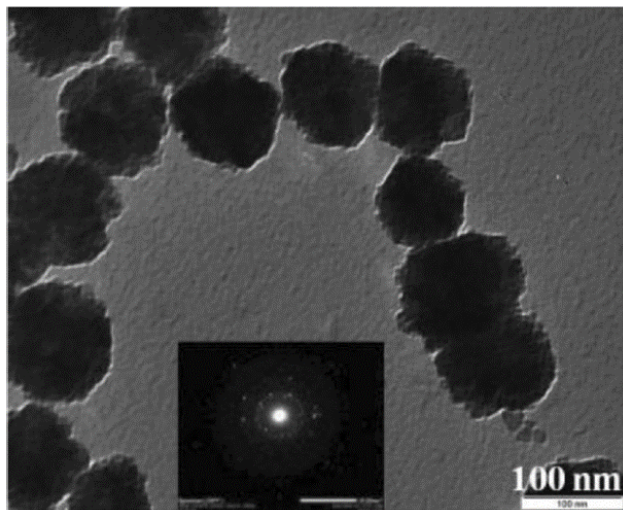


Figure 5.22 TEM image and electron diffraction image (inset) of the MNPs.

5.3.2 MNP Antibody Functionalization

Pathogen-specific antibodies were functionalized onto MNPs by physical non-covalent adsorption. The Ab-MNP conjugation is mainly formed by electrostatic interaction between the negatively charged Fc portion of the antibodies and the positively charged polyaniline surface, along with other factors, including hydrophobic effect, electrostatic interaction, hydrogen bonding, and van der Waals interaction [167][179]. The successful functionalization was confirmed by spectrophotometric studies earlier by our research team [167]. From measurement using UV-VIS scanning spectrophotometer, pure antibody solution had a characteristic wavelength peak of protein molecules at 280 nm. After the functionalization process with three times of magnetic separation, the supernatant solution had no peak at 280 nm, indicating that the antibodies were conjugated onto the MNPs effectively.

5.3.3 NMR R_2 Relaxation Time

Using the designed pNMR system, the target pathogen can be quantitatively detected through measuring NMR spin-spin relaxation time of water in the sample, which is inversely proportional to the amount of captured MNPs, as described in Chapter 5.2.8.

To detect the concentration of the target pathogen, the NMR biosensor measures each test sample for the spin-spin relaxation time, T_2 of water proton. First, the pNMR transmits high-power RF excitation signal through the coil antenna to the test sample, which align the magnetic moment of water proton inside. During the relaxation process back to thermal equilibrium, energy was emitted as RF echo signals and detected by the coil antenna. The echo series have exponential decay characteristics, which can be modeled in Equation 54.

$$M(t) = M_0 e^{-\frac{t}{T_2}} \quad \text{Equation 54}$$

where M is the nuclear spin magnetization vector as a function of time, t , M_0 is the initial nuclear spin magnetization vector, and T_2 is the spin-spin relaxation time constant.

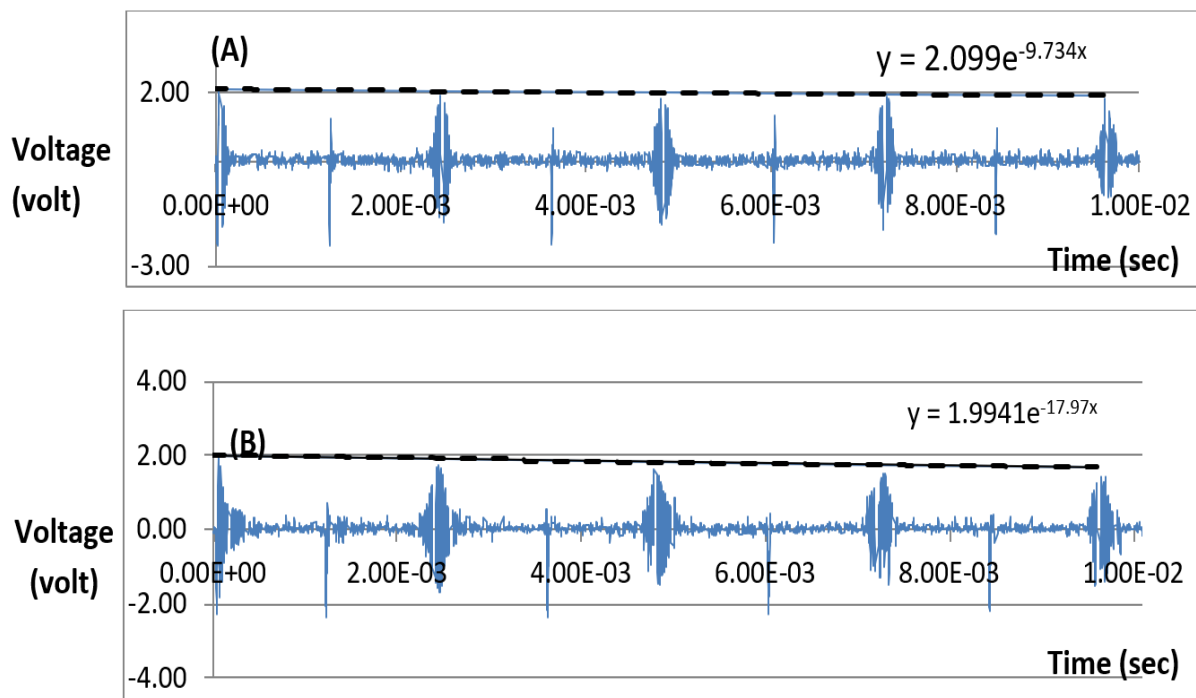


Figure 5.23 NMR biosensor relaxation signal of detection: (A) control (blank) sample, and (B) bacterial sample

The relaxation time T_2 is calculated by curve fitting of the signal envelope of the NMR echo series. For example, two NMR relaxation signals for pathogen sample and control sample are presented in Figure 5.23. Figure 5.23 (B) is the NMR signal of a sample spiked with *E. coli* O157:H7 while Figure 5.23 (A) is the NMR signal of a sample with no bacteria (blank). In this particular test, the spiked sample had a plate-counted bacterial concentration of 226 CFU/mL. The curve fitting results are shown as dashed lines in Figure 5.23 with the corresponding equations are shown above. The envelope curve fitting of the bacteria sample in Figure 5.23 (B) resulted mathematically in the Equation 55. Based on Equation 54, the time constant T_2 is $1/17.79$, which equals to 0.0556 s or 55.6 ms.

$$y = 1.994 e^{-17.97x} \quad \text{Equation 55}$$

For the control (blank) sample (0 CFU/mL), the envelope curve fitting of Figure 5.23A resulted in the Equation 56.

$$y = 2.099 e^{-9.734x} \quad \text{Equation 56}$$

The control sample consists of the same composition solution with the same amount of MNPs but without bacteria. It has a T_2 relaxation time of $1/9.734$, which equals to 0.1027 s or 102.7 ms (Figure 5.23B). The T_2 time of the bacteria sample is 54.1% (55.6/102.7) shorter than the control sample. These data demonstrate that the NMR signal decays faster in contaminated samples than in samples with no bacteria due to the formation of magnetic clusters around the bacterial cell walls and correspondingly reducing the bulk spin-spin relaxation time of the nearby water molecules. The magnetic filtration process removes the excessive unconjugated MNPs. This results in the captured MNPs being proportional to the target bacterial concentration. This improves the NMR sensitivity when detecting samples with low bacterial concentration as its composition is close to the blank sample.

Whole milk and drinking water and were used in the experiment to represent food samples. Milk and water were artificially inoculated with *E. coli* O157:H7 of concentration ranging from 10^1 to 10^7 CFU/mL. Magnetic filtration and NMR detection followed the same procedure as described above. The pNMR biosensor results are measured being delta T_2 of whole milk and drinking water samples are shown in Figure 5.24 and Figure 5.25. The curve fitting of signal envelope was processed for each experiment and T_2 was calculated as described above. The sample average and variance of the delta T_2 values, $T_{2 \text{ Control}} - T_{2 \text{ Sample}}$, were plotted for the bacteria contaminated and control samples. At least three replicates were performed for each test sample. Figure 5.24 and

Figure 5.25 indicate that the relaxation times of all the bacteria contaminated samples are shorter than that of the control samples. For drinking water and milk samples, the delta T_2 (Figure 5.24 and Figure 5.25) increases linearly with bacterial concentration from 10^1 CFU/mL up to 10^4 CFU/mL. The associated P-values for test results of water and milk samples were calculated and summarized in Table 5.5 and Table 5.6, respectively. The increase in T_2 difference between the control and contaminated samples supports the formation of MNPs clusters conjugated with the target bacteria, resulting in a change in their nearby magnetic field, and affecting the nuclear spin of the proton atoms of the surrounding water molecules. The pNMR relaxation difference does not further increase when the bacterial concentration is 10^5 CFU/mL or higher. This effect could be attributed to several factors. First, in the case of high bacterial concentrations, the outer bacteria could form one or several layers of blocking shells to the inner MNPs and hence reduce their impacts on the NMR relaxation due to their large size differences. MNPs are of around 80 nm diameter while *E. coli* O157:H7 is approximately 0.5 μm in width by 2 μm in length. In addition, the biochemical reaction of MNP-bacteria conjugation could be decreased due to the probabilistic interactions between the bacteria and antibodies, antibody orientations on MNP surface, and stability of the bacteria-MNPs conjugates complex. Further, there could be insufficient amount of Ab-MNPs to capture all the bacteria in the sample, similar to a saturation effect. In fact, data show that the pNMR signals for bacterial concentration of 10^5 to 10^7 CFU/mL do not have much difference compared to the pNMR signal of 10^4 CFU/mL.

NMR Biosensor Results

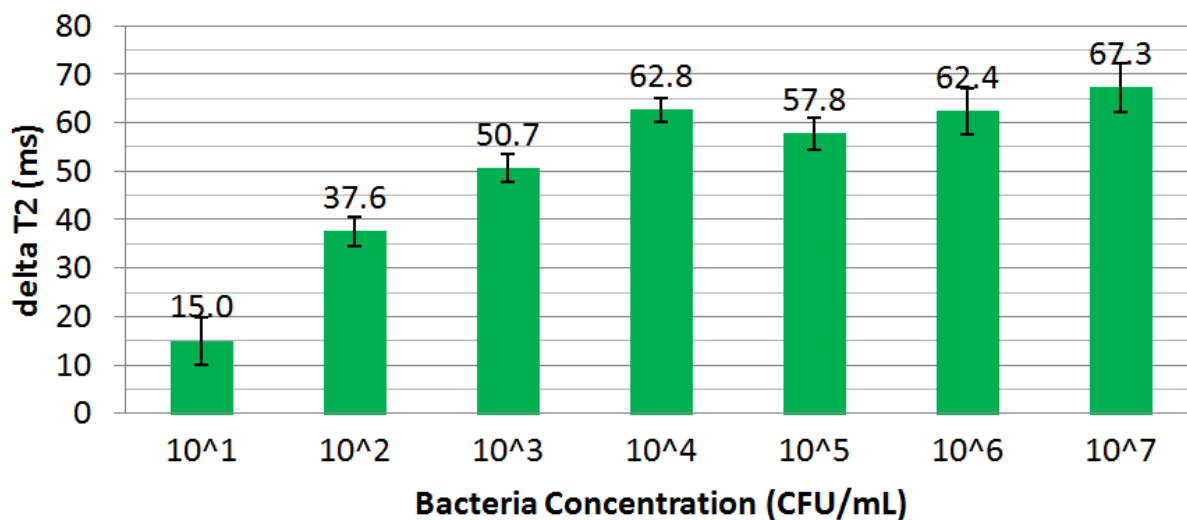


Figure 5.24 The MNP-based pNMR biosensor's measurement of relaxation time change, delta T_2 , for drinking water, which were contaminated by *E. coli* O157:H7.

Table 5.5 P-value of NMR biosensor test results for *E. coli* O157:H7 in water samples

Sample Pair (CFU/mL)	P-value (n = 3)
10 ¹ vs 10 ²	0.012
10 ² vs 10 ³	0.013
10 ³ vs 10 ⁴	0.012
10 ⁴ vs. 10 ⁵	0.156
10 ⁵ vs. 10 ⁶	0.312
10 ⁶ vs. 10 ⁷	0.377

The pNMR biosensor results for the whole milk samples are comparable to that of the drinking water samples, as demonstrated in Figure 5.25. The magnetic filtration assay has basically cleaned the sample matrix and removed excessive unbound MNPs. In general, the lowest detection limit

for milk and drinking water are down to the order of 10^1 CFU/mL or specifically, 92 CFU/mL and 76 CFU/mL for milk and water, respectively ($p < 0.05$, $n = 3$). Bacteria can be detected with concentration from 10^1 CFU/mL to 10^7 CFU/mL.

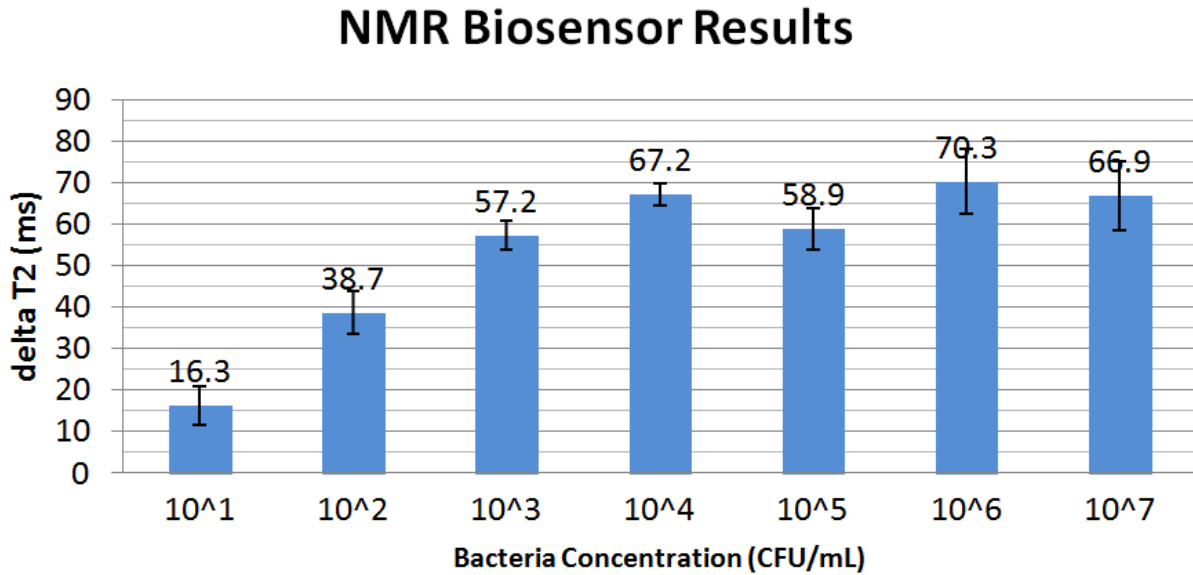


Figure 5.25 The MNP-based pNMR biosensor's measurement of relaxation time change, ΔT_2 , for whole milk samples, which were contaminated by *E. coli* O157:H7 .

Table 5.6 P-value of NMR biosensor test results for *E. coli* O157:H7 in milk samples

Sample Pair (CFU/mL)	P-value (n = 3)
10^1 vs 10^2	0.010
10^2 vs 10^3	0.024
10^3 vs 10^4	0.031
10^4 vs. 10^5	0.131
10^5 vs. 10^6	0.185
10^6 vs. 10^7	0.698

The pNMR biosensor's wide detection range is highly beneficial to food safety since certain organisms have varied infectious doses. For example, studies have shown that the infectious dose for some *Shigella* spp. is less than 10 organisms while that of toxigenic *V. cholera* is 10^4 organisms, which has one thousand times of difference [180]. The infective dose for another toxigenic pathogen, *Salmonella* is 10^3 organisms [181]. Results from the pNMR biosensor indicates that its detection sensitivity is better than those in the existing literature. A chip-NMR biosensor designed by Lee et al. has a detection sensitivity of 10^3 CFU/mL for *Staphylococcus aureus* [140]. This level of detection limit is consistent with our results when magnetic filtration is not applied, which is 10^3 CFU/mL for *E. coli* O157:H7.

5.4 Conclusions

This chapter describes a novel integrated design of an NMR biosensor, which make use of antibody-functionalized magnetic nanoparticle and filter based magnetic separation. The detection of the biosensor systems is fast, which includes a magnetic filtration assay of 20 min followed by a signal detection of 1 min. The average sensing limit for water and milk is 84 CFU/mL, lower than other NMR biosensors reported in the literature. The linear range of the NMR biosensor is from 10^1 to 10^4 CFU/mL while the detection range spans from 10^1 CFU/mL to 10^7 CFU/mL. The detection application can be extended to other microbial or viral organisms by appropriate adaption for their corresponding antibodies. Hence, besides food safety application, the NMR biosensor described in this research has potential to be applied as rapid detection devices in food safety, biodefense, and clinical diagnostics.

This chapter is adapted from our recently published work in the Journal of Biological Engineering:

Yilun Luo, and Evangelyn C. Alocilja. Portable Nuclear Magnetic Resonance Biosensor and Assay for a Highly Sensitive and Rapid Detection of Foodborne Bacteria in Complex Matrices. *Journal of Biological Engineering*. 2017. 11(14).

DOI: [10.1186/s13036-017-0053-8](https://doi.org/10.1186/s13036-017-0053-8)

CHAPTER 6

CONCLUSION AND FUTURE WORK

6.1 Conclusions

In this dissertation, two biosensors based on nanofiber and nanoparticle NMR, respectively, were successfully developed to detect *E. coli* O157:H7 bacteria in culture and in food samples. The work described in this dissertation also incorporated electrospinning technology and nanofiber surface treatment as well as NMR probe and transceiver design to improve their system performance for biosensing applications.

The first research work in the dissertation focused on an electrospun nanofiber biosensor. A new type of electrospun nanofibrous membrane (ENM) was successfully synthesized for capillary flow assay (LFA) application. Conductive MNPs were synthesized and functionalized with antibody to be the biomarker and applied in magnetic separation for sample filtration. A novel LFA biosensor was developed using the ENM and the MNP. The ENM was optimized for capillary action and pathogen binding by improved fiber alignment, plasma treatment, and antibody conjugation. Owing to the unique nanostructure and higher surface area of ENM and MNP, the biosensor was capable of detecting *E. coli* O157:H7 from a 10^1 CFU/mL sample with linear response from 10^1 to 10^4 CFU/mL. The versatility of this biosensor was also evaluated. It was capable of detecting BVDV from a 10^3 CCID/mL sample, equivalent to 1/1000 of viral concentration in infected bovine blood serum. The detection process was fast, detection time of 15 min from lateral flow process to data acquisition. Its application can be easily extended to detect other microbial or viral organisms

by appropriately changing the antibodies. This low-cost and simple measurement biosensor makes it possible for rapid field testing in food supply and healthcare.

The second research work reported in this dissertation is a portable NMR biosensor. MNPs were synthesized and functionalized with antibodies for NMR biosensing. The research combined an NMR system design for high signal-to-noise ratio and a unique filtration assay to improve sensitivity. The versatility of the biosensor was evaluated on both water and dairy food samples. The sample testing was rapid, including a magnetic filtration assay of 20-30 min followed by a detection time of 1 min. The averaged detection limit on water and milk samples was 84 CFU/mL, lower than the other NMR biosensors reported in the existing literature. The biosensor was highly portable and sensitive in detection with linear response from 10^1 to 10^4 CFU/mL while total range from 10^1 to 10^7 CFU/mL. The biosensing application can be easily extended to detect other microbial or viral pathogens by adaption for the corresponding antibodies. Thus, in addition to food safety application, the NMR biosensor has demonstrated promising potential to be applied for rapid detection in healthcare diagnostics and biodefense.

In summary, the electropun- and pNMR- biosensors developed in this research have demonstrated sensitive detection performance and rapid response compared to conventional *E. coli* detection methods. Both of them can be used as a low cost and portable diagnosis system for on-field food and water testing, and be extended to detect other bacterial and viral pathogens.

6.2 Recommendations for Future Work

Future work is recommended towards a number of research activities. For the electrospun biosensor, further improvement in the electrospinning process may be possible to increase the consistency in fiber alignment. Software algorithm to automatically process the impedance data is beneficial to further reduce detection time. Fellows et al. developed an LFA to detect glycoprotein CD4 [41]. Zheng et al. developed an immunosensor to detect β -Trophin protein [43]. Shi et al. developed a portable LFA biosensor to detect neomycin (NEO) and quinolones antibiotics (QNS) [44]. It is possible to implement the electrospun biosensor to detect other analytes, such as protein or IgG. Since the EFM has demonstrated a promising potential in biosensing, it is possible to explore the feasibility of applying for another biosensor platform.

For the pNMR biosensor, the magnetic field strength of the low-cost and small magnet shifts due to temperature variation, which can cause variance in the NMR result during on-field testing. Possible temperature regulator can be applied to keep the system temperature suitable. It is also possible to implement a dynamic NMR frequency control to compensate the temperature effect on the NMR signal [182]. To further improve portability, all the NMR components can be installed into a single instrument enclosure. Lu et al. utilized microfluidic channels for sample transport, detection, and removal in NMR detection [59]. It is possible to integrate such device in the pNMR system to automate the detection process. Gossuin et al. found that large magnetic field is beneficial to NMR detection [58]. Janis et al. utilized a 1.5 Tesla Halbach magnet for proton prepolarization [60]. Other small, high field strength, and low-cost magnets can be evaluated for this biosensor, such as the Halbach array magnet, to exploit the possibility to further increase detection limit, reduce cost, and system size.

APPENDIX

APPENDIX

This section contains the software source code in VHDL programming language on the FPGA controller for the CPMG pulse control.

```
-----  
-- nmr_biosensorw_cpmg_main.vhd  
-----
```

```
-- Author: Yilun Luo  
--       Biosensors Lab, Michigan State University  
-----
```

```
-- Description:   This file tests the included UART component by  
--               sending data in serial form through the UART to  
--               change it to parallel form, and then sending the  
--               resultant data back through the UART to determine if  
--               the signal is corrupted or not. When the serial  
--               information is converted into parallel information,  
--               the data byte is displayed on the 8 LEDs on the  
--               system board.  
--  
-----
```

```
-- Revision History:  
--       03/30/11 (LYL) Created  
--       05/20/11 (LYL) Added a finite state machine (FSM) for CPMG pulse generation  
-----
```

```
library IEEE;  
use IEEE.STD_LOGIC_1164.ALL;  
--use IEEE.STD_LOGIC_ARITH.ALL;
```

```

use IEEE.STD_LOGIC_UNSIGNED.ALL;
--use IEEE.numeric_bit.all;          -----YL
use IEEE.numeric_std.all;

```

```

-----
-- Title:      Main entity
--
-- Inputs:     3      :      RXD, CLK, RST
--
-- Outputs:    1      :      TXD, LEDS
--
-- Description: This describes the main entity that tests the included
--              UART component.  The LEDS signals are used to
--              display the data byte on the LEDs, so it is set equal to
--              the dbOutSig.  Technically, the dbOutSig is the scan code
--              backwards, which explains why the LEDs are mapped
--              backwards to the dbOutSig.
-----

```

entity DataCntrl is

```

    Port ( TXD          : out std_logic := '1';
           RXD          : in  std_logic := '1';
           CLK          : in  std_logic;
           LEDS         : out std_logic_vector(7 downto 0) := "11111111";
           RST          : in  std_logic := '0';

```

```

-----YL-----
           EnLED        : out bit_vector(3 downto 0);
           EnDigit      : out bit_vector(6 downto 0);
           DISPLAY      : in  std_logic;
           PulsOut      : out std_logic := '0';

```

```

    BtnPuls          : in std_logic := '0';
    PULSRESET       : in std_logic := '0';
    SwSel            : in std_logic_vector(3 downto 0);
    DeblankOut      : out std_logic := '0';

```

-----YL-----

```
end DataCntrl;
```

architecture Behavioral of DataCntrl is

```
-- Local Component, Type, and Signal declarations.
```

```
component RS232RefComp
```

```

Port (
    TXD  : out  std_logic      := '1';
    RXD  : in   std_logic;
    CLK  : in   std_logic;
    DBIN : in   std_logic_vector (7 downto 0);
    DBOU : out  std_logic_vector (7 downto 0);
    RDA  : inout std_logic;
    TBE  : inout std_logic      := '1';
    RD   : in   std_logic;
    WR   : in   std_logic;
    PE   : out  std_logic;
    FE   : out  std_logic;
    OE   : out  std_logic;

    RST  : in   std_logic      := '0'

```

```
);
```

```
end component;
```

```

-----YL-----
component BCDHEXDisplay is
Port (
    BINBCD: in std_logic; --0 for binary 1 for BCD
    BinNum: in bit_vector( 3 downto 0);
    DecNum: in integer;
    LEDIndex : in integer;
    LED: out bit_vector(3 downto 0);
    Digit: out bit_vector( 6 downto 0)
);
end component;

```

```

component LEDDisplayTiming is
Port
(
    LEDCLK:    in std_logic;
    EN:        in std_logic;
    DATALED:  in bit_vector(15 downto 0);
    BINBCD:    out std_logic;
    LEDINDX:   out integer range 0 to 5;
    LEDNUM:    out bit_vector(3 downto 0)
);
end component;

```

```

component Clock_Divider
port
(
    CIN : in STD_LOGIC;
    TIMECONST1: in integer;
    COUT: out STD_LOGIC
);

```

```
end component;
```

```
-- Debounce circuit for Key
```

```
COMPONENT debounce
```

```
  PORT ( clk, key  : IN STD_LOGIC;
```

```
         pulse    : OUT STD_LOGIC);
```

```
END COMPONENT;
```

```
COMPONENT P_GENERATOR
```

```
  PORT(
```

```
        CLK : IN std_logic;
```

```
--        CLKMS : IN std_logic;
```

```
        RESET : IN std_logic;
```

```
        TRIG : IN std_logic;
```

```
        PULSE : OUT std_logic;
```

```
        Deblank : OUT std_logic;
```

```
        WIDTH_A : in integer range 0 to 9999;
```

```
        WIDTH_B : in integer range 0 to 999025;
```

```
        WIDTH_C : in integer range 0 to 9999;
```

```
--        WIDTH_D : in integer range 0 to 63
```

```
        WIDTH_D : in integer range 0 to 127
```

```
    );
```

```
END COMPONENT;
```

```
-----YL-----
```

```
-----
```

```
--
```

```
-- Title:      Type Declarations
```

```
--
```

```
-- Description: There is one state machine used in this program, called
```

```
--      the mainState state machine. This state machine controls
--      the flow of data around the UART; allowing for data to be
--      changed from serial to parallel, and then back to serial.
--
```

```
-----
type mainState is (
    stReceive,
    stSend);
-----
```

```
-----YL-----
type HFBYTE is array (0 to 3) of std_logic_vector(3 downto 0);
-----YL-----
```

```
-----
-- Title: Local Signal Declarations
--
```

```
-- Description: The signals used by this entity are described below:
--
```

```
--      -dbInSig      :      This signal is the parallel data input for the UART
--      -dbOutSig     :      This signal is the parallel data output for the UART
--      -rdaSig       :      This signal will get the RDA signal from the UART
--      -tbeSig       :      This signal will get the TBE signal from the UART
--      -rdSig        :      This signal is the RD signal for the UART
--      -wrSig        :      This signal is the WR signal for the UART
--      -peSig        :      This signal will get the PE signal from the UART
--      -feSig        :      This signal will get the FE signal from the UART
--      -oeSig        :      This signal will get the OE signal from the UART
--
```

```
--      The following signals are used by the main state machine for state control:
```

```

--
--          -stCur, stNext
--
-----

    signal dbInSig :      std_logic_vector(7 downto 0);
    signal dbOutSig:      std_logic_vector(7 downto 0);
    signal rdaSig  :      std_logic;
    signal tbeSig  :      std_logic;
    signal rdSig   :      std_logic;
    signal wrSig   :      std_logic;
    signal peSig   :      std_logic;
    signal feSig   :      std_logic;
    signal oeSig   :      std_logic;

    signal stCur  :      mainState := stReceive;
    signal stNext  :      mainState;

-----YL-----

--Signals for LED display
    signal LEDCLK: std_logic;
    signal LEDINDX: integer range 0 to 4:= 0;
    signal LEDNUM: bit_vector (3 downto 0);
    signal BINBCD: std_logic:= '0';
    signal ENDISPLAY: std_logic:= '1';
    signal DATALED: bit_vector (15 downto 0);
    signal HEXIN: integer range 0 to 16:=0;
--signal CLKDIV: integer range 0 to 10000000:=0;
    signal startPuls: std_logic:= '0';
    signal DEBCLK: std_logic;
--    signal PULSCLK: std_logic;
--signal PulsCount: std_logic_vector (4 downto 0);

```

```

----signal PulsCount: integer range 0 to 100000000;
    signal index: integer range 0 to 3 :=0;
    signal PulsWidthA: HFBYTE;
    signal PulsWidthB: HFBYTE;
    signal PulsWidthC: HFBYTE;

    signal PulsTimeA: integer range 0 to 9999;
    signal PulsTimeB: integer range 0 to 999025;
    signal PulsTimeC: integer range 0 to 9999;
--    signal PulsTimeD: integer range 0 to 63           := 5;           --Interval number of
the longer pulse.
--    signal PulsTimeD: integer range 0 to 63           := 40;          --051112
    signal PulsTimeD: integer range 0 to 127           := 80;          --080312

```

-----YL-----

-- Module Implementation

begin

--

--Title: LED definitions

--

```

--    LEDS(7) <= dbOutSig(0);
--    LEDS(6) <= dbOutSig(1);
--    LEDS(5) <= dbOutSig(2);
--    LEDS(4) <= dbOutSig(3);
--    LEDS(3) <= dbOutSig(4);

```

```
-- LEDS(2) <= dbOutSig(5);
-- LEDS(1) <= dbOutSig(6);
-- LEDS(0) <= dbOutSig(7);
```

```
-----
UART: RS232RefComp port map ( TXD      => TXD,
                               RXD      => RXD,
                               CLK      => CLK,
                               DBIN     => dbInSig,
                               DBOUT    => dbOutSig,
                               RDA      => rdaSig,
                               TBE     => tbeSig,
                               RD       => rdSig,
                               WR       => wrSig,
                               PE       => peSig,
                               FE       => feSig,
                               OE       => oeSig,
                               RST     => RST);
-----
```

-----YL-----

```
L2:  BCDHEXDisplay port map (BINBCD,LEDNUM,HEXIN,LEDINDX,EnLED,EnDigit);
```

```
D1:  LEDDisplayTiming port map
(LEDCLK,ENDISPLAY,DATALED,BINBCD,LEDINDX,LEDNUM);
```

```
-- Set countdown
```

```
DebPuls:  Debounce port map (DEBCLK, BtnPuls, startPuls);
```

```
G1:  Clock_Divider port map (CLK,100,LEDCLK);
```

```
--2.5kHz. 10000 -> 400us
```

```
G2:  Clock_Divider port map (CLK,10000,DEBCLK);
```

```

--1MHz
--G3: Clock_Divider port map (CLK,25,PULSCLK);

--      Inst_P_GENERATOR: P_GENERATOR PORT MAP(
--          CLK => CLK,
--          CLKMS => PULSCLK,
--          RESET => PULSRESET,
--          TRIG => StartPuls,
--          PULSE => PulsOut,
--          Deblank => DeblankOut
--      );
Inst_P_GENERATOR: P_GENERATOR PORT
MAP(CLK,PULSRESET,StartPuls,PulsOut,DeblankOut,PulsTimeA,PulsTimeB,PulsTimeC,Pul
sTimeD);

----DeblankOut <= StartPuls;
-----YL-----
-----
--
-- Title: Main State Machine controller (UART)
--
-- Description: This process takes care of the Main state machine
--              movement. It causes the next state to be evaluated on
--              each rising edge of CLK. If the RST signal is strobed,
--              the state is changed to the default starting state, which
--              is stReceive.
--
-----

      process (CLK, RST)
          begin

```

```

        if (CLK = '1' and CLK'Event) then
            if RST = '1' then
                stCur <= stReceive;
            else
                stCur <= stNext;
            end if;
        end if;
    end process;

```

```

-----
--
-- Title: Main State Machine (UART)
--
-- Description: This process defines the next state logic for the Main
--              state machine. The main state machine controls the data
--              flow for this testing program in order to send and
--              receive data.
--

```

```

-----
    process (stCur, rdaSig, dboutsig)
        begin
            case stCur is

```

```

-----
--
-- Title: stReceive state
--
-- Description: This state waits for the UART to receive data. While in
--              this state, the rdSig and wrSig are held low to keep the
--              UART from transmitting any data. Once the rdaSig is set
--              high, data has been received, and is safe to transmit. At

```

```
--      this time, the stSend state is loaded, and the dbOutSig
--      is copied to the dbInSig in order to transmit the newly
--      acquired parallel information.
```

```
--
```

```
-----
```

```
      when stReceive =>
```

```
          rdSig <= '0';
```

```
          wrSig <= '0';
```

```
      if rdaSig = '1' then
```

```
          --DATALED(7 downto 0) <= to_bitvector(dbOutSig(7 downto 0));
```

```
---YL---
```

```
          dbInSig <= dbOutSig;
```

```
          stNext <= stSend;
```

```
      else
```

```
          stNext <= stReceive;
```

```
      end if;
```

```
-----
```

```
--
```

```
-- Title: stSend state
```

```
--
```

```
-- Description: This state tells the UART to send the parallel
```

```
--      information found in dbInSig. It does this by strobing
```

```
--      both the rdSig and wrSig signals high. Once these
```

```
--      signals have been strobed high, the stReceive state is
```

```
--      loaded.
```

```
--
```

```
-----
```

```
      when stSend =>
```

```
          rdSig <= '1';
```

```

        wrSig <= '1';
        stNext <= stReceive;
    end case;
end process;

-----YL-----
--   p1: process (rdaSig)
--       begin
--           if (rdaSig'event and rdaSig = '1') then
--
--               if (Sw(7) = '1') then
--
--                   if (dbOutSig(7 downto 0)/="00001101") then
--
--                       ---YL: 'enter'
--
--                           case Command(15 downto ) is
--                               when "001" =>
--                                   PulsWidthA(index) <= dbOutSig(3
downto 0);
--                               when "010" =>
--                                   PulsWidthB(index) <= dbOutSig(3
downto 0);
--                               when "100" =>
--                                   PulsWidthC(index) <= dbOutSig(3
downto 0);
--                               when others =>
--                                   end case;
--                                   index <= index + 1;
--
--                                   LEADS(3 downto 0) <= std_logic_vector(
to_unsigned( index, 4));
--                                   DATALED(11 downto 8) <= "0101";

```

```

--                                --DATALED(7 downto 0) <= bit_vector(
to_unsigned( index, 8));
--                                else
--                                LEDS(3 downto 0) <= std_logic_vector(
to_unsigned( index, 4));
--                                --DATALED(11 downto 8) <= "0111";
--
--                                DATALED(3 downto 0) <=
to_bitvector(PulsWidth(0));
--                                DATALED(7 downto 4) <=
to_bitvector(PulsWidth(1));
--                                DATALED(11 downto 8) <=
to_bitvector(PulsWidth(2));
--                                DATALED(15 downto 12) <=
to_bitvector(PulsWidth(3));
--
--                                index <= 0;
--                                end if;
--                                else
--                                end if;
--                                end process p1;

```

-----YL-----

```

p1: process (rdaSig)
    begin
        if (rdaSig'event and rdaSig = '1') then

            if (SwSel(3) = '1') then
--                if (dbOutSig(7 downto 0)/="00001101") then          ---YL: 'enter'

```

```

case SwSel(2 downto 0) is
  when "001" =>
    PulsWidthA(index) <= dbOutSig(3 downto 0);
  when "010" =>
    PulsWidthB(index) <= dbOutSig(3 downto 0);
  when "100" =>
    PulsWidthC(index) <= dbOutSig(3 downto 0);
  when others =>
    PulsWidthA(index) <= PulsWidthA(index);
    PulsWidthB(index) <= PulsWidthB(index);
    PulsWidthC(index) <= PulsWidthC(index);
end case;

index <= index + 1;

LEDS(3 downto 0) <= std_logic_vector( to_unsigned( index, 4));
LEDS(7 downto 4) <= "0101";
--DATALED(7 downto 0) <= bit_vector( to_unsigned( index, 8));
else
  case SwSel(2 downto 0) is
    when "001" =>
      DATALED(3 downto 0) <=
to_bitvector(PulsWidthA(3));
      DATALED(7 downto 4) <=
to_bitvector(PulsWidthA(2));
      DATALED(11 downto 8) <=
to_bitvector(PulsWidthA(1));
      DATALED(15 downto 12) <=
to_bitvector(PulsWidthA(0));

```

```

--PulsTimeA <= 875 + to_integer(
unsigned(PulsWidthA(3))+to_integer( unsigned(PulsWidthA(2)))*10+to_integer(
unsigned(PulsWidthA(1))*100+to_integer( unsigned(PulsWidthA(0))*1000;
PulsTimeA <= 805 + to_integer(
unsigned(PulsWidthA(3))+to_integer( unsigned(PulsWidthA(2)))*10+to_integer(
unsigned(PulsWidthA(1))*100+to_integer( unsigned(PulsWidthA(0))*1000;
when "010" =>
DATALED(3 downto 0) <=
to_bitvector(PulsWidthB(3));
DATALED(7 downto 4) <=
to_bitvector(PulsWidthB(2));
DATALED(11 downto 8) <=
to_bitvector(PulsWidthB(1));
DATALED(15 downto 12) <=
to_bitvector(PulsWidthB(0));
--PulsTimeB <= to_integer(
unsigned(PulsWidthB(3))+to_integer( unsigned(PulsWidthB(2)))*10+to_integer(
unsigned(PulsWidthB(1))*100+to_integer( unsigned(PulsWidthB(0))*1000;
--PulsTimeB <= - 875 + to_integer(
unsigned(PulsWidthB(3))*100+to_integer( unsigned(PulsWidthB(2)))*1000+to_integer(
unsigned(PulsWidthB(1))*10000+to_integer( unsigned(PulsWidthB(0))*100000;
PulsTimeB <= - 805 + to_integer(
unsigned(PulsWidthB(3))*100+to_integer( unsigned(PulsWidthB(2)))*1000+to_integer(
unsigned(PulsWidthB(1))*10000+to_integer( unsigned(PulsWidthB(0))*100000;
when "100" =>
DATALED(3 downto 0) <=
to_bitvector(PulsWidthC(3));
DATALED(7 downto 4) <=
to_bitvector(PulsWidthC(2));
DATALED(11 downto 8) <=
to_bitvector(PulsWidthC(1));

```

```

DATALED(15 downto 12) <=
to_bitvector(PulsWidthC(0));

--PulsTimeC <= 875 + to_integer(
unsigned(PulsWidthC(3))+to_integer( unsigned(PulsWidthC(2)))*10+to_integer(
unsigned(PulsWidthC(1))*100+to_integer( unsigned(PulsWidthC(0)))*1000;
PulsTimeC <= 805 + to_integer(
unsigned(PulsWidthC(3))+to_integer( unsigned(PulsWidthC(2)))*10+to_integer(
unsigned(PulsWidthC(1))*100+to_integer( unsigned(PulsWidthC(0)))*1000;
when others =>
PulsTimeA <= PulsTimeA;
PulsTimeB <= PulsTimeB;
PulsTimeC <= PulsTimeC;
end case;

index <= 0;

LEDS(3 downto 0) <= std_logic_vector( to_unsigned( index, 4));
LEDS(7 downto 4) <= "0111";

end if;

end if;

end process p1;

-----YL-----
-- PulsOut <= startPuls; -----YL: Debug Probe-----
-- PulsOut <= rdaSig;
-----YL-----
-----YL-----

```

```

-- PULS: process(CLK, CLKMS, startPuls)
--
--     begin
--     if (startPuls'event and startPuls = '0') then
--         genPuls <= '1';
--     end if;
--
--     if (genPuls = '0') then
--         PulsCountA <= 0;
--         PulsCountB <= 0;
--         PulsCountC <= 0;
--     elsif (CLK = '1' and CLK'Event) then
--         If (PulsCount /= 25) then
--             If (PulsCount /= (PulsTimeA+PulsTimeC)) then
--                 PulsCount <= PulsCount + 1;
--             end if;
--         --end if;
--     elsif (CLKMS = '1' and CLKMS'Event) then
--         If (PulsCountB /= (PulsTimeB)) then
--             PulsCountB <= PulsCountB + 1;
--         end if;
--     end if;
--
--     if (startPuls = '1' and PulsCount < 24 ) then
--     if (startPuls = '1') then
--         if PulsCount<(PulsTimeA-1) then
--             PulsOut <= '1';
--         elsif PulsCount<(PulsTimeA+PulsTimeB-1) then
--             PulsOut <= '0';
--         elsif PulsCount<(PulsTimeA+PulsTimeB+PulsTimeC-1) then
--             PulsOut <= '1';

```

```
--          else
--          PulsOut <= '0';
--          end if;
--      else
--          PulsOut <= '0';
--      end if;
--
--      end process;
-----YL-----

end Behavioral;
```

BIBLIOGRAPHY

BIBLIOGRAPHY

- [1] Atnafie B, Paulos D, Abera M, Tefera G, Hailu D, Kasaye S, Amenu K. Occurrence of Escherichia coli O157:H7 in cattle feces and contamination of carcass and various contact surfaces in abattoir and butcher shops of Hawassa, Ethiopia. BMC Microbiol. 2017 Jan 25;17(1):24.
- [2] Erickson MC, Liao JY, Payton AS, Cook PW, Ortega YR. Survival and internalization of Salmonella and Escherichia coli O157:H7 sprayed onto different cabbage cultivars during cultivation in growth chambers. J. Sci. Food Agric. 2019 May;99(7):3530-3537.
- [3] Pollari F, Christidis T, Pintar KDM, Nesbitt A, Farber J, Lavoie MC, Gill A, Kirsch P, Johnson RP. Evidence for the benefits of food chain interventions on E. coli O157:H7/NM prevalence in retail ground beef and human disease incidence: A success story. Can J Public Health. 2017 Apr 20;108(1):e71-e78.
- [4] Federal, R., *Quality standards for foods with no identity standards; bottled water*, F.a.D. Administration, Editor. 1993. p. 52042-52050.
- [5] Yakub, G.P., et al., *Evaluation of Colilert and Enterolert defined substrate methodology for wastewater applications*. Water Environment Research, 2002. **74**(2): p. 131-5.
- [6] Federal, R., *Guidelines establishing test procedures for the analysis of pollutants; analytical methods for the biological pollutants in wastewater and sewage sludge; final rule*. 2007. **72**(157): p. 14220-14233.
- [7] Fode-Vaughan, K.A., et al., *Direct PCR detection of Escherichia coli O157:H7*. Letters in Applied Microbiology, 2003. **37**(3): p. 239-43.
- [8] Torres-Chavolla, E. and E.C. Alocilja, *Nanoparticle based DNA biosensor for tuberculosis detection using thermophilic helicase-dependent isothermal amplification*. Biosensors & Bioelectronics, 2011. **26**(11): p. 4614-8.
- [9] Hill, H.D. and C.A. Mirkin, *The bio-barcode assay for the detection of protein and nucleic acid targets using DTT-induced ligand exchange*. Nature Protocols, 2006. **1**(1): p. 324-36.
- [10] Rompre, A., et al., *Detection and enumeration of coliforms in drinking water: current methods and emerging approaches*. Journal of Microbiological Methods, 2002. 49: p. 31-54.
- [11] Yanbo Liu, Ming Hao, Zhijun Chen, Lingling Liu, Yao Liu, Wenxiu Yang, Seeram Ramakrishna, "A review on recent advances in application of electrospun nanofiber materials as biosensors," *Current Opinion in Biomedical Engineering*, vol. 13, pp. 174-189, 2020.

- [12] Ye WW, Ding YT, Sun Y, et al.: A nanoporous alumina membrane based impedance biosensor for histamine detection with magnetic nanoparticles separation and amplification[J]. *Procedia Technol* 2017, 27:116–117.
- [13] Xie S, Tang Y, Tang D, et al. :Highly sensitive impedimetric biosensor for Hg(2+) detection based on manganese porphyrin-decorated DNA network for precipitation polymerization [J]. *Anal Chim Acta* 2018, 1023:22–28.
- [14] Chowdhury AD, Ganganboina AB, Park EY, et al.: Impedimetric biosensor for detection of cancer cells employing carbohydrate targeting ability of Concanavalin A[J]. *Biosens Bioelectron* 2018, 122:95–103.
- [15] WHO (2017). *Guidelines for drinking-water quality*, fourth edition. World Health Organization: ISBN: 978-92-4-154995-0, pp. 127, 240 - 241, 2017.
- [16] CDC (2020). "Reports of Selected E. coli Outbreak Investigations". Retrieved on 6 October 2020, from <https://www.cdc.gov/ecoli/outbreaks.html>
- [17] FDA (2020), "Spokane Produce Voluntarily Recalls Northwest Cuisine Creations and Fresh & Local Sandwiches and Green Leaf Lettuce Filets." Published on 11 March 2020, from <https://www.fda.gov/safety/recalls-market-withdrawals-safety-alerts/spokane-produce-voluntarily-recalls-northwest-cuisine-creations-and-fresh-local-sandwiches-and-green>
- [18] Carol Holtz, "Global Health Care: Issues and Policies." Jones & Bartlett Learning, pp. 239, May 20, 2016.
- [19] FDA (2020). *Bacteriological Analytical Manual (BAM)*, U.S. Food & Drug Administration: Chapter 4a: Diarrheagenic *Escherichia coli*; Appendix 1: Rapid Methods for Detecting Foodborne Pathogens, 2020.
- [20] *Guidelines for drinking-water quality: fourth edition incorporating the first addendum*. Geneva: World Health Organization; 2017. Licence: CC BY-NC-SA 3.0 IGO.
- [21] US National Institutes of Health (NIH), US National Institute of Allergy and Infectious Diseases (NIAID). Biodefense - NIAID Category A, B, and C Priority Pathogens website. Available: <http://www.niaid.nih.gov/topics/biodefenserelated/biodefense/pages/cata.aspx>. Accessed 2012 Oct 26.
- [22] CDC (2018). "Bioterrorism Agents/Diseases." Retrieved on 4 April 2018, from <https://emergency.cdc.gov/agent/agentlist-category.asp>
- [23] Sujakhu, K. and U.T. Shrestha, Microbial (Coliform and *Vibrio cholerae*) analysis of drinking water collected from outbreak region of Bhaktapur municipality. 2011.

- [24] CDC (2010). Microbiological Indicator Testing in Developing Countries: A Fact Sheet for the Field Practitioner. ver. 1 December 2010
<https://sanitationupdates.files.wordpress.com/2010/11/microbiology2020.pdf>
- [25] Bartram, Jamie, Ballance, Richard, World Health Organization & United Nations Environment Programme. (1996). Water quality monitoring: a practical guide to the design and implementation of freshwater quality studies and monitoring programs / edited by Jamie Bartram and Richard Ballance. London: E & FN Spon. pp. 229-241,
<https://apps.who.int/iris/handle/10665/41851>
- [26] Sauerbrey G. Verwendung von schwingquarzen zur wägung dünner schichten und zur mikrowägung. *Z. Phys.* 1959;155:206–222. doi: 10.1007/BF01337937.
- [27] Muratsugu M, Ohta F, Miya Y, Hosokawa T, Kurosawa S, Kamo N, Ikeda H, Quartz crystal microbalance for the detection of microgram quantities of human serum albumin: relationship between the frequency change and the mass of protein adsorbed. *Anal Chem.* 1993 Oct 15; 65(20):2933-7.
- [28] Deng T, Li JS, Wang H, Shen GL, Yu RQ, Piezoelectric immunoassay for complement C4 based on a Nafion-modified interface for antibody immobilization. *J Immunol Methods.* 2005 Apr; 299(1-2):1-8.
- [29] Funari R, Terracciano I, Della Ventura B, Ricci S, Cardi T, D'Agostino N, Velotta R, Label-Free Detection of Gliadin in Food by Quartz Crystal Microbalance-Based Immunosensor. *J Agric Food Chem.* 2017 Feb 15; 65(6):1281-1289.
- [30] Miroslav Pohanka, "Overview of Piezoelectric Biosensors, Immunosensors and DNA Sensors and Their Applications," *Materials*2018,11, 448; doi:10.3390/ma11030448
- [31] Il-Hoon Cho, Dong Hyung Kim, and Sangsoo Park, "Electrochemical biosensors: perspective on functional nanomaterials for on-site analysis," *Biomaterials Research* (2020) 24:6.
- [32] Zhu N, et al. Label-free and sequence-specific DNA detection down to a picomolar level with carbon nanotubes as support for probe DNA. *Anal Chim Acta.* 2009; 650: 44–8.
- [33] Han L, et al. Enhanced conductivity of rGO/Ag NPs composites for electrochemical immunoassay of prostate-specific antigen. *Biosens Bioelectron.* 2017; 87: 466–72.
- [34] Cai X, et al. Ratiometric electrochemical immunoassay based on internal reference value for reproducible and sensitive detection of tumor marker. *Biosens Bioelectron.* 2016;81:173–80.
- [35] Damborský, Pavel et al. "Optical biosensors." *Essays in biochemistry* vol. 60,1 (2016): 91-100. doi:10.1042/EBC20150010

- [36] Huang, J.; Virji, S.; Weiller, B. H.; Kaner, R. B., Polyaniline Nanofibers: Facile Synthesis and Chemical Sensors. *Journal of the American Chemical Society*, 2003, 125, (2), pp. 314-315.
- [37] Sánchez-Tirado, E.; Salvo, C.; González-Cortés, A.; Yáñez-Sedeño, P.; Langa, F.; Pingarrón, J. M. Electrochemical Immunosensor for Simultaneous Determination of Interleukin-1 Beta and Tumor Necrosis Factor Alpha in Serum and Saliva Using Dual Screen Printed Electrodes Modified with Functionalized Double-walled Carbon Nanotubes. *Anal. Chim. Acta* 2017, 959, 66–73.
- [38] Green, A. A.; Hersam, M. C. Properties and Application of Double-Walled Carbon Nanotubes Sorted by Outer-Wall Electronic Type. *ACS Nano* 2011, 5, 1459–1467.
- [39] Moore, K. E.; Flavel, B. S.; Ellis, A. V.; Shapter, J. G. Comparison of Double-Walled with Single-Walled Carbon Nanotube Electrodes by Electrochemistry. *Carbon* 2011, 49, 2639–2647.
- [40] Hou, L., Cui, Y., Xu, M., Gao, Z., Huang, J., Tang, D., "Graphene Oxide-Labeled Sandwich-Type Impedimetric Immunoassay with Sensitive Enhancement Based on Enzymatic 4-Chloro-1-Naphthol Oxidation," *Biosens. Bioelectron.* 2013, 47, 149–156.
- [41] Tamika Fellows, Lance Ho, Shane Flanagan, Ronen Fogel, Dupe Ojo, and Janice Limson, " Gold nanoparticle-streptavidin conjugates for rapid and efficient screening of aptamer function in lateral flow sensors using novel CD4-binding aptamers identified through Crossover-SELEX," *Analyst*, 2020, 145, 5180-5193
- [42] Qiu, W., Baryeh, K., Takalkar, S. *et al.* Carbon nanotube-based lateral flow immunoassay for ultrasensitive detection of proteins: application to the determination of IgG. *Microchim Acta* **186**, 436 (2019). <https://doi-org.proxy1.cl.msu.edu/10.1007/s00604-019-3508-4>
- [43] Zheng, L., Fang, C., Yan, J. *et al.* A New Tactic for Label-Free Recognition of β -Trophin via Electrochemiluminescent Signalling on an AuNPs Supported Immuno-Interface. *Sci Rep* **7**, 11199 (2017). <https://doi.org/10.1038/s41598-017-11750-8>
- [44] Shi, Q., Huang, J., Sun, Y. *et al.* A SERS-based multiple immuno-nanoprobe for ultrasensitive detection of neomycin and quinolone antibiotics via a lateral flow assay. *Microchim Acta* **185**, 84 (2018). <https://doi-org.proxy1.cl.msu.edu/10.1007/s00604-017-2556-x>
- [45] Gondhalekar, C., Biela, E., Rajwa, B. *et al.* Detection of *E. coli* labeled with metal-conjugated antibodies using lateral-flow assay and laser-induced breakdown spectroscopy. *Anal Bioanal Chem* **412**, 1291–1301 (2020). <https://doi-org.proxy1.cl.msu.edu/10.1007/s00216-019-02347-3>
- [46] Wiley: NMR Spectroscopy: Basic Principles, Concepts, and Applications in Chemistry, 2nd Edition - Harald Günther. [Online]. Available:

<http://www.wiley.com/WileyCDA/WileyTitle/productCd-047195201X.html>. [Accessed 14 Oct 2016].

- [47] Ng SM. Chapter 3 - Portable NMR-Based Sensors in Medical Diagnosis A2 - ur-Rahman, Atta. In *Applications of NMR Spectroscopy*, M. I. Choudhary, Ed. Bentham Science Publishers, 2015, pp. 121–146.
- [48] Yu D, Garcia N, Xu S. Toward portable nuclear magnetic resonance devices using atomic magnetometers. *Concepts Magn Reson Part A*. 2009;34A(2): 124–32.
- [49] Perez JM, Josephson L, O’Loughlin T, Högemann D, Weissleder R. Magnetic relaxation switches capable of sensing molecular interactions. *Nat Biotechnol*. 2002;20(8):816–20.
- [50] Lee H, Sun E, Ham D, Weissleder R. Chip–NMR biosensor for detection and molecular analysis of cells. *Nat Med*. 2008;14(8):869–74.
- [51] Rokitta M, Rommel E, Zimmermann U, Haase A. Portable nuclear magnetic resonance imaging system. *Rev Sci Instrum*. 2000;71(11):4257–62.
- [52] Lee H, Yoon T-J, Figueiredo J-L, Swirski FK, Weissleder R. Rapid detection and profiling of cancer cells in fine-needle aspirates. *Proc Natl Acad Sci*. 2009;106(30):12459–64.
- [53] Zalesskiy SS, Danieli E, Blümich B, Ananikov VP. Miniaturization of NMR Systems: Desktop Spectrometers, Microcoil Spectroscopy, and “NMR on a Chip” for Chemistry, Biochemistry, and Industry. *Chem Rev*. 2014;114(11): 5641–94.
- [54] Patel P. An NMR Chip The Size of a Seed. *IEEE Spectrum: Technology, Engineering, and Science News*, 05-Aug-2014. [Online]. Available: [http:// spectrum.ieee.org/tech-talk/biomedical/devices/an-nmr-device-the-size-of-aseed](http://spectrum.ieee.org/tech-talk/biomedical/devices/an-nmr-device-the-size-of-aseed). [Accessed 30 Sep 2016].
- [55] Sara Hash, M. Pilar Martinez-Viedma, Fred Fung, Jee Eun Han, Paul Yang, Charlene Wong, Loganathan Doraisamy, Suresh Menon, Donald Lightner, "Nuclear magnetic resonance biosensor for rapid detection of *Vibrio parahaemolyticus*," *Biomedical Journal*, Volume 42, Issue 3, 2019, Pages 187-192, ISSN 2319-4170, <https://doi.org/10.1016/j.bj.2019.01.009>.
- [56] Suresh M. Menon, David E. Newman, Terry J. Henderson, J. Manuel Perez, " Magnetic resonance system and method to detect and confirm analytes," U.S. patent, US9442110B2, Sept. 13, 2016
- [57] Gupta, M, Singh, K, Lobiyal, DK, et al. A sensitive on-chip probe-based portable nuclear magnetic resonance for detecting low parasitaemia plasmodium falciparum in human blood. *Med Devices Sens*. 2020; 3:e10098. <https://doi.org.proxy1.cl.msu.edu/10.1002/mds3.10098>

- [58] Gossuin, Y., Okusa Ndjolo, P., Vuong, Q.L. et al. NMR relaxation properties of the synthetic malaria pigment β -hematin. *Sci Rep* 7, 14557 (2017). <https://doi.org/10.1038/s41598-017-15238-3>
- [59] Lu, R., Lei, P., Yang, Q. *et al.* Development of a Microfluidic NMR Device for Rapid and Quantitative Detection of Tumor Markers. *Appl Magn Reson* **50**, 357–370 (2019). <https://doi.org/10.1007/s00723-018-1071-5>
- [60] Janis Smits, Joshua T. Damron, Pauli Kehayias, Andrew F. McDowell, Nazanin Mosavian, Ilya Fescenko, Nathaniel Ristoff, Abdelghani Laraoui, Andrey Jarmola, Victor M. Acosta, "Two-dimensional nuclear magnetic resonance spectroscopy with a microfluidic diamond quantum sensor," *Science Advances*, Vol. 5, no. 7, 26 Jul 2019: eaaw7895
- [61] Dengwei Jing, Le Sun, Jingyu Jin, Madasamy Thangamuthu and Junwang Tang, " Magneto-optical transmission in magnetic nanoparticle suspensions for different optical applications: a review," *Journal of Physics D: Applied Physics*, Vol.54, Num, 1, October 14 2020.
- [62] Kai Wu, Jinming Liu, Diqing Su, Renata Saha, and Jian-Ping Wang, "Magnetic Nanoparticle Relaxation Dynamics-Based Magnetic Particle Spectroscopy for Rapid and Wash-Free Molecular Sensing," *CS Appl. Mater. Interfaces* 2019, 11, 26, 22979–22986, Publication Date: June 6, 2019, <https://doi-org.proxy2.cl.msu.edu/10.1021/acsami.9b05233>
- [63] Ulrike Martens, Una Janke, Sophie Möller, Delphine Talbot, Ali Abou-Hassan, and Mihaela Delcea, " Interaction of fibrinogen–magnetic nanoparticle bioconjugates with integrin reconstituted into artificial membranes," *Nanoscale*, Vol. 12, Iss. 38, 09/2020, 19918-19930.
- [64] Kimberly Fabijanczuk, Kaylee Gaspar, Nikunj Desai, Jungeun Lee, Daniel A. Thomas, J. L. Beauchamp, and Jinshan Gao, " Resin and Magnetic Nanoparticle-Based Free Radical Probes for Glycan Capture, Isolation, and Structural Characterization," *Analytical Chemistry* **2019** 91 (24), 15387-15396, DOI: 10.1021/acs.analchem.9b01303
- [65] Shutyi, A.M., Eliseeva, S.V. & Sementsov, D.I. Responses of an Isolated Anisotropic Magnetic Nanoparticle and Nanoparticle Lattice to a Magnetic Field Pulse. *Appl Magn Reson* **51**, 409–429 (2020). <https://doi-org.proxy2.cl.msu.edu/10.1007/s00723-020-01193-2>
- [66] Pourmodheji H, Ghafar-Zadeh E, Magierowski S. A Multidisciplinary Approach to High Throughput Nuclear Magnetic Resonance Spectroscopy. *Sensors*. 2016;16 no. 6.
- [67] Lei K-M, Mak P-I, Law M-K, Martins RP. A palm-size μ NMR relaxometer using a digital microfluidic device and a semiconductor transceiver for chemical/biological diagnosis. *Analyst*. 2015;140(15):5129–37.

- [68] S. Kralj, M. Rojnik, Matija, J. Kos, D. Makovec (2013). "Targeting EGFR-overexpressed A431 cells with EGF-labeled silica-coated magnetic nanoparticles". *Journal of Nanoparticle Research* 15 (5), 1666, 1-11.
- [69] F. Gertz¹ and A. Khitun¹ (2016). "Biological cell manipulation by magnetic nanoparticles". *AIP Advances* 6, 025308, 1-7.
- [70] Y.S. Jiang, H. Wang, S.B. Li and W.J. Wen (2014). "Applications of Micro/Nanoparticles in Microfluidic Sensors: A Review". *Sensors*, 14, 6952-6964
- [71] I. Rabias, et al. (2010). "Rapid magnetic heating treatment by highly charged maghemite nanoparticles on Wistar rats exocranial glioma tumors at microliter volume". *Biomicrofluidics* 4(2): 024111 1-8.
- [72] H. Unterwegera, S. Lyera, R.P. Friedricha, C. Jankoa, M. Pöttlera, S. Dürrb, C. Alexioua (2015). "Magnetic nanoparticle-based drug delivery for cancer therapy". *Biochemical and Biophysical Research Communications*, Volume 468, Issue 3, Pages 463–470.
- [73] K.E. Scarberry, E.B. Dickerson, J.F. McDonald, Z.J. Zhang (2008). "Magnetic Nanoparticle-Peptide Conjugates for in Vitro and in Vivo Targeting and Extraction of Cancer Cells". *Journal of the American Chemical Society* 130 (31): 10258–62.
- [74] R. E. Elizabeth, J.P. Eric and E.S. Raymond (2013). "Magnetic separation of colloidal nanoparticle mixtures using a material specific peptide". *Chem. Commun.*, 2013, 49, 5471-5473.
- [75] Xiliang, L., et al., *Application of nanoparticles in electrochemical sensors and biosensors*. *Electroanalysis*, 2006. **18**(4): p. 319-326.
- [76] Chen Q., Lin J., Gan C., Wang Y., Wang D., Xiong Y., Lai W., Li Y., Wang M. (2015) "A sensitive impedance biosensor based on immunomagnetic separation and urease catalysis for rapid detection of *Listeria monocytogenes* using an immobilization-free interdigitated array microelectrode". *Biosens Bioelectron.* 74:504-11.
- [77] Pal, S., E.C. Alocilja, and F.P. Downes, (2007) *Nanowire labeled direct-charge transfer biosensor for detecting Bacillus species*. *Biosensors & Bioelectronics.* **22**(9-10): p. 2329-36.
- [78] A.-H. Lu, E. L. Salabas and F. Schüth (2007). "Magnetic Nanoparticles: Synthesis, Protection, Functionalization, and Application". *Angew. Chem. Int. Ed.* 46 (8): 1222–1244
- [79] S S.Rana, J. Philip, B.Raj (2010). "Micelle based synthesis of Cobalt Ferrite nanoparticles and its characterization using Fourier Transform Infrared Transmission Spectrometry and Thermogravimetry". *Materials Chemistry and Physics* 124: 264–269.

- [80] E. K. Athanassiou, Evagelos K.; R. N. Grass; W. J. Stark (2010). "Chemical Aerosol Engineering as a Novel Tool for Material Science: From Oxides to Salt and Metal Nanoparticles". *Aerosol. Sci. Tech.* 44 (2): 161–72.
- [81] Sharma, R., S. Lamba, et al. (2005). "Composition dependent magnetic properties of iron oxide-polyaniline nanoclusters." *Journal of Applied Physics* **97**(1): 014311-6.
- [82] Pal, S. and E. C. Alocilja (2009). "Electrically active polyaniline coated magnetic (EAPM) nanoparticle as novel transducer in biosensor for detection of Bacillus anthracis spores in food samples." *Biosensors and Bioelectronics* **24**(5): 1437-44.
- [83] Maghemite (2020), Retrieved 30 October 2020, from <https://en.wikipedia.org/wiki/Maghemite>.
- [84] K.S. Ryu, S.H. Chang, S.K. Jeong, E.J. Oh, and C.H. Yo. (2000). "Magnetic Properties of Conducting Polyanilines Induced by Organic Acids and Solvents". 238 *Bull. Korean Chem. Soc.*, Vol. 21, No. 2, 238-240
- [85] Barick, K. C., M. Aslam, et al. (2009). "Nanoscale assembly of amine-functionalized colloidal iron oxide." *Journal of Magnetism and Magnetic Materials* 321(10): 1529-1532.
- [86] Peter Dobson, Stephen King, Erik Gregersen, and Kara Rogers, "Nanoparticle," *Encyclopedia Britannica*, May 14, 2019, <https://www.britannica.com/science/nanoparticle>, Access November 30, 2020
- [87] Lin, Y.Y., Wang, J., Liu, G.D., Wu, H., Wai, C.M., Lin, Y.H., 2008. *Biosensors and Bioelectronics*. 23, 1659-1665.
- [88] Zhang, G.P., Wang, X.N., Yang, J.F., Yang, Y.Y., Xing, G.X., Li, Q.M., Zhao, D., Chai, S.J., Guo, J.Q., 2006. *Journal of Immunological Methods*. 312, 27-33.
- [89] Beck, O., Kraft, M., Moeller, M.R., Smith, B.L., Schneider, S., Wennig, R, 2000. *Ann Clin Biochem*. 37, 199-204.
- [90] Wong, R., Tse, H., 2008. *Lateral Flow Immunoassay*, first ed. Humana Press, New York, pp. 35-51.
- [91] Basu, M., Seggerson, S., Henshaw, J., Jiang, J., Cordona, R., Lefave, C., Boyle, P.J., Miller, A., Pugia, M., Basu, S., 2004. *Glycoconjugate Journal*. 21, 487-496.
- [92] Mehdinia, A., Kazemi, S.H., Bathaie, S. Z., Alizadeh, A., Shamsipur M., Mousavi, M.F., 2009. *Journal of Pharmaceutical and Biomedical Analysis*. 49, 587-593.
- [93] Claussen, J.C., Franklin A.D., Haque A.U., Porterfield, M.D., Fisher, T.S., 2009. *ACS Nano*. 3, 37–44.

- [94] Wang, X.Y., Drew, C., Lee, S. H., Senecal, K.J., Kumar, J., Samuelson, L.A., 2002. *Journal of Macromolecular Science*. A39, 1251-1258.
- [95] Huang, Z.M., Zhang, Y.Z., Kotaki, M., Ramakrishna, S., 2003. *Composites Science and Technology*. 63, 2223-2253.
- [96] Kim, I.D., Rothschild, A., Lee, B.H., Kim, D.Y., Jo, S.M., Tuller, H.L., 2006. *Nano Lett.* 6, pp. 2009–2013.
- [97] Li, M.Y., Guo, Y., Wei, Y., MacDiarmid, A.G., Lelkes, P.I., 2006. *Biomaterials*, 27, 2705–2715.
- [98] Zeng, J., Xu, X.Y., Chen, X.S., Liang, Q.Z., Bian, X.C., Yang, L.X., Jing, X.B., 2003. *Journal of Controlled Release*. 92, 227-231.
- [99] Venugopal, J.R., Low, S., Choon, A.T., Kumar, A. B., Ramakrishna, S., 2008. *Artificial Organs*. 32, 388 – 397.
- [100] Nama, J.H., Joo, Y.H., Lee, J.H., Chang, J.H., Cho, J.H., Chun, M.P., Kim, B.I., 2009. *Journal of Magnetism and Magnetic Materials*. 321, 1389–1392.
- [101] Hou, S., Li, X.X., Li, X.Y., Feng, X.Z., 2009. *Biofabrication*. 1, 1-7.
- [102] Wang, Z.G., Wan, L.S., Liu, Z.M., Huang, X.J., Xu, Z.K., 2009. *Journal of Molecular Catalysis B: Enzymatic*. 56, 189–195.
- [103] Ren, G.L., Xu, X.H., Liu, Q., Cheng, J., Yuan, X.Y., Wu, L.L., and Wan, Y.Z., 2006. *Reactive & Functional Polymers*. 66, 1559–1564.
- [104] Sawicka. K., Gouma, P., Simon, S., 2005. *Sensors and Actuators B*. 108, 585–588.
- [105] Quadrat, O., Stejskal, J., Kraochvil, P., Klason, C., McQueen, D., Kubat, J., Saha, P., 1998. *Syn. Metal*. 97, 37–42.
- [106] Tahir, Z.M., Alocilja, E.C., 2003. *Biosensors and Bioelectronics*. 18, 813-819.
- [107] Kim, J.H., Cho, J.H., Cha, G.S., 2000. *Biosensors and Bioelectronics*. 14, 907–915.
- [108] Brock, K. V., Chase, C. C. L., 2000. *Veterinary Microbiology*. 77, 209-214.
- [109] Nartker S., L. T. Drzal, and M. Misra (2005). “Aligned Electrospun Nanofibers for Nanocomposite Applications,” *Proceedings of the American Society for Composites*, pp. 77-89.
- [110] O. Quadrat, J. Stejskal, P. Kraochvil, C. Klason, D. McQueen, J. Kubat, and P. Saha (1998). “Electrical properties of polyaniline suspensions,” *Syn. Metal*, vol. 97, pp. 37–42.

- [111] S. Ramakrishna, K. Fujihara, W.E. Teo, T.C. Lim and Z.W. Ma, (2005) "An Introduction to Electrospinning and Nanofibers", World Scientific, pp 142-145.
- [112] Z. M. Tahir, E. C. Alocilja (2003). "A conductometric biosensor for biosecurity," *Biosensors and Bioelectronics*, vol. 18, pp. 813-819.
- [113] ICTVdB - The Universal Virus Database, version 4. Retrieved 11 December 2010, from <http://www.ncbi.nlm.nih.gov/ICTVdb/ICTVdB/>.
- [114] Ridpath, J. F. (2010). Bvdv: Detection, Risk Management and Control. Proceedings of Texas Veterinary Medical Association, p. 151-158.
- [115] Cloutier BC, Cloutier AK, Alocilja EC. Optimization of electrically active magnetic nanoparticles as accurate and efficient microbial extraction tools. *Biosensors (Basel)*. 2015;5(1):69-84. Published 2015 Feb 5. doi:10.3390/bios5010069.
- [116] J. H. Kim, J. H. Cho, and G. S. Cha (2000). "Conductimetric membrane strip immunosensor with polyaniline-bound gold colloids as signal generator," *Biosensors & Bioelectronics*, vol. 14, pp. 907-915.
- [117] K. V. Brock, and C. C. L. Chase (2000). "Development of a fetal challenge method for the evaluation of bovine viral diarrhoea virus vaccines," *Veterinary Microbiology*, vol. 77, iss. 1-2, pp. 209-2140.
- [118] J.C. Chiang, A.G. MacDiarmid (1986). "Polyaniline: protonic acid doping of the emeraldine form to metallic regime," *Synthetic Metal*, vol. 13, pp. 193-205.
- [119] M.P. Doyle, Food Safety: Bacterial Contamination, Editor(s): Benjamin Caballero, *Encyclopedia of Human Nutrition* (Third Edition), Academic Press, 2013, Pages 322-330, ISBN 9780123848857, <https://doi.org/10.1016/B978-0-12-375083-9.00124-0>.
- [120] Shi L, Xu L, Xiao R, Zhou Z, Wang C, Wang S and Gu B (2020) Rapid, Quantitative, High-Sensitive Detection of *Escherichia coli* O157:H7 by Gold-Shell Silica-Core Nanospheres-Based Surface-Enhanced Raman Scattering Lateral Flow Immunoassay. *Front. Microbiol.* 11:596005. doi: 10.3389/fmicb.2020.596005.
- [121] Chunxia Lu, Xiaoxu Gao, Ya Chen, Jiangtao Ren & Changbin Liu (2020) Aptamer-Based Lateral Flow Test Strip for the Simultaneous Detection of *Salmonella typhimurium*, *Escherichia coli* O157:H7 and *Staphylococcus aureus*, *Analytical Letters*, 53:4, 646-659, DOI: 10.1080/00032719.2019.1663528.
- [122] Zonghan Wang, Xiaolin Yao, Yongzhi Zhang, Rong Wang, Yanwei Jia, Jing Sun, Daohong Zhang, Jianlong Wang, (2020) Functional nanozyme mediated multi-readout and label-free lateral flow immunoassay for rapid detection of *Escherichia coli* O157:H7, *Food Chemistry*, Vol. 329, 1 November 2020, 127224.

- [123] A. Hatch, B. Weigl, D. Zebert, and P. Yager (1999). "Microfluidic approaches toward immunoassays," in Proc. SPIE Microfluidic Devices Syst. II, Santa Clara, CA.
- [124] G. Cavelier (1995). "Possible role of surface electrochemical electron-transfer and semiconductor charge transport processes in ion channel function," *Bioelectron. Bioeng.*, vol. 40, pp. 197–213.
- [125] Günther H., 1995, *NMR Spectroscopy: Basic Principles, Concepts, and Applications in Chemistry*, 2nd ed., Wiley, 15-48.
- [126] G.W. Ewing, 1997, *Analytical Instrumentation Handbook*, 2nd ed., CRC, 811-812.
- [127] Doscotch M.A., Evans J.F., Munson E.J., 1998, *Journal of Chemical Education*, 75, 8, 1008-1013.
- [128] Takeda K., 2007, *Rev. Sci. Instrum.*, 78, 033103.
- [129] Epel B., Sundramoorthy S.V., Mailer c., Halpern H.J., 2008, *Concepts Magn Reson Part B Magn Reson Eng*, 33B, 3, 163–176.
- [130] Takeda K., 2008, *Journal of Magnetic Resonance*, 192, 218–229.
- [131] Hassibi A., Babakhani A., Hajimiri A., 2009, *IEEE Journal of Solid-State Circuits*, 44, 6, 1805-1813.
- [132] Yong Liu, Nan Sun, Hakho Lee, Ralph Weissleder, and Donhee Ham, " CMOS mini nuclear magnetic resonance system and its application for biomolecular sensing," *Proceedings of IEEE International Solid-State Circuits Conference*, pp. 140-141 (Feb 2008)
- [133] Sun N., Yoon T.J., Lee H., Andress W.F., Weissleder R., Ham D., 2011, *IEEE Journal of Solid-State Circuits (JSSC)*, 46, 1, 342-352.
- [134] Sun N., Liu Y., Lee H., Weissleder R., Ham D., 2009, *IEEE Journal of Solid-State Circuits (JSSC)*, 44, 5, 1629-1643.
- [135] ZYSW-2-50DR+, Reflective SPDT, Solid State Switch, <https://www.minicircuits.com/WebStore/dashboard.html?model=ZYSW-2-50DR%2B>, June 2020
- [136] Basys 2 Spartan-3E FPGA Trainer Board, <https://store.digilentinc.com/basys-2-spartan-3e-fpga-trainer-board-limited-time/>, June 2020
- [137] 50B High Frequency (HF) solid state power amplifier, Henry Radio Inc., <https://www.henryradio.com/amplifiers.html>, June 2020

- [138] AU-1467 low noise amplifier, "Bipolar amplifiers," Narda Miteq Inc., retrieved in June 2020, <https://nardamiteq.com/docs/C22E.PDF>.
- [139] Sonoma-instrument 310 low noise amplifier, "Sonoma Instrument 310 Broadband Amplifier," retrieved in September 2020, <http://sonoma-instrument.com/pdf/sonoma-instrument-310.pdf>
- [140] Lee H., Sun E., Ham D., Weissleder R., 2008, *Nature Medicine*, 14, 8, 869-874.
- [141] CDC, 2009, E. coli Outbreak Investigations, <http://www.cdc.gov/ecoli/2009/1124.html>.
- [142] Dundas S., Todd W.T., Stewart A.I., Murdoch P.S., Chaudhuri A.K., Hutchinson S.J., 2001, *Clin Infect Dis*, 33, 7, 923-931.
- [143] CDC, 2011, E. coli Outbreak Investigations, <http://www.cdc.gov/ecoli/outbreaks.html>.
- [144] Frenzen P.D., Drake A., Angulo F.J., 2005, *J Food Prot*, 68, 12, 2623-2630.
- [145] Wells J.G., Davis B.R., Wachsmuth I.K., 1981, *Journal of clinical microbiology*, 18, 3, 512-520.
- [146] March S. B., Ratnam S., 1986, *J Clin Microbiol*, 23, 5, 869-872.
- [147] Guan J., Levin R.E., 2002, *Food Biotechnology*, 16, 3, 155 – 166.
- [148] Fratamico P.M., Strobaugh T.P., Medina M.B., Gehring A.G., 1998, *Biotechnology Techniques*, 12, 7, 571-576.
- [149] Lin Y.H., Chen S.H., Chuang Y.C., Lu Y.C., Shen T.Y., Chang C.A., Lin C.S., 2008, *Biosensors and Bioelectronics*, 23, 1832-1837.
- [150] Permanent magnets PM1055, Metrolab Inc., Geneva, Switzerland (2011) <http://www.metrolab.com/index.php?id=28>.
- [151] Fukushima E., 1993, *Experimental Pulse NMR: A Nuts and Bolts Approach*.
- [152] Behzad Razavi, 2011, *RF Microelectronics (2nd Edition)*, Prentice Hall Press, pp.74
- [153] Selectivity and Q of a Circuit, <http://hyperphysics.phy-astr.gsu.edu/hbase/electric/serres.html>, 2020
- [154] Louis N. Hand and Janet D. Finch, "Analytical Mechanics," Cambridge, England: Cambridge University Press, pp. 192. ISBN 978-0-521-57572-0, 1998.

- [155] Fundamental Physical Constants, "Proton gyromagnetic ratio in MHz/T", NIST, https://physics.nist.gov/cgi-bin/cuu/Value?gamma_pbar, 2020.
- [156] D. I Hoult and R. E Richards. The signal-to-noise ratio of the nuclear magnetic resonance experiment. *Journal of Magnetic Resonance* (1969), 24(1):71–85, October 1976. 1.3.1, 1.3.1.1
- [157] R.C. Hansen, "Fundamental limitations in antennas," *Proc. of IEEE*, 69(2), pp. 170-182, 1981.
- [158] A.D. Yaghjian, and S.R. Best, "Impedance, bandwidth, and q of antennas," *IEEE Trans. Antennas Propagat.*, 53(4), pp. 1298-1324, 2005
- [159] Leong, Kenneth, J. Mazierska, Mohan V. Jacob, and D. Ledenyov. "Comparing unloaded Q-factor of a high-Q dielectric resonator measured using the transmission mode and reflection mode methods involving S-parameter circle fitting." In *2002 IEEE MTT-S International Microwave Symposium Digest (Cat. No. 02CH37278)*, vol. 3, pp. 1665-1668. IEEE, 2002.
- [160] Luo and Alocilja, Portable nuclear magnetic resonance biosensor and assay for a highly sensitive and rapid detection of foodborne bacteria in complex matrices, *Journal of Biological Engineering* (2017) 11:14
- [161] EC Alocilja, Y Luo, Nuclear magnetic resonance apparatus, systems, and methods, US Patent 10,359,378, 2019
- [162] Harald Günther, *NMR Spectroscopy: Basic Principles, Concepts, and Applications in Chemistry*, Wiley 2nd Edition, 14 Oct 2016
- [163] Ng SM. Chapter 3 - Portable NMR-Based Sensors in Medical Diagnosis A2 - ur-Rahman, Atta. In *Applications of NMR Spectroscopy*, M. I. Choudhary, Ed. Bentham Science Publishers, 2015, pp. 121–146.
- [164] Yu D, Garcia N, Xu S. Toward portable nuclear magnetic resonance devices using atomic magnetometers. *Concepts Magn Reson Part A*. 2009;34A(2): 124–32.
- [165] Conventional nuclear magnetic resonance (NMR) system, https://en.wikipedia.org/wiki/Nuclear_magnetic_resonance, Accessed Sept 2019
- [166] Stefan H Bossmann, Hongwang Wang, *Magnetic Nanomaterials: Applications in Catalysis and Life Sciences*, Royal Society of Chemistry, Cambridge 2017
- [167] Pal S., Settingington E, Alocilja EC. Electrically active magnetic nanoparticles for concentrating and detecting *Bacillus anthracis* spores in a direct-charge transfer biosensor. *IEEE Sensors J*. 2008;8(6):647–54.

- [168] Nuclei spin energies split in an external magnetic field, https://en.wikipedia.org/wiki/Nuclear_magnetic_resonance/media/File:NMR_splitting.gif, , Accessed Oct 2019
- [169] Dybowski, C. Zeeman Interaction in Nuclear Magnetic Resonance. In *Encyclopedia of Analytical Chemistry* (eds R.A. Meyers and C. Dybowski). doi:10.1002/9780470027318.a6119, 15 September 2006
- [170] Gueron M (1975). *Nuclear relaxation in macromolecules by paramagnetic ions: A novel mechanism*. *J Magn Reson* 19, 58–66.
- [171] L. Banci, I. Bertini, and C. Luchinat (1991). *Nuclear and Electron Relaxation*, VCH, Weinheim.
- [172] Roch, Muller, and Gillis, Theory of proton relaxation induced by superparamagnetic particles, *J. Chem. Phys.*, Vol. 110, No. 11, pp. 5403-5411, 15 March 1999
- [173] Freed JH (1978). *Dynamic effects of pair correlation functions on spin relaxation by translational diffusion in liquids*. *J Chem Phys* 68, 4034–4037.
- [174] Y. Ayant, E. Belorizky, J. Aluzon, Jean Gallice. Calcul des densites spectrales resultant d'un mouvement aleatoire de translation en relaxation par interaction dipole-dipole magnetique dans les liquides. *Journal de Physique*, 1975, 36 (10), pp.991-1004.
- [175] Kittel, Charles. *Introduction to Solid State Physics*, 8th Edition. Wiley. pp. 304, 2004
- [176] Apostolos Kantzas, Jonathan Bryan, Saeed Taheri, "Fundamentals of Fluid Flow in Porous Media," retrieved in October 2020, <https://perminc.com/resources/fundamentals-of-fluid-flow-in-porous-media/chapter-3-molecular-diffusion/diffusion-coefficient/measurement-techniques/nmr-method/principles-nmr-processing/spin-echo-cpmg-pulse-sequence/>
- [177] Luo, Y., Nartker, S., Miller, H., Hochhalter, D., Wiederoder, M., Wiederoder, S., Setterington, E., Drzal, L.T., Alocilja, E.C., 2010, *Biosensors and Bioelectronics*, 26, 4, 1612-1617
- [178] Roch, A., Muller, R.N., and Gillis, P. (1999) Theory of Proton Relaxation Induced by Superparamagnetic Particles, *J. Chem. Phys.* 110, 5403–5411.
- [179] Sharma S, Byrne H, O’Kennedy RJ. Antibodies and Antibody-Derived Analytical Biosensors. Ed. Pedro Estrela. *Essays Biochem.* 2016;60(1):9–18.
- [180] Kothary MH, Babu US. Infective Dose of Foodborne Pathogens in Volunteers: A Review. *J Food Saf.* 2001;21(1):49–68.
- [181] Loynachan AT, Harris DL. Dose Determination for Acute Salmonella Infection in Pigs. *Appl Environ Microbiol.* 2005;71(5):2753–5.

[182]E.C. Alocilja, Y. Luo, Nuclear magnetic resonance apparatus, systems, and methods, US Patent 10,359,378, 2019